SYNTHESIS OF Al-Ga CO-DOPED TIN OXIDE NANOPARTICLES USING *Psidium guajava* LEAVES EXTRACT AND CHARACTERIZATION FOR POTENTIAL APPLICATION IN SOLAR CELL

Bethwel Kiprotich

A Thesis Submitted in Partial Fulfillment of the Requirements for the Degree of Master of Science in Chemistry of Murang'a University of Technology

August, 2025

DECLARATION

Student Declaration

I hereby declare that this Thesis is my original work and to the best of my knowledge has not been presented for a degree award in this or any other university. I understand what plagiarism is and I am aware of the University's policy in this regard. I understand that any false claim in respect of this work shall result in disciplinary action in accordance with the University Anti-Plagiarism Policy.

_____ _____

Bethwel Kiprotich Date

Reg no: AS401/5137/2023

Supervisors' Approval

The undersigned certify that they have read and hereby recommended for acceptance of Murang'a University of Technology a thesis entitled **"Synthesis of Al-Ga Co-doped Tin Oxide Nanoparticles using *Psidium Guajava* Leaves Extract and Characterization for Potential Application in Solar Cells".**

_____ _____

Dr. Peter Waithaka Njoroge, Date

Department of Physical and Biological Science,

Murang'a University of Technology.

_____ _____

Prof. Sylvia Awino Opiyo, Date

Department of Physical and Biological Sciences,

Murang'a University of Technology.

DEDICATION

This thesis is dedicated to my mother, Hellen Kiplagat, whose unwavering support and encouragement have been a constant source of inspiration throughout my academic journey. Her belief in my abilities and her sacrifices have made this achievement possible.

ACKNOWLEDGEMENT

I am forever grateful to the Almighty God for his protection, guidance, providence, and care throughout my studies. I appreciate the valuable mentorship of my supervisors Dr. Peter W. Njoroge and Prof Sylvia A. Opiyo for their tireless efforts and guidance throughout the study.

This research has been successful due to the financial support received from BMBF, the German Ministry of Education and Research and UNESCO – TWAS courtesy of Dr. Sharon Kiprotich. I'm deeply humbled and obliged for choosing me to benefit from your research grant.

Thanks to the School of Pure and Applied Sciences, Murang'a University of Technology, for the tremendous support during my undergraduate and masters' studies. I acknowledge with a lot of gratitude the grant of access to various synthesis equipment, apparatus, characterization techniques, and technical assistance while working in the laboratory aided by the technologist, James Waweru, Charles Gitau, Kariuki, Ann and Maggy of Murang'a University of Technology, and Mr. Ngugi of Kenyatta University. To my colleague Joan, James, Shadrack, Nancy, Nimrod and Collins, I am thankful for your support during my study period.

To my parents Hellen Kiplagat, Leonida Kiplagat, Dinah Kiplagat and my siblings Anderson Kipchirchir and Caren Jebiwot, thank you for your support prayer and encouragement. I also thank Mr. Francis Kipruto for the advice and finance support, feel appreciated and honoured.

Finally, I would like to thank myself for not giving up, being discipline and giving my best on this academic journey.

ABSTRACT

A significant percentage of greenhouse gases (GHGs) are emitted during burning of fossil fuel, contributing to climate change by trapping heat leading to an increase in global temperature. Alternative energy sources have been explored as they are considered clean and non-polluting. While solar cells typically have low efficiency in converting sunlight into electricity, doping of metal oxide semiconductors used in solar cells can help resolve this issue. Due to their interesting energy band gaps, which can be readily adjusted by doping with foreign elements, metal oxide semiconductors like tin oxide have a wide range of applications. The research focuses on the synthesis and characterization of undoped tin oxide nanoparticles (NPs) with and without *Psidium guajava* extract, to determine the effects of Al and Ga doping concentrations (0.5, 1.0, 1.5, 2.0 and 2.5%) and to investigate the effects of varying Al and Ga co-doping ratios (25:75, 50:50 and 75:25 %) on the structural, luminescence and optical properties of tin oxide nanoparticles. Synthesis was done using green synthesis method by utilizing *Psidium guajava* as caping agent and the nanoparticles were characterized using Photoluminescence spectrophotometer (PL), ultra-violent visible spectrophotometer (UV-Vis), X-ray diffractometer (XRD) and Fourier transform infrared spectrophotometer (FTIR). From the UVVis results, the band gap of capped and uncapped tin oxide was 3.98 and 3.21 eV, respectively. The band gap decreased upon doping and co-doping. For capped Al, Ga and Al: Ga-SnO_2, obtained band gap were within 2.01-2.88, 2.29-3.25 and 1.58-1.69 eV, respectively. For uncapped Al, Ga and Al: Ga-SnO_2, optical band gaps were within 2.38-2.89, 2.46-3.07 and 3.063.14 eV, respectively. Using the Scherrer equation, crystallite sizes of 14.89 and 18.00 nm were calculated for capped and uncapped SnO_2. For Al-doped SnO_2, the smallest crystallite sizes were observed at 2.0% doping (capped, 10.57 nm) and 1.5% doping (uncapped, 12.47 nm). For Ga-doped SnO_2, the smallest sizes were at 2.5% (capped) and 1.5% (uncapped). PL spectra showed a strong emission peak and a broadband in the 460-480 nm range, attributed to the defect and oxygen vacancy recombination. For capped Al-SnO_2, Ga-SnO_2 and Al:Ga-SnO_2, the highest PL intensities were observed at 2% Al, 0.5% Ga and 75:25 Al:Ga-SnO_2 ration, peak intensities were highest at 2.0 % Al, 2.0% Ga, and a 75:25 ratio. The lowest PL intensity peaks were observed at 2.5 % Al, 1.0 % Ga and 25:75 Al:Ga-SnO_2 ratio in both capped and uncapped samples. Doping and co-doping significantly tuned SnO_2 nanoparticle properties, improving their optical and structural characteristics for potential solar applications. Future studies should explore other green synthesis routes and dopant elements to further enhance SnO_2 efficiency in optoelectronic devices.

TABLE OF CONTENTS

DECLARATION ..... **ii**
DEDICATION ..... **iii**
ACKNOWLEDGEMENT ..... **iv**
ABSTRACT ..... **v**
LIST OF TABLES ..... **ix**
LIST OF FIGURES ..... **x**
ACRONYMS AND ABBREVIATIONS ..... **xiii**
DEFINITION OF OPERATIONAL TERMS ..... **xiv**
CHAPTER ONE: INTRODUCTION **1**
1.1 Background Information 1
1.2 Statement of Problem 2
1.3 Significance of the Study 3
1.4 Objectives of the Study 4
1.4.1 General objectives of the Study 4
1.4.2 Specific Objectives 4
1.5 Research Questions 4
1.6 Scope and Limitation 4
1.7 Contribution of the Thesis 5
1.8 Organization of the Thesis 5
CHAPTER TWO: LITERATURE REVIEW **6**
2.1 General Introduction 6
2.2 Solar Cells 6
2.3 Metal Oxide Nanoparticles and their Applications 8
2.4 Tin Oxide 9
2.5 Dopants 10
2.5.1 Gallium Doped Tin Oxide 10
2.5.2 Aluminium Doped Tin Oxide 11
2.6 Crystalline Structure of Tin Oxide 11
2.7 Synthesis of nanoparticles 12
2.7.1 Sol gel Method 13
2.7.2 Chemical Precipitation 14
2.7.3 Green Synthesis Method 15
2.8 Analytical Techniques used to Characterization nanoparticles 16
2.8.1 Fourier Transform infrared spectroscopy (FT-IR) 17
2.8.2 Ultraviolent Visible spectroscopy (UV-Vis) 18

2.8.3 X-ray diffraction (XRD) 19
2.8.4 Photoluminescence spectroscopy (PL) 19
2.9 Chapter Summary 19
CHAPTER THREE: MATERIALS AND METHODS 21
3.1 Introduction 21
3.2 Materials 21
3.3 Methods 21
3.3.1 Preparation of *Psidium guajava* leaf extract 21
3.3.2 Synthesis of pure tin oxide NPs without *P. guajava* extract 22
3.3.3 Synthesis of tin oxide nanoparticles using *P. guajava* leaf extract 22
3.3.4 Synthesis of gallium doped tin oxide NPs without *P. guajava* extract 23
3.3.5 Synthesis of gallium doped tin oxide NPs using *P. guajava* extract 24
3.3.6 Synthesis of aluminium doped tin oxide without *P. guajava* extract. 24
3.3.7 Synthesis of aluminium doped tin oxide nanoparticles with *P. guajava* extract. 24
3.3.8 Synthesis of Al-Ga co-doped tin oxide NPs without *P. guajava* leaf extract. 25
3.3.9 Synthesis of Al-Ga co-doped tin oxide NPs using *P. guajava* leaf extract 25
3.4 Characterization of the synthesized nanoparticles 25
3.4.1 The UV-Vis characterization 25
3.4.2 XRD Characterization 26
3.3.3 Photoluminescence characterization 28
3.4.4 FT-IR characterization 29
3.5 Chapter Summary 30
CHAPTER FOUR: RESULTS AND DISCUSSION 31
4.1 Introduction 31
4.2 Characterization undoped tin oxide nanoparticles with and without *p. guajava* leaf extract as capping agent 31
4.2.1 Optical analysis of undoped tin oxide nanoparticles 31
4.2.2 XRD analysis of undoped tin oxide nanoparticles 34
4.2.3 Photoluminescence spectroscopy analysis of undoped nanoparticles 37
4.2.4 The FTIR analysis of undoped nanoparticles 39
4.3 Optimization of Al and Ga doping concentration on the synthesis of SnO_2 NPs 40

4.3.1: Effect of varying Al doping concentration on the structural, luminescence and optical properties of SnO_2 NPs synthesized with and without the caping agent 40
4.3.1.1 Optical analysis of doped and undoped nanoparticles 40
4.3.1.2 XRD analysis doped nanoparticles 43
4.3.1.3 Photoluminescence (PL) analysis of doped nanoparticles 49
4.3.1.4 FTIR analysis of doped nanoparticles 53
4.3.2 Effect of Ga doping concentration on the structural, luminescence and optical properties of SnO_2 NPs synthesized with and without *P. guajava* extract 54
4.3.2.1 UV-Vis analysis of doped nanoparticles 54
4.3.2.2: XRD analysis of doped nanoparticles 57
4.3.2.3 Photoluminescence analysis of doped nanoparticles 63
4.3.2.4 FTIR analysis of doped nanoparticles 67
4.4 Effects of varying Al and Ga co-doping ratios on the structural, luminescence and optical properties of tin oxide nanoparticles 68
4.4.1 Optical analysis of co-doped nanoparticles 68
4.4.2 XRD analysis of co-doped nanoparticles 71
4.4.3 Photoluminescence analysis of co-doped nanoparticles 75
4.4.4 FTIR analysis Al and Ga co-doped nanoparticles 77
4.5 Chapter Summary 77
CHAPTER FIVE: CONCLUSION AND RECOMMENDATIONS 79
5.1 Conclusion 79
5.2 Recommendations 82
5.2.1 Recommendations for Policy 82
5.2.2 Recommendations for future work 82
REFERENCES 83
APPENDICES 103

LIST OF TABLES

Table 4.1: FWHM, crystallite size (d), d-spacing, dislocation density(δ) and micro-strain of undoped SnO_2 nanoparticles 36
Table 4.2: Energy band gaps (eV) of pure SnO_2 and Al-SnO_2 synthesized with and without *P. guajava* extract 43
Table 4.3: 2θ, full width at half maximum (FWHM), Crystallite size (D) and dislocation density (δ) for capped Al-SnO_2 47
Table 4.4: 2θ, full width at half maximum (FWHM), Crystallite size (D) and dislocation density (δ) for uncapped Al-SnO_2 48
Table 4.5: Lattice parameters (a and c), and strain (∈) for capped and uncapped Al-SnO_2 49
Table 4.6: Photoluminescence Intensity and peak centre of Al-SnO_2 53
Table 4.7: Energy band gap (eV) of pure SnO_2 and Ga-SnO_2 synthesized with and without *P. guajava* extract 56
Table 4.8: 2θ, full width at half maximum (FWHM), crystallite size (D) and the dislocation density (δ) for uncapped (a) and capped (b) Ga-SnO_2 60
Table 4.9: Lattice parameter (a and c) and micro-strain of capped and uncapped Ga-SnO_2 62
Table 4.10: Peak centre and intensity of Ga-SnO_2 at varying mol concentration of gallium 67
Table 4.11: Energy band gap (eV) of pure SnO_2 and Al:Ga-SnO_2 synthesized with and without *P. guajava* extract 71
Table 4.12: 2θ, full width at half maximum (FWHM), average FWHM, crystallite size (D) and average D of Al:Ga-SnO_2 72
Table 4.13: Dislocation density and micro strain of Al:Ga-SnO_2 75
Table 4.14: Peak centre and intensity of Al:Ga-SnO_2 76

LIST OF FIGURES

Figure 2.1: Silicon based photovoltaic solar cell 6
Figure 2.2: Basic structure of photovoltaic solar cell 7
Figure 2.3: Differences between insulators, semiconductors and conductors 8
Figure 2.4: Top-down and Bottom-up approach for synthesizing nanoparticles..... 12
Figure 2.5: Physical, chemical and biological synthesis of nanoparticle 13
Figure 2.6: Different stages of sol-gel process 14
Figure 2.7: Schematic diagram of plant extract-mediated synthesis of SnO_2 NPs 15
Figure 2.8: P. guajava (Guava) plant in its habitat..... 16
Figure 3.1: Schematic representation of *P. guajava* leaves extract preparation 22
Figure 3.2: SnO_2 NPs preparation using *P. guajava* leaf extract..... 23
Figure 3.3: UV-VIS spectrophotometer at Murang'a University of Technology..... 26
Figure 3.4: XRD diffractometer EQUINOX 100 at Murang'a University of Technology 28
Figure 3.5: Photoluminescence spectrophotometer (PL) at Murang'a University of Technology 29
Figure 3.6: FT-IR spectrophotometer at Murang'a University of Technology..... 30
Figure 4.1: Absorbance spectrum of synthesized SnO_2 with and without p. guajava extract 32
Figure 4.2: Tauc's plot extrapolation of capped and uncapped SnO_2..... 34
Figure 4.3: XRD pattern of SnO_2 synthesized with and without *P. guajava* extract 35
Figure 4.4: PL spectra of SnO_2 NPs with and without p. guajava extract 38
Figure 4.5: FTIR spectra of capped and uncapped SnO_2 in the range 400-4000 cm^{-1} 40
Figure 4.6: Absorbance spectra of synthesized SnO_2 and Al doped SnO_2 with (a) and without (b) *P. guajava* extract 41
Figure 4.7: Tauc's plot estimate of SnO_2 and Al-SnO_2 synthesized with (a) and without (b) *P. guajava* extract 42
Figure 4.8: XRD pattern of synthesized SnO_2 and Al-SnO_2 with (a) and without (b) *P. guajava* extract 44
Figure 4.9: Relationship between crystallite size with FWHM of capped (a) and uncapped (b) Al-SnO_2 45

Figure 4.10: Trend of dislocation density and strain of capped (a) and uncapped (b) Al-SnO_2 46
Figure 4.11: Variation in crystallite size and strain for capped (a) uncapped (b) Al-SnO_2 49
Figure 4.12: Photoluminescence spectra of pure SnO_2 and Al- SnO_2 synthesized with *P. guajava* extract in the range 250-500 nm 50
Figure 4.13: Photoluminescence spectra of pure SnO_2 and Al- SnO_2 synthesized without *P. guajava* extract in the range 250-500 nm 51
Figure 4.14: FTIR spectra of capped (a) and uncapped (b) Al-SnO_2 54
Figure 4.15: Absorption spectra of synthesized pure SnO_2 and Ga-SnO_2 with (a) and without (b) *P. guajava* extract 55
Figure 4.16: Tauc's plot estimate of synthesized SnO_2 and Ga-SnO_2 with (a) and without (b) *P. guajava* extract 57
Figure 4.17: XRD pattern of synthesized SnO_2 and Ga-SnO_2 with (a) and without (b) *P. guajava* extract in the range 20°-80° 58
Figure 4.18: Trend of micro strain and dislocation density of capped (a) and uncapped (b) Ga-SnO_2 59
Figure 4.19: Relationship between crystallite size and FWHM of capped (a) and uncapped (b) Ga-SnO_2 61
Figure 4.20: Shows the variation in crystallite size and strain for capped (a) and uncapped (b) Ga-SnO_2 63
Figure 4.21: Photoluminescence spectra of synthesized pure and Ga-SnO_2 with *P. guajava* extract 64
Figure 4.22: Photoluminescence spectra of synthesized pure and Ga-SnO_2 without *P. guajava* extract 65
Figure 4.23: FTIR spectra of capped (a) and uncapped (b) Ga-SnO_2 at varying concentrations of the dopant 68
Figure 4.24: UV-Vis spectra of synthesized pure SnO_2 and Al-Ga-SnO_2 co-doped SnO_2 with (a) and without (b) *P. guajava* extract 69
Figure 4.25: Tauc's plot extrapolation of synthesized pure SnO_2 and Al-Ga-SnO_2 co-dopped SnO_2 with (a) and without (b) *P. guajava* extract 70
Figure 4.26: XRD pattern of synthesized SnO_2 and AlGa-SnO_2 with (a) and without (b) *P. guajava* extract in the range 20°-80° 71
Figure 4.27: Variation of FWHM with crystallite size with (a) and without (b) *P. guajava* extract 73

Figure 4.28: Variation between crystal size and strain of capped (a) and uncapped (b) Al:Ga-SnO_2 74
Figure 4.29: Dislocation density and strain of capped (a) and uncapped (b) Al:Ga-SnO_2 74
Figure 4.30: Pl spectra of capped (a) and uncapped (b) Al:Ga-SnO_2 76
Figure 4.31: FTIR spectra of capped (a) and uncapped (b) Al:Ga SnO_2 77

ACRONYMS AND ABBREVIATIONS

BGN	Band gap narrowing
BGW	Band gap width
DLE	Deep level emission
DSSC	Dye sensitive solar cell
FWHM	Full width at half maximum
GHGs	Green-house gases
JCPDS	Join committee of power diffraction standards
MRI	Magnetic resonance imaging
MSD	Magnetic storage device
NBE	Near band emission
NPS	Nanoparticles
PL	Photoluminescence spectroscopy
TCO	Transparent conducting oxide
UV-Vis	Ultra-violent visible spectroscopy
VOC	Open circuit voltage
XRD	X-ray diffractometer

DEFINITION OF OPERATIONAL TERMS

Capped: Nanoparticles synthesized with the caping agent.

Co-doping: the simultaneous introduction of two or more different dopant impurities into a material, typically a semiconductor, to modify its properties.

Dislocation density: is a measure of the number of dislocations within a specific volume of a crystalline material

Doping: Introducing foreign atom into the host crystal lattice to improve its optical and structural properties by modifying the crystal structure, conductivity, band position, and surface state.

Energy bandgap: the minimum energy required for an electron to jump from a lower energy level to a higher energy level in a solid material

Lattice parameters: a physical quantity that defines the dimensions of the repeating unit cell in a crystal lattice

Optical properties: They describe how the material interact with light across the electromagnetic spectrum, including visible and Ultra violet, offering insights that help when applied in lasers, light emitting diodes, photovoltaic, optical sensors and optical communication devices

Strain: the deformation of a material's crystal lattice, where the atomic spacing is either compressed or expanded

Synthesis: The process of producing a compound, material or a substance by combining individual components in a systematic manner.

Uncapped: Nanoparticles synthesized without the capping agent.

CHAPTER ONE
INTRODUCTION

1.1 Background Information

The major source of energy consumed worldwide are fossil fuels, as it generates electrical and thermal energy essential for various domestic and industrial applications. Fossil fuel emits greenhouse gas (GHGs) specifically carbon dioxide during the generation of power (Ye *et al.*, 2015). Solar cells have received considerable attention as they rely on sun for generation of energy. However, despite the use of solar energy, they are expensive and less efficient compared to fossil fuel. Perovskite Cadmium Telluride (CdTe) Solar Cells, Monocrystalline Silicon (c-Si) Solar Cells are examples of solar cell technologies that harness sunlight to generate electricity. To enhance light trapping in silicon solar cells, nanoparticles may be required. The sun provides a free, natural, and inexhaustible source of energy. Harnessing direct sunlight and converting into electrical energy has created a source of electrical energy that can be relied upon (Kalyani *et al*., 2015).

Metal oxides with nanostructure include tin oxide (SnO_2), titanium oxide (TiO_2) and zinc oxide (ZnO). Among these, SnO_2 is one of binary semiconductors that have been considered for solar cell application due to its wide direct band gap, optical transparency and high electron mobility (Ko *et al*., 2011). The oxygen vacancy present in pure tin oxide makes an n-type semiconductor, with a room temperature direct band gap of 3.68 eV (Azam *et al*., 2010), which helps to protects dye-sensitive solar cells (DSSCs) from long term UV deterioration. SnO_2 can also possess high electrical conductivity when doped with foreign impurities (Banyamin *et al.*, 2014).

A nanoparticle is a tiny particle typically measuring between 1 to 100 nms. The properties of metal oxide nanoparticles such as optical, structural and electrical characteristics are dramatically improved by doping with a suitable dopant at correct concentration (Altaf *et al.*, 2023). When a lower valency cation is introduced in tin oxide lattice, carrier conversion occurs, decreasing *n*-type conductivity and increasing the hole concentration, thereby enhancing the *p*-conductivity (Benouis *et*

al., 2014). Notably, effective doping is achieved when the ionic radius of the dopant is equal to or smaller than that of the host ion Sn^{4+} (r=0.71 Å) *(*Benouis *et al.*, 2014). Doping SnO_2 with gallium raises its band edge (Teh *et al*., 2013). By increasing the band edge, Ga-doping elevates the energy levels at which electrons can be excited to the conduction band (CB) from the valence band (VB). The band edge increase has implications on the performance of SnO_2 in various applications, including solar cells.

Different methods have been used to synthesize SnO_2 nanoparticles including the sol-gel route (Subramaniam *et al.*, 2018), hydrothermal method (Patil *et al*., 2012), chemical vapor deposition (Nagirnyak *et al.*, 2016) and thermal evaporation of oxide powder (Patil *et al.*, 2012. However, these methods are often considered, as they utilize toxic reagents and involve tedious procedures to prepare nanoparticles. Therefore, there is need to develop economic friendly and green method to synthesize these nanoparticles. Physical and chemical methods are gradually being replaced by green synthesis technique (Alsammarraie *et al*., 2018) due to concerns related to high energy consumption (Horwat *et al.*, 2011), the release of toxic and hazardous chemicals (Hoag *et al*., 2009) and use of complex equipment and synthesis conditions (Ahmed *et al,* 2015).

Green synthesis offers significant advantages over the traditional chemical and physical methods, as it is non-toxic (Devi *et al*., 2019), pollution free (Alsammarraie *et al*., 2018), environment friendly, and cost effective (Kataria *et al*., 2018). The green method typically involves the use of plant extract as capping and stabilizing agents to control the crystal growth of nanoparticles. Phytochemical components in plant extracts such as flavonoids, terpenoids, phenolics, aldehyde, and ketones act as natural reducing and stabilizing agents. *Psidium guajava* contains high amounts of polyphenols which are inexpensive, renewable and widely available and potentially effective for promoting nanoparticle growth.

1.2 Statement of Problem

Fossil fuels represent almost 80% of the global known primary sources of energy. The generation of energy through burning of fossil fuel causes greenhouse gas

emission and responsible for an estimated 74% of all CO_2 emissions into the atmosphere. The emitted gases lead to global warming significantly influencing the ecosystems, cause rise in sea level and affecting agricultural production. Pollutants such as nitrogen oxide, sulfur dioxide and particulate matter are also released during fossil fuels combustion, contributing to air pollution and associated health problems. Reducing the consumption of fossils fuel would lower the amount of greenhouse gases (GHGs) released into the atmosphere. Thus, the need to reduce global temperatures and air pollution calls for development of alternative technology.

Renewable energy sources such as wind power, hydropower, solar energy, biomass, biofuel and geothermal energy are considered as prime step to reduce fossil fuel dependence, as they are regarded as clean and non-polluting. Solar energy, in particular, is a promising option since it can be harnessed as long as the sun continues to shine. Unlike fossil fuels, solar cells do not emit GHGs. To trap solar energy, solar cells are required. However, solar cells are not fully efficient in trapping solar energy.

Tin oxide (SnO_2) nanoparticles have recently garnered attention for use in solar cell applications due to their optical transparency, high electron mobility, large electron diffusion coefficient and wide band gap. However, SnO_2 suffers from the problem of low conduction band edge, which promotes the rapid backflow of photoelectrons to the electrolyte, thereby reducing the open circuit voltage. These material properties of SnO_2 nanoparticles search as the optical, structural, luminescence and electrical properties can be enhanced through doping with suitable elements. The current research focuses on improving the properties of SnO_2 nanoparticles such as the optical, structural, luminescence and electrical properties, through doping and co-doping with aluminium and gallium (Al-Ga-SnO_2) using *Psidium guajava* leaf extract.

1.3 Significance of the Study

Improving the efficiency of solar cell means less relying on fossil fuel. Nanotechnology has attracted considerable attention for its ability to transform material and for driving the advancement of sustainable energy sources. The synthesis method is referred to as green synthesis method since it uses less chemicals and toxic

chemicals are replaced with plant extract. This research aimed at synthesizing Al and Ga doped tin oxide NPs using *Psidium guajava* extract. The research findings provide knowledge on the importance of doping metal oxide for solar cell application and also form a basis on how nanoparticles can be synthesized without use of expensive chemicals. This research focused on improving properties of SnO_2 nanoparticles for solar cell. This was achieved through the use of green synthesis methods specifically by using *Psidium guajava* leaf extract as a capping agent and optimization of Al-Ga co-doped on tin oxide nanoparticles.

1.4 Objectives of the Study

1.4.1 General objectives of the Study

To synthesize Al-Ga co-doped tin oxide nanoparticles using *Psidium guajava* leaf extract and characterize for potential application in solar cell.

1.4.2 Specific Objectives

i. To synthesize and characterize undoped tin oxide nanoparticles with and without using *Psidium guajava* leaf extract as capping agent.
ii. To determine the effect of varying Al and Ga doping concentration on the structural, luminescence and optical properties of tin oxide nanoparticles
iii. To investigate the effects of varying Al and Ga co-doping ratios on the structural, luminescence and optical properties of tin oxide nanoparticles.

1.5 Research Questions

1. Does *Psidium guajava* leaf extract (as a capping agent) affects the structural, luminescence and optical property of undoped tin oxide nanoparticles?
2. Does varying concentration of Al and Ga dopants affect the structural, luminescence and optical property of tin oxide nanoparticles?
3. Does co-doping Al and Ga ratios have effects on structural, luminescence and optical property of tin oxide nanoparticle?

1.6 Scope and Limitation

Psidium guajava leaf extract was used only as capping agent. Only Al and Ga ions were employed as dopants. This research involved the synthesis and characterization

of Al and Ga doped tin oxide NPs and Al-Ga co-doped tin oxide nanoparticles capped with *Psidium guajava*. Although various plant parts such as roots, leaves, stem, fruits and flowers have been successfully used as capping agents, this study focused on leaf extract of *Psidium guajava.* While metal oxide semiconductors have been widely applied in solar cells, this research focused on tin oxide NPs. Only structural and optical properties were studied.

1.7 Contribution of the Thesis

This research addresses, climate change problems by reducing dependence on environmental unfriendly sources of non-renewable energy, the current global energy crisis and offers a sustainable solution to the growing demand for energy. The use of renewable energy sources such as solar energy is crucial for reducing the dependence on unfriendly energy sources to the environment and promoting a sustainable future. The study's contributions lie in the potential application of optimized Al, Ga and Al:Ga SnO_2 co-doped nanoparticles in solar cells, where their unique properties leads to improved efficiency and performance of the solar cell. This study contributes to the development of optimized nanoparticles that is used in the photo-anode of the Dye-Sensitized Solar Cells (DSSC) to provide green energy.

1.8 Organization of the Thesis

The thesis has been arranged into five chapters, with chapter one having the fundamental aspects of renewable energy, emphasizing the significance of solar energy and articulating the problem statement, objectives, research questions, and its scope and limitations. The second chapter reviews previous studies of the properties of SnO_2, Al, and Ga. The chapter also discuss the methods of synthesizing nanoparticles and characterization techniques. Chapter three outline the materials and reagents that were used in the synthesis process and procedure of obtaining the nanoparticles for the study. It outlines how each nanoparticle was obtained as per the objectives and the techniques that were used to characterized nanoparticles. Chapter 4 discuss the results obtained from characterization of nanoparticles using XRD, FTIR, PL, and UV-Vis. The chapter five summarizes the results, and offers recommendations from the study and suggests directions for future work

CHAPTER TWO
LITERATURE REVIEW

2.1 General Introduction

Chapter two explains the different methods that have been employed to synthesize nanoparticles and mainly focuses on the green synthesis techniques and why this technique is considered environmentally safer than physical and chemicals techniques that have been used in synthesis. This chapter also discusses solar cells and related work done on the solar cells, nanoparticles and technique used to synthesize nanoparticles. Therefore, the chapter also describe properties of SnO_2 under the structural, optical, and luminescence in its solar cell application. Lastly, group 13 elements regard the properties for Al and Ga being best dopants and co-dopants of SnO_2 on solar cell applications.

2.2 Solar Cells

A photovoltaic cell is a semi-conductor device that directly transforms solar power into electrical power. This phenomenon was discovered in 1839 by Antoine Cesar Bequerel (Pode *et al*., 2011) and is called the photovoltaic effect. Solar cell is typically named from the semiconducting material they are made of an example is the silicon based solar cell shown in Figure 2.1.

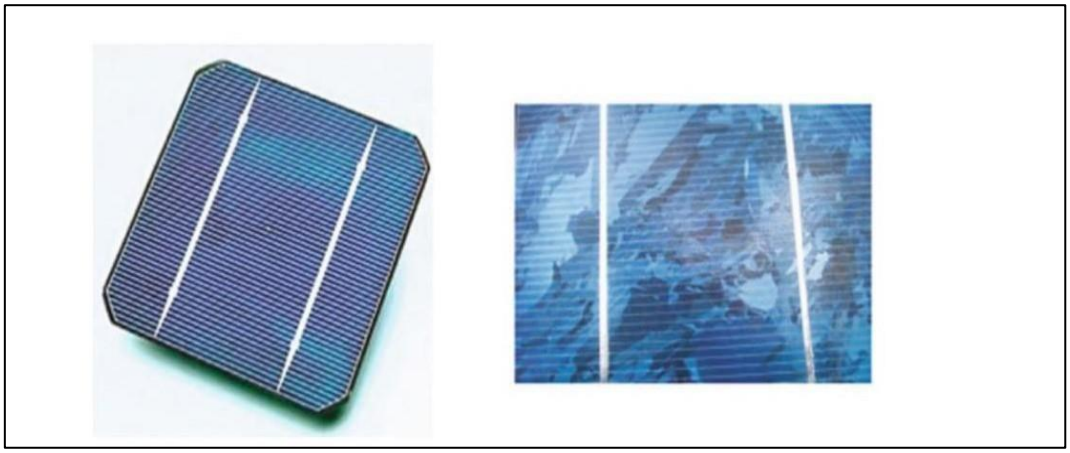


Figure 2.1: Silicon based photovoltaic solar cell (Pode *et al*., 2011)

Solar cells are the major components of solar panel. Solar cell do not rely on chemical reactions or fuel to generate electricity unlike batteries or fuel cells and operate without moving parts (Yuan *et al*., 2016). The materials utilized for solar cell must be capable of converting visible spectrum of sunlight into electricity (Darwish *et al.*, 2022). Figure 2.2 illustrate the basic structure of photovoltaic solar cell structure

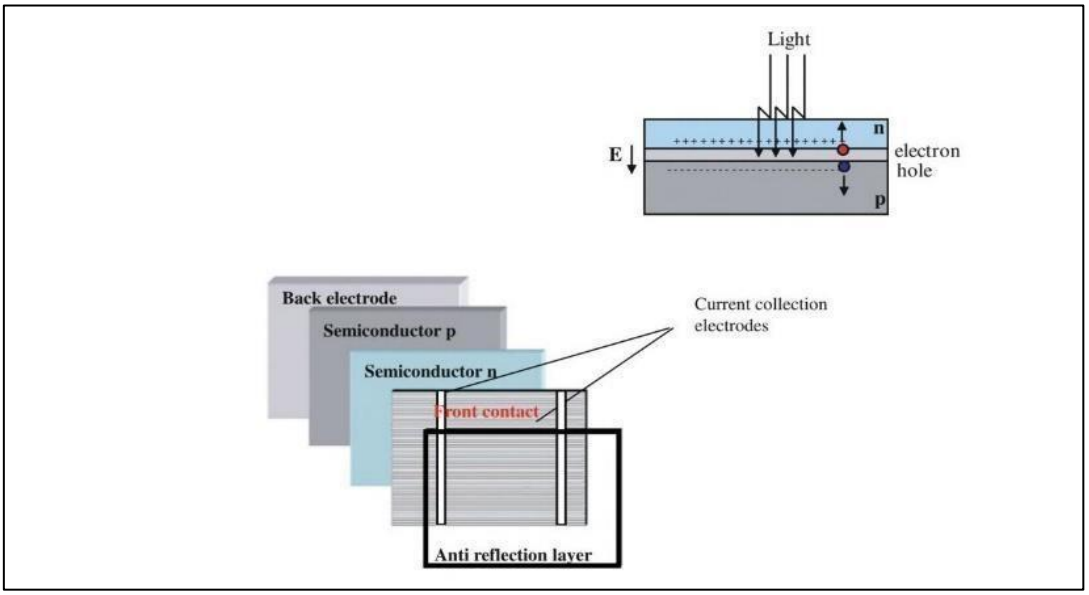


Figure 2.2: Basic structure of photovoltaic solar cell (Pode *et al*., 2011)

The incident photons from the sun excite the valence band electrons into the conduction band. Valence band has the least amount of unoccupied energy state, whereas the conduction band has the maximum occupied energy state. Insulators have extremely low conductivity and high resistivity therefore have high energy gap compared to semiconductors (Agrahari *et al.*, 2015). Figure 2.3 demonstrates the difference between insulators, semiconductors and conductors in terms of their band gap.

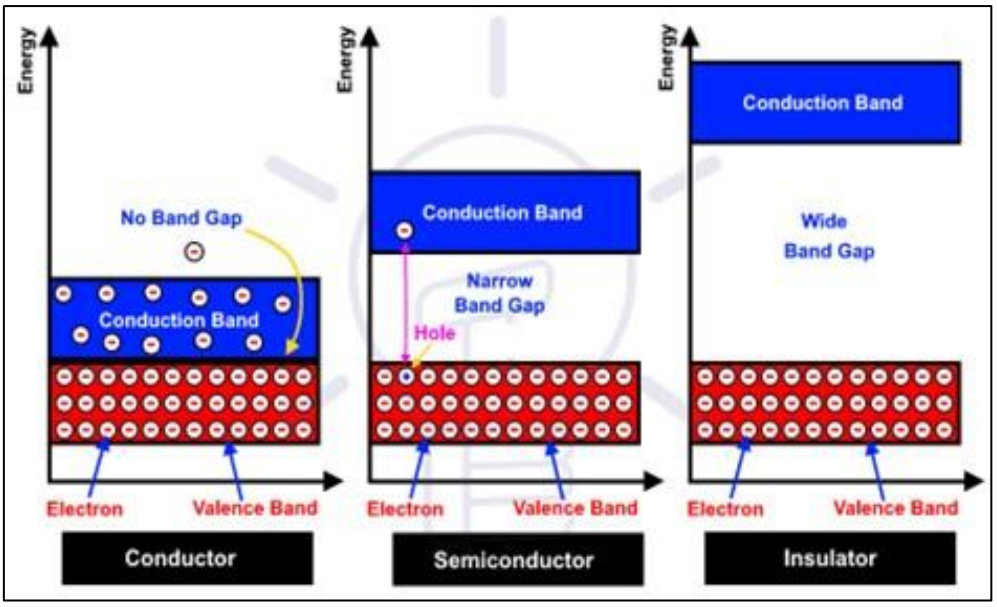


Figure 2.3: Differences between insulators, semiconductors and conductors (Agrahari *et al.*, 2015)

2.3 Metal Oxide Nanoparticles and their Applications

Properties of metal oxide such as magnetic, conducting, chemical and electronic properties can be modified by varying the specific size of the nanoparticle (Chavali *et al.*, 2019). Particles size significantly influences the electrical properties, particularly when utilizing oxides such as tin oxide (SnO_2), tungsten trioxide (WO_3) and indium (III) oxide (In_2O_3). Zinc oxide has found application in solar cells, mixed varistors, optoelectronics and in gas sensors (Sapkota *et al.*, 2021). One dimensional ZnO exhibits applications ranging from gas sensors to varistors (Choi *et al*., 2010). Because of their many potential uses, which range from magnetic storage devices (MSD) to contrast agents for magnetic resonance imaging (MRI). Iron oxides—specifically magnetite—are of special interest to materials scientists (Chavali *et al*, 2019)

Magnesium oxide has been used in the chemical industry to remove gaseous air contaminant such CO_2, CO, NO_x, and SO_x. It is also used as a cleaning material and catalyst in the synthesis of organic compounds. For industrial application, TiO_2 nanoparticles are utilized in solar cell, material science and pollution elimination.

SnO_2 is utilized as transparent conducting oxide due to its low electrical resistance, stability and high optical transparency (Dheyab *et al*., 2022). In a various optoelectronic device, such as solar cells, SnO_2 has been utilized as conducting electrode (Dheyab *et al*., 2022).

Zin oxide and SnO_2 have been recognized for solar cell application because of their wide direct band gap, large electron diffusion coefficient, excellent optical transparency high electron mobility (Ko *et al*., 2011). ZnO is a less preferred photoanode in DSSC applications due to its limited chemical stability and dye loading capacity. The problem with SnO_2 is that its low open circuit voltage (about 400 mV) and increased electron transport dynamics lead to a faster recombination rate, which restricts its overall photon-to-electron conversion efficiency (PCE) at moderate temperatures (Gubbala *et al.,* 2008). Several gases, including CO, NO, NH_3, H_2, O_2 and NH_2 have been detected using SnO_2 nanostructures at mild temperatures (Bhattacharjee *et al*., 2016).

2.4 Tin Oxide

Tin oxide belongs to a variety of transparent conductive oxides known as transparent conducting oxides (TCOs) (Chowdhury *et al.,* 2013). Due to its extensive use, tin oxide, a transparent conducting oxide (TCO), has drawn a lot of study interest and have been examined by numerous researchers (Dixon *et al.*, 2016). SnO_2 has been used in solar cells, gas sensors, transparent conducting electrodes, transistors, low-emissivity windows, and specific coatings for energy conversion (Buniyamin *et al.,* 2022). Recent studies have focused more on the transformed nanostructures due to their better qualities than the bulk material (Sagadevan *et al.*, 2015). SnO_2 is an n-type semiconductor with a direct band-gap energy of ~3.6 eV (Nilavazhagan *et al*., 2015). It is utilized in sensors to increase their sensitivity and reaction time due to its low density, high specific area, and strong stability (Wang *et al*, 2015).

Its high surface responsiveness, numerous active sites, and strong radiation absorption improve dye removal through photocatalysis (Bhattacharjee *et al*., 2015). It is used as an anode material in Li-ion batteries with high theoretical capacity. SnO_2 nanoparticles are also effective in solar cells because their band-gap responds to UV

irradiation (Zhou *et al.*, 2012). Tin oxide is classified as a post-transition metal oxide with a d^{10} electronic configuration (Wang *et al*., 2010). Doping SnO_2 nanoparticles with appropriate dopants improves their optical, structural, luminescent, and electrical characteristics (Altaf *et al*., 2023). The material's n type conductivity is influenced by naturally occurring donor type impurities (Bhuyan *et al.*, 2018).

SnO_2 is 97% transparent in the visible spectrum and has a resistivity of 10^{-4} –10^{-6} cm, which is lower than that of a semiconductor (Herklotz *et al*., 2023). Since tin exhibits two oxidation states (+2 and +4), two kinds of oxides are present: stannous oxide (SnO– romarchite) and stannic oxide (SnO_2– cassiterite), among the two SnO_2 is more stable than SnO (Tazikeh *et al*., 2014). As a photocatalyst, SnO_2 has been utilized to degrade broad range of environmental pollutants, including phenols, dyes and others (Vidhya *et al*., 2016).

2.5 Dopants

Doping is the intentional addition of contaminants into a material to modify its properties. Introducing dopants into transition metal oxide, properties like electrical properties are improved (Jiang *et al.*, 2017). Doping using appropriate impurities in the proper concentrations can significantly change a material's optical, structural and electrical properties (Altaf *et al.*, 2023)**.** Metal ion doping of the SnO_2 lattice produces oxygen vacancies and increases specific surface area (Singh *et al.*, 2017). Doping modifies the electrical property of a filament (Zhao *et al*., 2013). As the doping concentration increase, Zr-doped Ta_2O_5 shows voltage decrease (Kukli *et al.*, 2018). Magnesium doping in SnO_2 can reduce charge recombination and extend electron lifetime in DSSC devices (Duan *et al*., 2015). Ga doping replaces Sn atoms with reduced lattice deformation than Al and In, making it another viable p-type dopant for SnO_2 (Tsay *et al*, 2015). The most widely used dopants are Group-III elements like Al, Ga, and In because they are efficient donors (Kemuma *et al.*, 2024).

2.5.1 Gallium Doped Tin Oxide

Gallium is one among the dopant used to enhance properties of tin oxide. The band age of tin oxide rises when doped using Ga (Teh *et al*., 2013). Gass sensing properties of metal oxide are improved by doping using Ga (Hjiri *et al.*, 2015). Ga^{3+} can readily

replace Sn^{+4} in the SnO_2 lattice because its ionic radii Ga^{3+} (0.62 Å) are lower than that of Sn^{+4} (0.71 Å) (Tsay *et al,* 2015). The photovoltaic and photocurrent are higher when Ga-doped SnO_2 is utilized in photocatalysis than when undoped SnO_2 is used. Due to the differing sizes and structures of Ga and Sn, doping Ga^{3+} ions into SnO_2 is expected to promote photocatalytic activity and photoinduced charge separation of SnO_2 (Vidhya *et al.*, 2016). Accordingly, it is expected that Ga doped tin oxide will have excellent photocatalytic activity.

2.5.2 Aluminium Doped Tin Oxide

On earth's crust, Aluminium has been determined to be the most prevalent metal *(*Rabinovich *et al*, 2013). Oxygen vacancies are created when Sn^{+4} is exchanged for Al^{+3}, which is advantageous for photodiode and photovoltaic applications (Kethzy *et al*., 2019). A lower valency cation as acceptor impurity such as Al^{3+} in tin oxide decreases n-type conductivity and increases the hole concentration and hence the p-conductivity (Benouis *et al*., 2014). High transparency in the visible spectrum is created through tin oxide doping with Al to generate transparent conductive oxide (Bagheri *et al.,* 2004). Aluminium has excellent heat and electrical property making it suitable for transparent conducting oxide (Agura *et al*., 2003). Al-doped SnO_2 nanoparticles synthesized in the current study record good optical, surface and electrical characteristic that increase their suitability for potential photovoltaic use (Panneer *et al*., 2023).

2.6 Crystalline Structure of Tin Oxide

Tin oxide is an ionic compound with the lattice properties measured by x-ray diffraction obtained as a = 4.737 Å, c = 3.185 Å and u = 0.672 in an ideal tetragonal rutile structure. Two types of oxide are possible as tin present two oxidation states +2 and +4; stannic oxide (SnO_2) and stannous oxide (SnO) in which SnO is less stable than SnO_2. The structure contains three Sn^{4+} ions, which take up the three corners of an equilateral triangle and six oxygen ions encircle anions of oxygen (Altaf *et al*., 2023). Tin oxide and oxygen has a coordination geometry of octahedral and trigonal planar respectively with coordination number of 3 for oxygen and 6 for Sn atom.

2.7 Synthesis of nanoparticles

Nanoparticles can be produced via physio–chemical methods (Singh *et al.,* 2015). Nanoparticles synthesis can be bottom up or top down as shown in Figure 2.4.

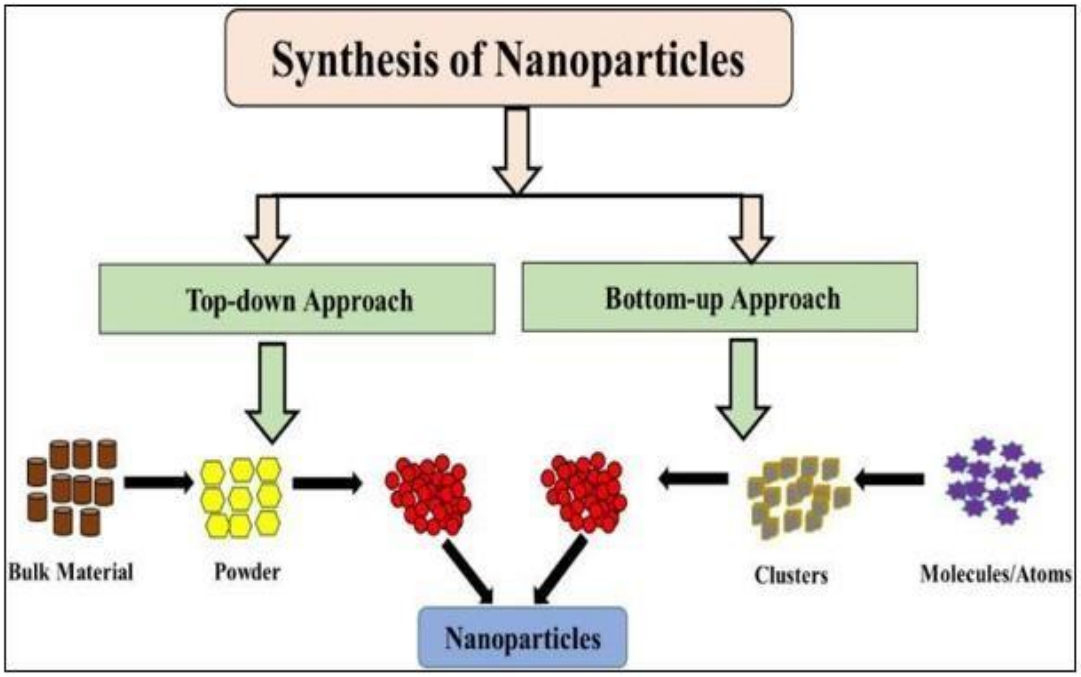


Figure 2.4: Top-down and Bottom-up approach for synthesizing nanoparticles (Anu et al., 2017)

The methods of NPs synthesis are grouped into chemical, biological and physical methods as shown in the Figure 2.5 Growth parameters like pH, salt content, temperature and exposure duration have a substantial effect on the nanoparticles size and structure (Gopinath *et al*., 2016) Some of the common method used are sol gel method, chemical precipitation and green synthesis methods. These technique presents numerous challenges such as reliance on harmful solvents and production of harmful waste materials making it financial intensives (Feinle *et al*., 2016).

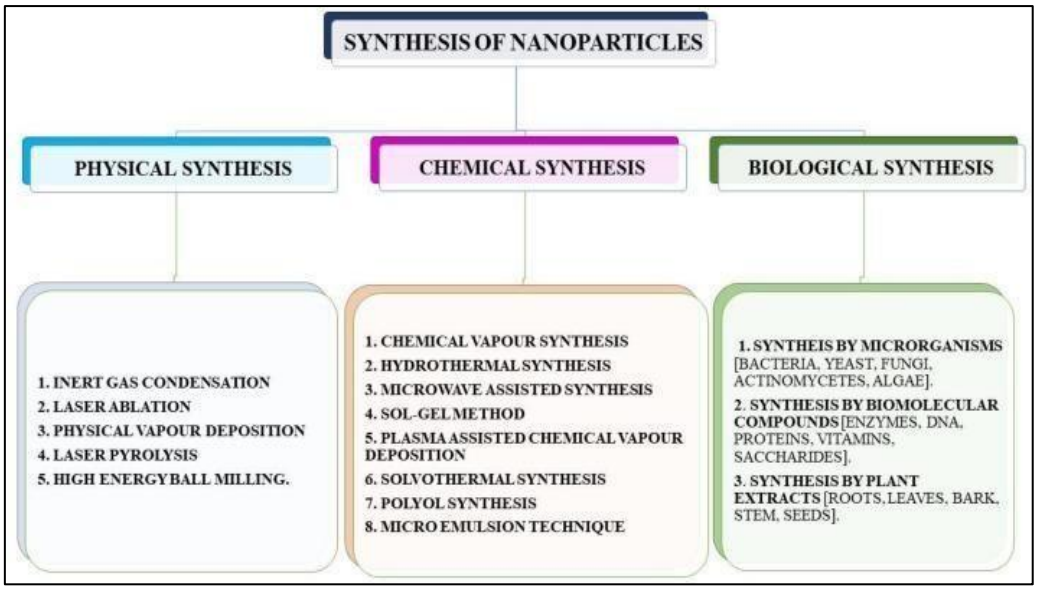


Figure 2.5: Physical, chemical and biological synthesis of nanoparticle (Singh et al., 2015)

2.7.1 Sol gel Method

Sol gel method is widely used in industry (Feinle *et al.*, 2016). This approach entails information of inorganic suspension known as sol and its gelation in an ongoing form of liquid forming a gel (Rheima *et al.,* 2020). Sol-gel technique involves several steps as highlighted in the Figure 2.6 and is able to produce high-quality nanoparticles of the same size (Rahman *et al,* 2012). More than one type of nanoparticles can be produced simultaneously (Adam *et al.,* 2011). The precursor used in this method are metal oxide and chlorine (Ramesh *et al,* 2013). The end product is created through a series of irreversible chemical reactions (Bai *et al.*, 2012). Factors such as pH, concentration, type of solvent and temperature affects the rate of reaction of salt. The hydrolysis process results in the formation of a sol and when condensed leads to the formation of a gel. It produces solid materials from small molecules mainly from metal oxides which involves the transformation of monomers into a sol (colloidal solution) as the precursor to form a gel (Nachit *et al*., 2022). The gel is created by linking cavities to transform the cell's density into a three-dimensional structure.

The cell density is converted to cavities to create a three-dimensional structure to produce a gel (Yue *et al*., 2013). Volumetric shrinkage makes the gel to dry, producing a solid and stiff structure (Yue *et al.,* 2013). In this method, nanosized porosity are achieved by controlling the drying condition of the gel (Hassan *et al*., 2013). Sol can be converted into gel by varying the solution and pH content (Shinde *et al.*, 2012). The removal of solvent is done by drying as shown in Figure 2.6 since drying prevents the formation of cracks (Cuce *et al*., 2014).

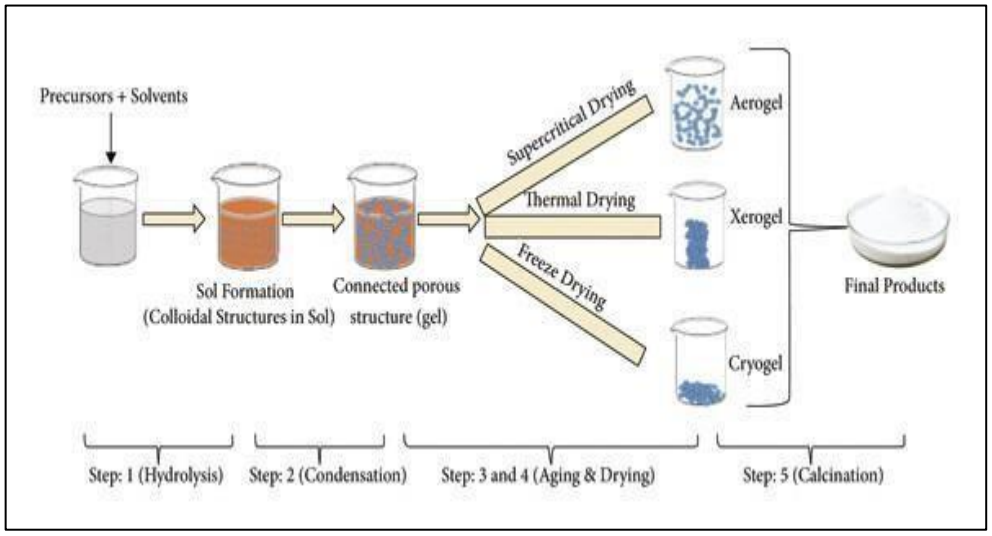


Figure 2.6: Different stages of sol-gel process (Patil et al., 2020)

2.7.2 Chemical Precipitation

Chemical precipitation method is ideal for creating nanostructured material due to its inexpensive cost and its flexibility to adjust the crystalline grain size (Priyadharsini *et al*., 2017). Nanoparticle with the highest optical and photocatalytic activity is produced by the chemical precipitation process (Changchun *et al*., 2011). The synthesis involves reaction of the component materials in the appropriate solvent. Size management is done by the arrested precipitation technique (Rajput *et al.,* 2015). After the particles and crystals are separated by centrifugation, they are cleaned and vacuum-dried using surfactant to keep them apart. Temperature, pH, concentration

and solvent type are some of the variables that impact how quickly salt reacts (Sharma *et al*., 2009).

2.7.3 Green Synthesis Method

Green synthesis strategy involves use of natural product like fruit, flowers or crop leaves (Figure 2.7) to substitute hazardous chemicals (Hussain *et al*., 2016). This method is rapidly gaining importance over other methods as it has a less chance of failure, low cost, environmentally friendly and nontoxic (Bansal *et al*., 2015). The utilization of vitamins, amino acids and plant extracts is gaining popularity (Annadhasan *et al*., 2015)

Metal precursors can be biogenically reduced to their corresponding NPs without harming the environment (Jayaseelan *et al*., 2012) its enduring (Gopinath *et al.,* 2016) and is less costly (Mittal *et al*., 2013). The capping and stabilizing substances found in biological entities are necessary for acting as growth terminators and preventing the aggregation/agglomeration process (Kharissova *et al*., 2013).

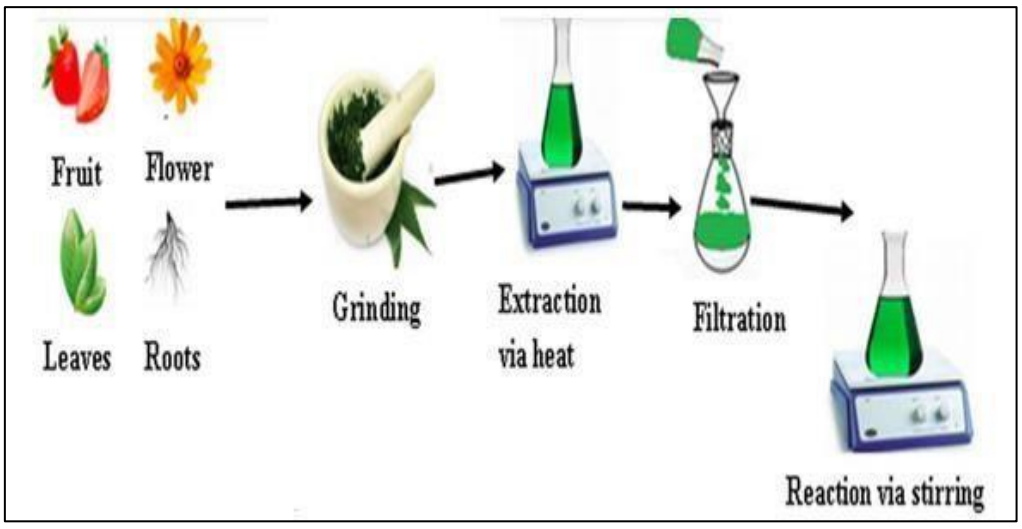


Figure 2.7: Schematic diagram of plant extract-mediated synthesis of SnO_2 (Gebreslassie et al., 2021)

Metal oxide NPs have been synthesized by use of green synthesis method and the nanoparticles dimensions fluctuate with concentration of leaf solution. SnO_2 NPs has successfully been synthesized by use of *Camellia sinensis* leaf extract (Selvakumari *et al.*, 2017). The anticancer, antibacterial and antioxidant properties of triterpenoid acids, flavonoids, sesquiterpene alcohols and phenolic compounds have been found in guava leaf extracts (Qin *et al*., 2017). Leaf extract contains phenolic compounds which act both as caping and stabilizing agent. By using *Psidium guajava,* at 314 nm, the UV-Vis data showed a surface plasmon resonance peak verifying SnO_2 NPs formation and the spherical NPs with size ranging from 8 to 10 nm (Gebreslassie *et al,* 2021). Figure 2.8 shows Guava plant, leaves and fruit.



Figure 2.8: *P. guajava* (Guava) plant in its habitat (Patil et al., 2020)

2.8 Analytical Techniques used to Characterization nanoparticles

Characterization is the study of material properties such as structural, composition, magnetic, electrical, chemical and physical properties. Regarding innovation and inventions, several techniques are employed to help analyse whether the synthesized compound's desired morphology, structure, optical and electronic properties have been achieved. A wider characterization of nanoparticles is necessary where

complementary techniques can be married together and validate a hypothesis. As analysis is factored in, physical and chemical composition can be evaluated using multiple techniques based on their strengths and limitations. This research analyses the structural and optical properties of synthesized nanoparticles. Functional group is identified by use of as Fourier Transform infrared spectroscopy (FT-IR), Ultraviolent Visible spectroscopy (UV-Vis) are used to analyse the absorbance, X-ray diffraction (XRD) technique analyses the crystalline structure of NPs and Scanning electron microscopy (SEM) provide details about morphology of NPs.

2.8.1 Fourier Transform infrared spectroscopy (FT-IR)

Functional group present in a molecule are identified by Infrared spectroscopy as it measures the vibration frequency of a molecule (Shankar *et al*, 2015). The principle that acts on FTIR is based on passing infrared IR radiation through a sample where light of the correct wavelength is absorbed and records the absorption or transmission bands. An interferogram gives the interferometer output as a graph, converted into a spectrum graph of infrared spectroscopy. The spectrum is plotted on a graph where the transmittance recorded is plotted against wave number (Dutta *et al.*, 2017). FTIR is preferred over another method as it is a constructive sample analyser, fast than other analysis instruments, and much more sensitive and precise. The analytical technique is used to identify components in a mixture of organic, inorganic, and polymeric materials, pharmaceutical industry, food analysis, and petrochemical engineering.

The FTIR spectrum has two regions that is at fingerprint region < 1500 cm^{-1} and functional group region > 1500 cm^{-1}. The fingerprint region shows the vibrations of the compound and ranges between 700 and 1500 cm^{-1}. To determine the functional group present in a NPs, a frequency region from 4000 to about 1250 cm^{-1} is required and the range of IR spectrum is 4000-1500 cm^{-1}. The vibration is classified into stretching and bending vibration. Stretching vibration which is classified into symmetric stretching where there is simultaneous vibration of bonds that elongate and contract together and anti-symmetric stretching where one bond gets longer as

the other gets shorter and goes in opposite directions. The frequency at which a molecule naturally vibrates is the same as the frequency that is absorbed. The amplitude of vibration motion increases due to the energy absorbed by the bond in a molecule. The sample absorb some of the IR radiation while some are transmitted through it (Smith *et al*, 2011). FTIR allows the acquisition of multiple interferogram of same sample as it receives an interferogram in not more than a second. Infrared photons have enough energy to make a collection of atoms vibrate in respect to the bond that holds them together. The energy of infrared photons is sufficient to cause a collection of atoms to vibrate with relation to the bond holds them together. The transformation is executed by a computer, which then delivers spectral information to the user for analysis (Micheli *et al.*, 2017).

2.8.2 Ultraviolent Visible spectroscopy (UV-Vis)

UV-Vis spectroscopy is a technique that involves shining Ultraviolet (UV) or visible (Vis) light on a compound. The main emphasis of ultraviolet-visible spectroscopy is the interaction of molecules with UV visible radiation. Two modes of operation are the absorbance mode and the transmittance mode. When a sample takes in light of a suitable wavelength and an electron is promoted to a high energy molecular orbital, the molecule is in then excited state. In the absorbance mode, the quantity of light absorbed by the compound is measured as a function of wavelength, and a graph of absorbance against wavelength is obtained; this graph is known as an absorption spectrum.

In the transmittance mode, the amount of light transmitted through the sample is measured as a function of wavelength: this graph is known as a transmittance spectrum. UV-Vis analyse the optical characteristic of nanoparticles which are affected by shape, agglomeration, size, concentration and refractive index near NPs surface (Blanco *et al,* 2014). UV-visible spectroscopy allows for the study of NP arrangement because of their surface plasmon reverberation assimilation band (Abdelghany *et al*., 2018).

2.8.3 X-ray diffraction (XRD)

X-ray diffraction (XRD) is an instrument utilized to characterize crystalline materials. X-Ray diffraction spectroscopy (XRD) is regarded as the most efficient and reliable non-destructive analytical instrument in the analysis of nanoparticles. As X-rays are passed through a powdered material, they interact with the atoms in the material, producing a diffraction pattern. The obtained pattern provides details on various parameters of material such as crystallinity, structures and preferred crystal orientations (texture). A monochromatic X-ray beam scattered across a surface produces X-ray diffraction peaks at specific angles (Bunaciu *et al*., 2015). XRD is utilized in several industries such as power generating, aircraft and microelectronics (Ameh *et al*., 2019). The technique is used *in situ* studies as it is non-destructive and non-contact (Anandalakshmi *et al*., 2016).

2.8.4 Photoluminescence spectroscopy (PL)

Photoluminescence spectroscopy (PL) is an excellent instrument for identifying the kind of oxygen vacancies found in nanomaterials. PL provides information on the emission that is the near band emission and the deep level emission. SnO_2 emission spectra display peak correlating to defects such as tin interstitials, oxygen vacancies and dangling bonds. The light emitted by the atom or molecule are monitored by Photoluminescence spectroscopy. Optical (photon) absorption or photoexcitation is the process that produces photoluminescence among the different radiative processes (Aoki *et al.,* 2012). Plasmonic nanostructures of different shape are utilized to obtain single-photon and milti-photon excitation PL (Zhang *et al*., 2014).

2.9 Chapter Summary

Chapter two comprehensively reviewed the literature pertaining to the synthesis and characterization of nanoparticles. It also examined the intrinsic properties of SnO_2, including its structural, optical, and luminescence characteristics, as well as its applications in solar cell technology. Furthermore, the literature review discussed the properties of aluminium and gallium as dopants, highlighting their significance in modifying the properties of SnO_2 nanoparticles. By synthesizing

existing research findings, this chapter provided a comprehensive understanding of the factors influencing the synthesis and performance of doped tin oxide nanoparticles, laying the groundwork for the experimental investigations conducted in subsequent chapters.

CHAPTER THREE
MATERIALS AND METHODS

3.1 Introduction

Synthesis of tin oxide nanoparticles can be carried out through several methods including solgel, co-precipitation, chemical vapour decomposition, green synthesis method among others. Green synthesis method was chosen to synthesize tin oxide, aluminium and gallium doped tin oxide and Al:Ga co-doped tin oxide to investigate structural, luminescence and optical properties for possible solar cell application.

3.2 Materials

All the chemicals that were used were of analytical grade and were used without any form of purification. All chemicals were purchased from Sigma Aldrich & A.B Chem. Co., Ltd. They include stannous chloride dihydrate ($SnCl_2.2H_2O$) (>98%), gallium (III) nitrate hydrate ($Ga(NO_3)_3.XH_2O$) (>99.9%), aluminium nitrate nanohydrate ($Al(NO_3)_3.9H_2O$) (>98%), absolute ethanol (C_2H_5OH) (>99%) and deionized water. Deionized water was prepared at Murang`a university research lab.

3.3 Methods

This section involves the synthesis of nanoparticles and has been arranged according to specific objectives

3.3.1 Preparation of *Psidium guajava* leaf extract

Guava leaves (*Psidium quajava*) were collected from a farm in Murang'a County near Murang`a University of Technology, Kenya. County is located in central Kenya at latitudes of 0° 34' S and 1° 7' S and longitudes 36° E and 37°27' E**.** The samples were first cleaned using running tap water followed by deionized water to remove surface contaminants. The washed leaves were dried in an oven at 50 ℃ for 5 hours before crushing using a blender. 4.0 g of the sample was introduced to 100 ml of deionized water and heated at temperature of 60 ℃ for 30 minutes. After cooling to room temperature, the mixture was filtered using 1 mm Whatmann filter paper (Figure 3.1) (Kumar *et al*., 2018) and stored in a refrigerator to be used as capping agent in the synthesis.

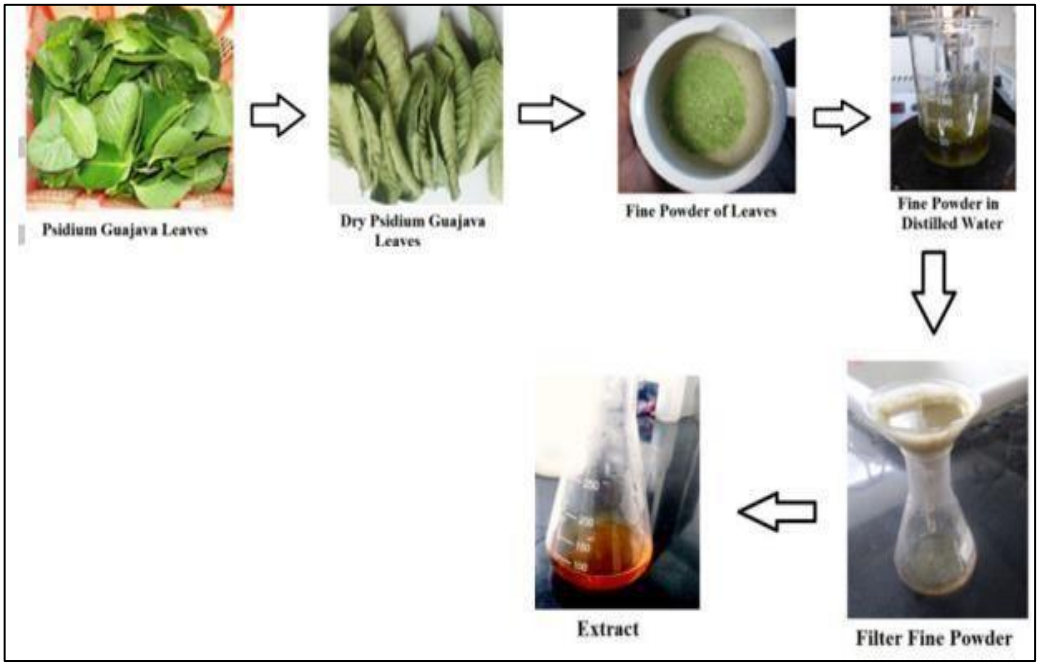


Figure 3.1: Schematic representation of *P. guajava* leaves extract preparation

3.3.2 Synthesis of pure tin oxide NPs without *P. guajava* extract

Tin chloride dihydrate (1.35378 g) was dissolved in 30 ml deionized water and stirred for 10 mins at room temperature until fully dissolved. Ammonium hydroxide was added to the solution dropwise to maintain a pH of 9. The mixture was refluxed at 60 ℃ for 3 hours. The resulting solution was aged for 24 hours then washed using a 70:30 mixture of deionized water and ethanol. The product was dried in a laboratory oven (MEGA O 50 model) at 100 ℃ for 2 hours. The particles formed were annealed in a muffle furnace at a temp of 500 ℃ for 3 hours (Singh *et al.*, 2019).

$$SnCl_4.2H_2O + 4NH_4OH \rightarrow SnO_2 + 7H_2O + 4NH_4Cl$$

3.3.3 Synthesis of tin oxide nanoparticles using *P. guajava* leaf extract

Tin (II) chloride dihydrate (1.35378 g) was dissolved in 30 ml deionized water and stirred for 10 mins at room temperature until all salt dissolved. Then, 30ml of *psidium guajava* extract was added to the solution, as shown in Figure 3.2 (Kumar *et al*., 2018). Ammonium hydroxide was added dropwise to maintain the pH to 9. The

reaction mixture was then refluxed at 60 ℃ for 3 hours on a magnetic stirrer. The solution was aged for 24 hours, washed using a 70:30 mixture of deionized water and ethanol, and then dried in a laboratory oven (MEGA O 50 model) at 100 ℃ for 2 hours. The particles formed were annealed in a muffle furnace at 500 ℃ for 3 hours.

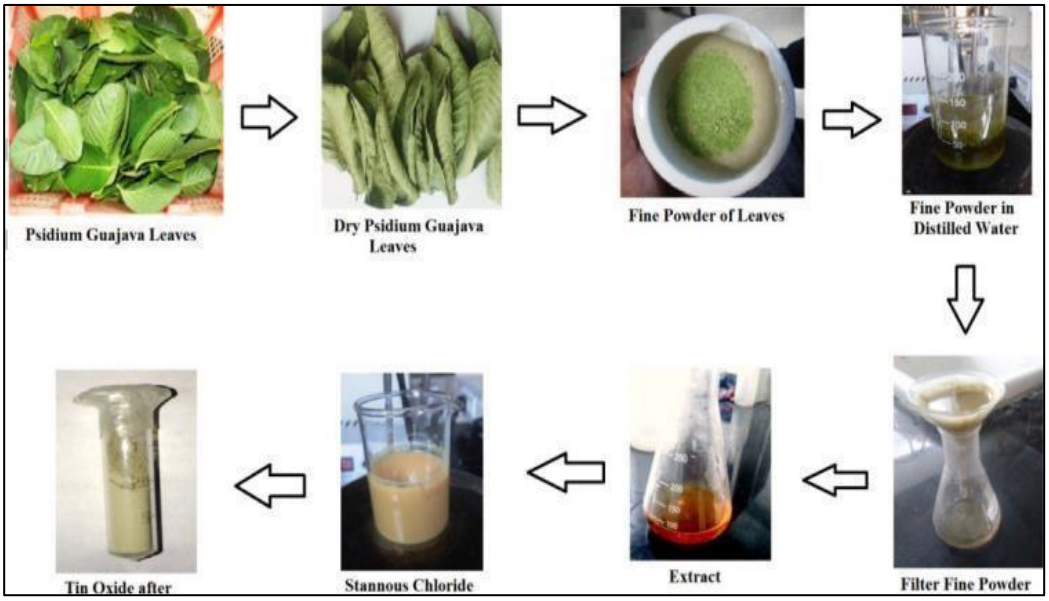


Figure 3.2: SnO_2 NPs preparation using *P. guajava* leaf extract

3.3.4 Synthesis of gallium doped tin oxide NPs without *P. guajava* extract

Tin (II) chloride dihydrate (1.35378 g) was dissolved in 30 ml of deionized water and stirred for 10 mins at room temperature until all the salt dissolved. Ammonium hydroxide was added to the solution to maintain a pH of 9, after which different mol % of gallium (III) nitrate hydrate (0.5 %, 1 %, 1.5 %, 2 % and 2.5 %) was added. The mixture was refluxed at 60 ℃ for 3 hours. Aging process was allowed for 24 hours then the product was washed using a 70:30 mixture of deionized water and ethanol, and dried in a laboratory oven at 100 ℃ for 2 hours. The particles formed were annealed in a muffle furnace at a temp of 500 ℃ for 3 hours (Vidhya *et al*., 2016).

$$SnCl_2.2H_2O + Ga(NO_3)_3.5H_2O + 2H_2O \rightarrow Ga_xSnO_X + HNO_3 + H_2O$$

3.3.5 Synthesis of gallium doped tin oxide NPs using *P. guajava* extract

Tin (II) chloride dihydrate (1.35378 g) was dissolved in 30 ml of deionized water and stirred using magnetic stir for 10 minutes at room temperature until all the salts dissolved. Then, 30 ml of *Psidium guajava* extract was added, followed by the dropwise addition of ammonia hydroxide to raise the pH to 9. Different mole percentages (0.5%, 1%, 1.5%, 2% and 2.5%) of gallium (III) nitrate hydrate were added, and the mixture was refluxed at 60 ℃ for 3 hours. Aging process was allowed for 24 hours then washed using a 70:30 mixture of deionized water and ethanol, before drying in a laboratory oven at 100 ℃ for 2 hours. The particles formed were annealed in a muffle furnace at a temp of 500 ℃ for 3 hours.

3.3.6 Synthesis of aluminium doped tin oxide without *P. guajava* extract.

Tin (II) chloride dihydrate (1.35378 g) was dissolved in 30 ml of deionized water and stirred using magnetic stir for 10 mins at room temperature until all the salt dissolved. Ammonium hydroxide was added to the solution dropwise to maintain a pH of 9. Different mol% of aluminium nitrate nanohydrate (0.5%, 1%, 1.5%, 2% and 2.5%) was added and refluxed at 60 ℃ for 3 hours. Aging process was allowed for 24 hours then washed using a 70:30 mixture of deionized water and ethanol, followed by drying in a laboratory oven at 100 ℃ for 2 hours. The particles formed were annealed in a muffle furnace at a temp of 500 ℃ for 3 hours.

3.3.7 Synthesis of aluminium doped tin oxide nanoparticles with *P. guajava* extract.

Tin chloride dihydrate with a mass of 1.35378 (g) was dissolved in 30 ml of deionized water and stirred for 10 mins at room temperature. 30 ml of *Psidium guajava* extract was added after which ammonia hydroxide was added dropwise to raise the Ph to 9. Different mole % of Aluminium Nitrate Nanohydrate (0.5%, 1%, 1.5%, 2% and 2.5%) was added and the mixture refluxed at 60 ℃ for 3 hours. Aging process was allowed for 24 hours before washing using a 70:30 mixture of deionized water and ethanol, dried in a laboratory oven at 100 ℃ for 2 hours. The particles formed were annealed in a muffle furnace at a temp of 500 ℃ for 3 hours.

3.3.8 Synthesis of Al-Ga co-doped tin oxide NPs without *P. guajava* leaf extract.

Tin (II) chloride dihydrate (1.35378 g) was dissolved in 30 ml of deionized water and stirred for 10 mins at room temperature. 30 ml of *Psidium guajava* extract was added after which ammonia hydroxide was added dropwise to raise the pH to 9. Different mole % of aluminium nitrate nanohydrate (0.5%, 1%, 1.5%, 2% and 2.5%) were added and the mixture refluxed at 60 ℃ for 3 hours. Aging process was allowed for 24 hours before washing using a 70:30 mixture of deionized water and ethanol, followed by drying in a laboratory oven at 100 ℃ for 2 hours. The particles formed were annealed in a muffle furnace at a temp of 500 ℃ for 3 hours.

3.3.9 Synthesis of Al-Ga co-doped tin oxide NPs using *P. guajava* leaf extract

Tin (II) chloride dihydrate (1.35378 g) was dissolved in 30 ml of deionized water and stirred for 10 mins at room temperature. 30ml of *Psidium guajava* leaf extract was added under continuous stirring after which ammonium hydroxide was added to raise pH to 9. Weighed mass of aluminium nitrate nanohydrate and gallium nitrate hydrate (25%:75%, 50%:50% and 75%:25%) was added to the solution and refluxed at 60 ℃ for 3 hours (Doyan *et al*., 2021). Aging was allowed for 24 hours before washing using a 70:30 mixture of deionized water and ethanol, then drying in a laboratory oven at 100 ℃ for 2 hours. The particles formed were annealed in a muffle furnace at a temp of 500 ℃ for 3 hours.

3.4 Characterization of the synthesized nanoparticles

3.4.1 The UV-Vis characterization

UV-Vis spectrophotometer model Evolution One Plus (Figure 3.3) was used to determine the absorbance in the material. The instrument was turned on and 20 minutes was allowed to warm up after which the bulk (deionized water) was used to autozero the machine. A wavelength (200-800 nm) and the type of analysis (absorbance) was selected. The sample was placed in cuvette and the quantity of light absorbed was measured as a function of wavelength, and a graph of absorbance against wavelength was obtained; this graph is known as an absorption spectrum. The optical energy band gap was calculated using Tauc's equation (Equation 3.1) (Abbas *et al.*, 2020)

$$(\alpha hv)^n = \beta(hv\text{-}E_g) \qquad (3.1)$$

Where α is the optical absorption coefficient, h is the planks constant, v is the photon frequency, Eg is the band gap, β is the proportional constant, and n is the electronic transition. n can be 2 or $\frac{1}{2}$ for direct and indirect allowed transition respectively or can be $\frac{2}{3}$ or $\frac{1}{3}$ for direct and indirect forbidden transition respectively. Optical band gap values were estimated by drawing a tangent of $(\propto hv)^2$ on Tauc's plot and extrapolating to the $(\propto hv)^2 = 0$ x-axis.



Figure 3.3: UV-VIS spectrophotometer at Murang'a University of Technology

3.4.2 XRD Characterization

X-Ray diffraction analysis (XRD) is a non-destructive technique that provides detailed information about the crystallographic structure, chemical composition, and physical properties of a material. XRD diffractometer mode EQUINOX 100 (Figure 3.4) was used in the analysis, where the machine was first turn on and given 30 minutes to warm up. It was operated at a 40 kV and current of 0.9 mA with a wavelength of 1.5406 Å. The nanoparticles were ground into fine powder using

pestle and mortar and placed on the sample holder of the XRD instrument. The excel data obtained was used to plot the diffraction peaks using origin software. Bragg's law equation as shown in Equation 3.2 was used to determine the interplanar spacing (Bett *et al.*, 2024)

$$n\lambda = 2d\sin\theta \qquad (3.2)$$

where d is interplanar spacing, θ is Bragg's angle of incidence, n is the order of the diffraction beam and λ is the x-ray wavelength.

The crystalline size (D) was calculated from the peak broadening of diffraction peak using Debye Scherer formula (Equation 3.3) (Venugopal *et al*., 2014)

$$D = \frac{k\lambda}{\beta\cos\theta} \qquad (3.3)$$

Where λ is the incident wavelength (1.5406 Å), β is the full width at half maximum intensity (rads), θ is the Bragg diffraction angle, D is the crystallite size (nm), and k is the Scherer constant (0.9).



Figure 3.4: XRD diffractometer EQUINOX 100 at Murang'a University of Technology

3.3.3 Photoluminescence characterization

The spectrophotometer (Figure 3.5) was first turn on after which it was given 20 minutes to warm up. The sample was dissolved in deionized water and then loaded on a transparent cuvette and laser lamp was used to excite nanoparticles. The spectrometer displayed the emitted light onto a detector. The excel values obtained was plotted with the help of origin software.

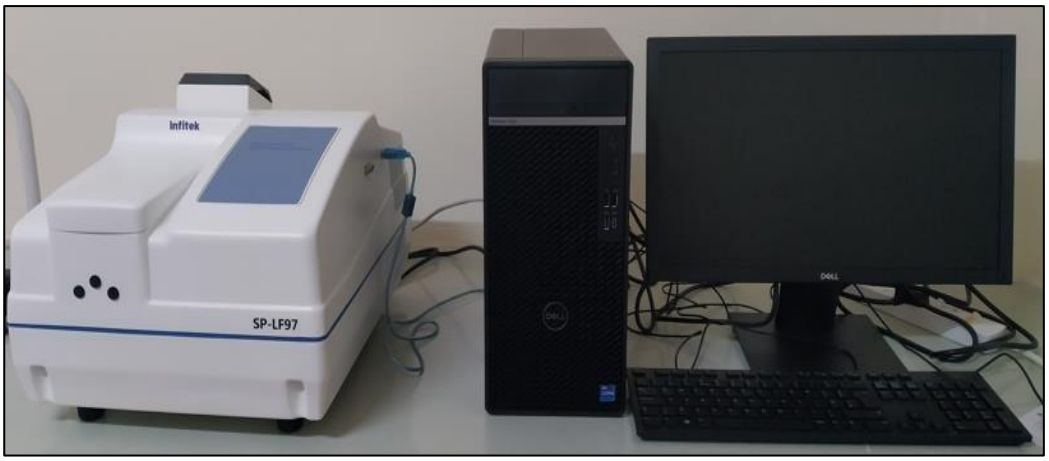


Figure 3.5: Photoluminescence spectrophotometer (PL) at Murang'a University of Technology

3.4.4 FT-IR characterization

Fourier transform infrared spectrophotometer (FTIR) (Figure 3.6) was first turned on and allowed to warm up, the background measurements was obtained by scanning empty sample holder in the ATR. It was calibrated using standard reference (polystyrene film). The powder sample was placed on the sample holder then scan at a wavelength of 400-4000 cm^{-1} to obtain the spectrum. The spectrum obtained was analyzed to determine the functional group present in the finger print and functional group region. FTIR has two types of vibration: stretching and bending vibration. Stretching vibration is classified into symmetrical and anti-symmetrical and occurs when the interatomic distance continuously changes along the bond axis bond between two atoms. The vibration is called bending vibration when there is a change in the angle between two bonds. Bending vibrations occur in the same plane for which we can have wagging, scissoring, twisting, or rocking vibrations (Khan *et al*., 2018)



Figure 3.6: FT-IR spectrophotometer at Murang'a University of Technology

3.5 Chapter Summary

This chapter extensively discussed the material used, the synthesis method as per the objective and the characterization techniques employed to analyse data. The nanoparticles were synthesized via green synthesis method using *P. guajava* leaves extract. The characterization technique employed include FT-IR, UV-Vis, Pl and XRD

CHAPTER FOUR
RESULTS AND DISCUSSION

4.1 Introduction

This chapter discuss the results obtained from the study. The results have been discussed according to the specific objectives. It entails the effects of capping agent on tin oxide NPs, effects of varying Al and Ga doping concentration on tin oxide NPs and effects of Al:Ga co-doping on structural, optical and photoluminescence properties of tin oxide NPs.

4.2 Characterization undoped tin oxide nanoparticles with and without *p. guajava* leaf extract as capping agent

As part of the first objectives of this research, synthesis of tin oxide nanoparticles was accomplished by use of green synthesis method. It involves utilizing *P. guajava* extract as a capping agent. The results synthesized nanoparticles were also characterized by FTIR, PL, UV-Vis and XRD.

4.2.1 Optical analysis of undoped tin oxide nanoparticles

Figure 4.1 shows the absorbance spectra of synthesized tin oxide with and without *P. guajava* extract, measured in the 200-800 nm range. Absorption peaks were observed at 308 nm and 290 nm for capped and uncapped samples, respectively. The variation in the absorbance is attributed to the presence of various phytochemicals in the guava leaves, which contributes to the formation of Sn^{4+} (Binadi *et al*., 2025). The absorption band arises from the photoexcitation of the electrons from valence band (VB) to conduction band (CB) (Agrahari *et al.*, 2015). Unlike bulk tin oxide, which exhibits an absorption peak at 337 nm (Subramaniam *et al*., 2018), the synthesized samples display a shift due to the quantum confinement effect (Ahmed *et al*., 2011). When nanoparticle size falls below this threshold, quantum confinement leads to energy level quantization and an increased band gap. Absorbance of 298 nm for tin oxide nanoparticles synthesized using *P. juliflora* extract was previously reported (Govindasamy *et al*., 2024)

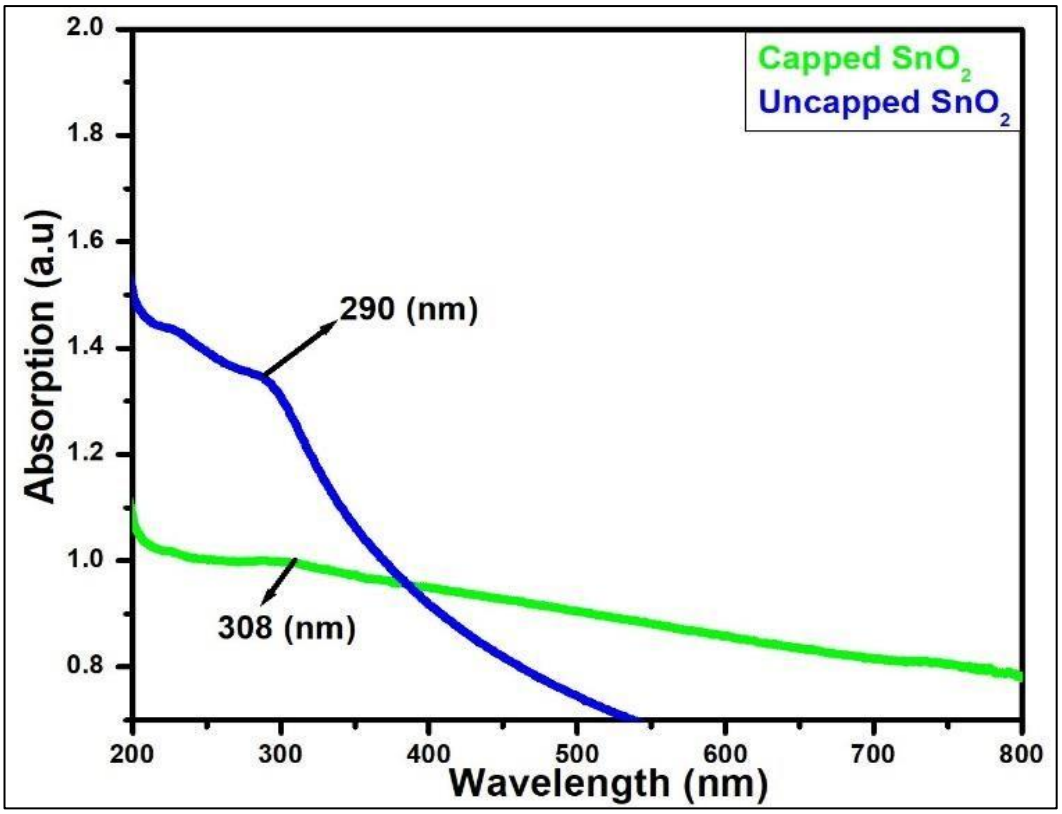


Figure 4.1: Absorbance spectrum of synthesized SnO_2 with and without p. guajava extract

The optical band gap energies of both capped and uncapped SnO_2 were quantitatively determined by utilizing the Tauc's plot equation (Equation 3.1) (Jepngetich *et al.,* 2025), which is an estimated technique for estimating semiconductors band gap energy from its absorbance spectrum. Figure 4.2 shows a plot $(\alpha hv)^2(eV\ cm^{-1})^2$ against photon energy (hv) (eV). The band gap energy was obtained by extrapolating the linear portion of each curve (the rising edge) to the x-axis, the band gap energy is estimated as the x-intercept. Deviations from the ideal crystal structure, growth imperfections, oxygen vacancies, and quantum effects in nanoparticles can alter the energy band structure and affect band gap. From figure 4.2 the band gap energy of 3.98 and 3.21 eV was obtained for capped and uncapped SnO_2 respectively.

Capped and uncapped SnO_2 NPs were found to have a higher and lower band gap value compare to the bulk value (3.6 eV) (Ahmed *et al*., 2011) respectively. For capped sample, the difference is due to the electron quantum confinement effect. When nanoparticle size falls below this threshold, quantum confinement leads to energy level quantization and an increased band gap. As a result, capped SnO_2 nanoparticles exhibit larger band gap energy as compared to the bulk and similar result were previously reported by Binadi *et al.*, 2025 and Kumar *et al.,* 2018. The variation is due to the changes in the morphologies, particle size and surface microstructure (Binadi *et al.,* 2025). A blue shift in the band gap was reported for capped SnO_2 using *Prosopis juliflora* and uncapped method (Nagirnyak *et al*., 2016).

For uncapped sample the band gap was lower than that of the bulk which is in agreement with previous reports (Doyan *et al*., 2018), *(*Nagirnyak *et al*., 2016) and (Thankaian *et al*., 2022). The deviation in energy gap values from the energy gap of bulk tin oxide is explained by a combination of the drop in surface charge distribution and the significant quantity of oxygen vacancies preserved in the material (Thankaian *et al*., 2022). This is in contrast to the normal phenomenon of quantum confinement even though the size decreases. These findings concur with earlier research work, and offer a deeper understanding of the electronic structure of the SnO_2 NPs synthesized through different methods (Nagirnyak *et al.*, 2016). Additionally, the variation in the band gap energy of capped and uncapped is due to different synthesis method which can introduce different types and levels of defects, such as oxygen vacancies, which in turn affect the band gap (Furka *et al*., 2025).

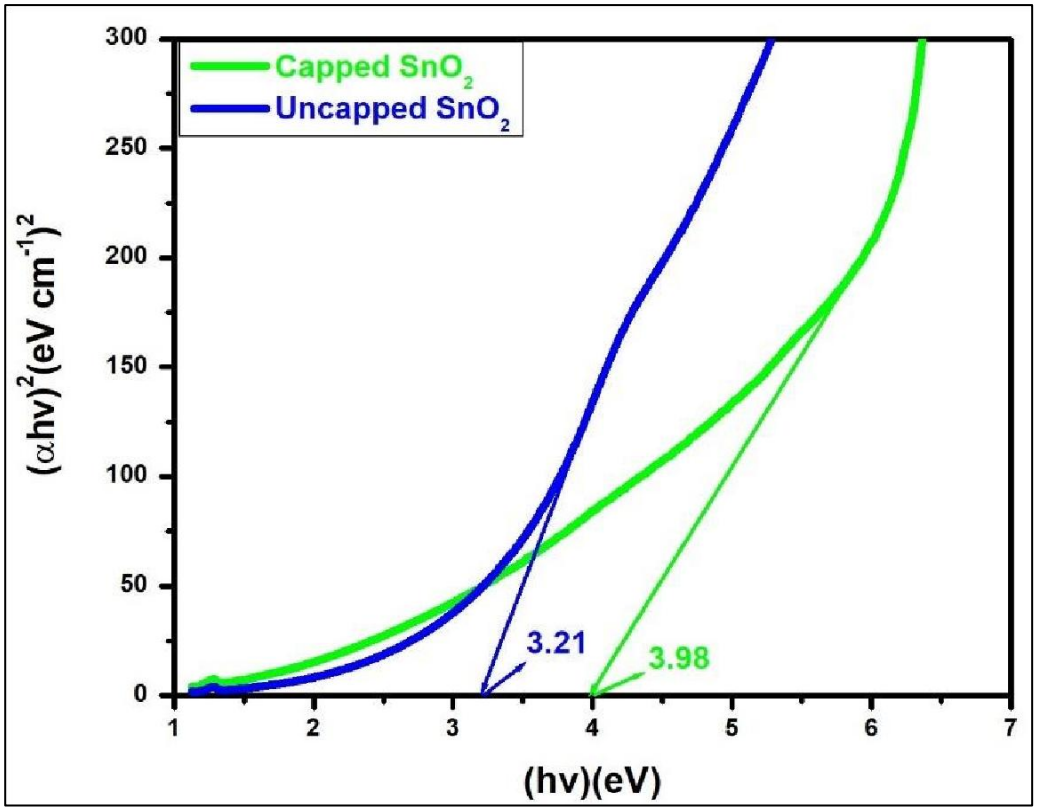


Figure 4.2: Tauc's plot extrapolation of capped and uncapped SnO_2

4.2.2 XRD analysis of undoped tin oxide nanoparticles

Figure 4.3 displays XRD pattern at specific 2 θ values at 26.55, 34.04, 38.15 51.99, 54.96, 57.98, 61.59, 65.83 and 71.28 for capped SnO_2 and 26.55, 34.03, 38.73, 51.91, 54.96, 57.98, 61.59, 65.48 and 71.28 for uncapped SnO_2 along the miller indices of 110, 101, 200, 211, 220, 002, 310, 301, 202 and 321. Additional peak was observed at 46 ° and was more intense in uncapped than for the capped SnO_2 nanoparticles. The obtained XRD pattern indicates that the synthesized NPs possess a rutile structure with tetragonal unit cell and was further confirmed by the Joint Committee on Powder Diffraction Standards (JCPDS) card 00-41-1445. The crystallite size was calculated using Debye Scherrer equation (Equation 3.3) (Kiprotich *et al*., 2018). Crystallite size was calculated from the average of four peaks (101), (200), (211) and (301). From Scherrer equation, average crystallite size showed that capped SnO_2 had smallest crystallite size of 14.89 nm but for uncapped SnO_2 the crystallite size of nanoparticle increased to 18.00 nm (Table 4.1).

The behaviour is due to the ability of the capping agents being absorbed onto SnO_2 surface and so prevent the diffusion of growth species. Smaller crystallite size for capped NPs compared to uncapped has been reported when ZnO was capped with *citrus reticulata* peel extract (Jepngetich *et al.*, 2025) and also when Fe_2O_3 was prepared using different amount of capping agents (Sagadevan *et al.*, 2017). The difference in the crystallite size between capped and uncapped SnO_2 NPs illustrate that *P. guajava* extract has impact in the particle formation during nanoparticles synthesis. Also, the crystallite size is also affected by strain where Crystal size $\alpha \frac{1}{Strain}$ (Siyalo *et al.*, 2025). At miller indices (110), (101), (211), capped SnO_2 has a high intensity peak compared to uncapped SnO_2. Therefore, this shows that nanoparticles prepared with capping agents had high crystallinity.

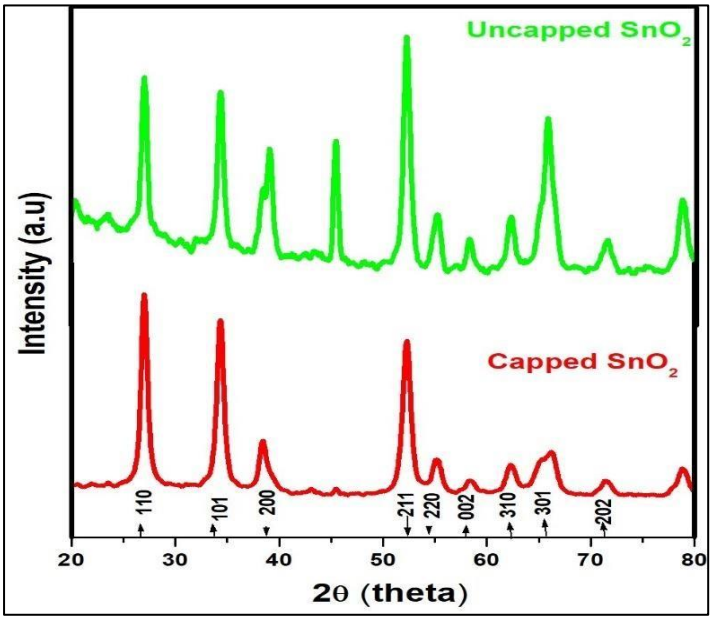


Figure 4.3: XRD pattern of SnO_2 synthesized with and without *P. guajava* extract

The dislocation density (δ), defined as the length of dislocation-lines per unit volume of the crystal was calculated using Equation 4.1 (Bett *et al.*, 2024) as Table 4.1 shows the results.

$$(\delta) = \frac{1}{D2} \qquad (4.1)$$

Where δ is the dislocation density and D is the crystallite size, λ is the X-Ray wavelength and θ is the Bragg's diffraction angle. Table 4.1 also shows the micro-strain ($\in$) values, which were computed using the Equation 4.2 (Bett *et al.,* 2024).

$$\in = \frac{\beta}{4 \tan\theta} \qquad (4.2)$$

Where θ is the diffraction angle and β is the full width at half maximum. From Table 4.1, it is observed that crystallite size is inversely proportional to FWHM. For capped SnO_2, the average strain value ($\in$) of 0.0065 is higher than for uncapped SnO_2 with 0.0053, hence capped SnO_2 have a small size than uncapped SnO_2. The organic molecules from the capping agent interacts with the surface atoms, causing slight lattice distortions that lead to increased strain.

Table 4.1: FWHM, crystallite size (d), d-spacing, dislocation density(δ) and micro-strain of undoped SnO_2 nanoparticles

Nanoparticles	**Plane**	**110**	**101**	**200**	**211**	**301**
Capped SnO_2	FWHM	0.5875	0.6045	0.6162	0.7298	0.4726
	2θ	26.72	34.04	38.16	51.98	65.83
	D (nm)	13.66	13.74	13.64	12.11	20.02
	δ	0.0054	0.0053	0.0054	0.0068	0.0025
	$\in$	0.0108	0.0086	0.0078	0.0033	0.0031
	D	0.3334	0.2632	0.2356	0.1757	0.1417
Uncapped SnO_2	FWHM	0.4985	0.5317	0.3521	0.6089	0.5257
	2θ	26.72	34.03	38.73	51.91	65.48
	D (nm)	16.38	15.62	23.91	14.51	17.97
	δ	0.0037	0.0041	0.0017	0.0047	0.0031
	$\in$	0.0092	0.0076	0.0044	0.0055	0.0036
	D	0.3238	0.2632	0.2323	0.1760	0.1417

4.2.3 Photoluminescence spectroscopy analysis of undoped nanoparticles

The PL study is performed to determine the ability of the material to absorb photon energy and emit due to the oxygen vacancies, charge recombination and migration efficiency of the synthesized NPs. Figure 4.4 depicts photoluminescence spectra of synthesized SnO_2 NPs with and without *P. guajava* extract with 250-500 nm range. The analysis was done at room temperature with an excitation wavelength of 260 nm. Tin oxide has been reported to have varying absorption wavelength at 275 nm (Ahmed *et al*., 2011), 300 nm (Suthakaran *et al*., 2020), and 325 nm (Nagirnyak *et al*., 2016).

Excitation peak at 264 nm was observed for *P. guajava* capped and uncapped SnO_2 NPs with uncapped SnO_2 having higher peak intensity than capped SnO_2 NPs. The PL spectra showed two types of emissions: near band edge emission (NBE) in UV region and defect level emission (DLE) in the visible region. Three emission peaks are observed at 354.62, 378.74 and 468.21 nm for uncapped and 468.21 capped SnO_2. The peaks around near UV region (354.62 and 378.74 nm) for uncapped sample belong to near band edge emission (NBE) which is formed due to the recombination of electrons in the conduction band and holes in the valence band (Ahmed *et al*., 2011) leading to the formation of positively charged holes and negatively charged electrons. The presence of free charge carriers influences the intensity of the photoluminescence peak (Ran *et al*., 2015).

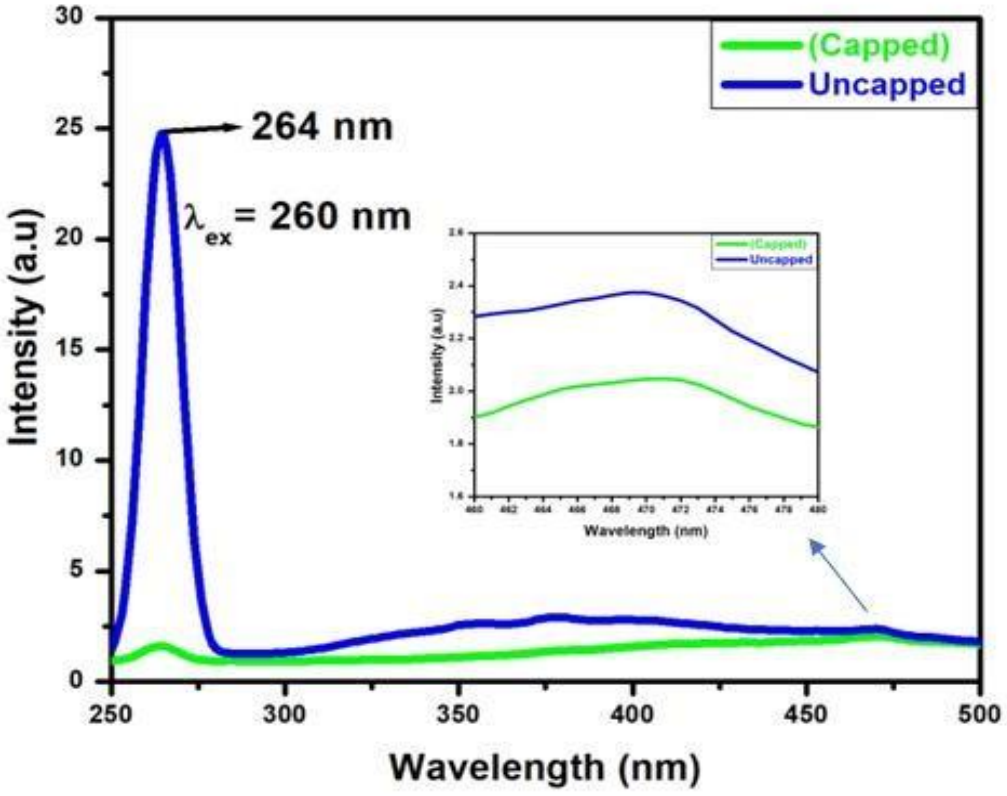


Figure 4.4: PL spectra of SnO_2 NPs with and without p. guajava extract

Oxygen vacancy and interstitials of the material are the most common defects found in metal oxide. As intrinsic defects, the oxygen vacancies have the ability to capture electrons and function as ionized vacancies. The ionized vacancies act as defect donors and form new energy levels and they also have an impact in optical properties of the SnO_2 photocatalyst. In SnO_2, oxygen vacancies are present in three different charge states: V^o, V^{+1} and V^{+2}, in which V^0 is very weak shallow donor (Ahmed *et al*., 2011). From the inset in Figure 4.4, the peak at 468.21 nm belong to Deep Level Emission (DLE) which is attributed to the impurities and structural defects in the synthesized NPs (Baraneedharan *et al*., 2015). These defects act as luminescent centers (M *et al*., 2017). Emission in the DLE was also reported (Suthakaran *et al*., 2020). Compared to uncapped SnO_2 NPs, capped SnO_2 NPs have a lower emission intensity. The lowering of the emission intensity indicates an inhibition of electron - hole recombination, which leads to increase the higher photocatalytic activity

(Suthakaran *et al*., 2019). With low defect, more free charge carriers will be available, so it can absorb more radiation than others, it leads to better performance in the photocatalytic material. Holes are generated from Sn vacancies (V_{Sn}) and O interstitials (O_i), V_{Sn} believed to be the main source of hole carriers because it is difficult to ionize O_i totally (Nguyen *et al*., 2017).

4.2.4 The FTIR analysis of undoped nanoparticles

Capped and uncapped SnO_2 samples were characterized by FTIR spectroscopy Shimadzu model with 32 number of scans in order to identify the chemical bonding and functional group present. Figure 4.5 shows the FT-IR spectra of plant extract capped and uncapped SnO_2 recorded in the range of 400-4000 cm^{-1}. The main bands were observed in both fingerprint and functional groups region for capped SnO_2 but uncapped SnO_2 showed a peak only in the finger print region. The peak observed at 3652.77 cm^{-1} is due to the stretching vibration of O-H bond and N H of the fatty acids, carbohydrates, and lignin units contained in the leaf of *Psidium guajava* (Zayed *et al*., 2022). The peak is in the range previously reported by Adnan *et al*., 2010 and Mahfooz *et al.*, 2019 and the peak is due to OH groups and the adsorbed water bound at the SnO_2 surface.

The O-H peak was more intense in the capped SnO_2 indicating that hydroxyl groups present, are likely due to the interaction between the guava phytochemicals and the tin oxide surface. The peak at 2973.55 cm^{-1} is due to the C-H stretching which is associated with aliphatic organic compounds from the guava leaves and it is more intense than other peaks in the spectra. The peak around 1379.06 cm^{-1} represents the stretching vibrations of C=O. The carbonyl group could be a part of the fatty acids in the extract. Presence of C≡C was observed at 2158.37 cm^{-1} while at 749.23 and 746.44 cm^{-1} corresponds to Sn-O for capped and uncapped SnO_2 respectively which confirms the formation of metal oxide (Saha *et al.*, 2021). The peak at 1155.29 cm^{-1} corresponds to C-O stretching from phenols. The set of peaks in the range of 1550 to 890 cm^{-1} is due to the vibration of hydroxyl tin bonds (Haq *et al.*, 2020)

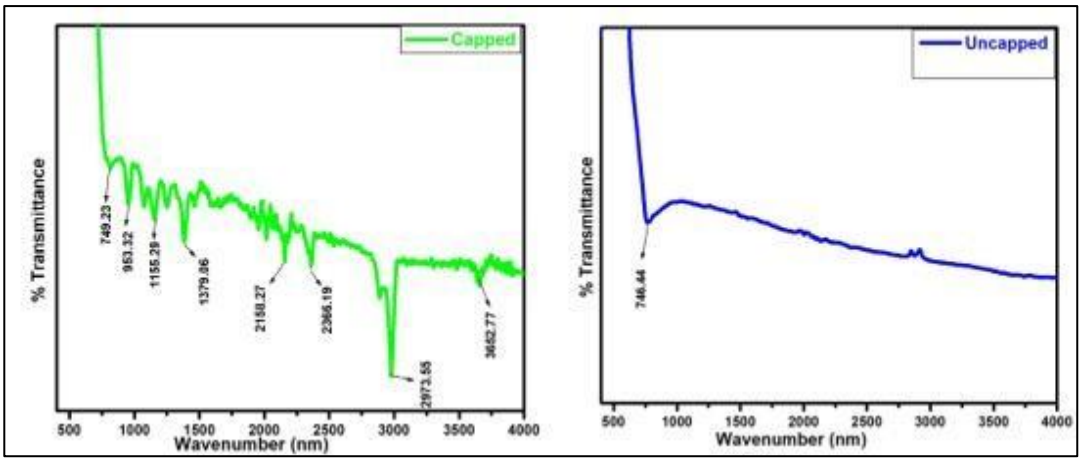


Figure 4.5: FTIR spectra of capped and uncapped SnO_2 in the range 400-4000 cm^{-1}

4.3 Optimization of Al and Ga doping concentration on the synthesis of SnO_2 NPs

4.3.1: Effect of varying Al doping concentration on the structural, luminescence and optical properties of SnO_2 NPs synthesized with and without the caping agent

This study investigates the effect of varying Al doping concentrations on the structural, optical, and luminescence properties of SnO_2 nanoparticles synthesized with and without a capping agent. Synthesized nanoparticles were analysed using UV-Vis, XRD, Pl and FTIR.

4.3.1.1 Optical analysis of doped and undoped nanoparticles

The optical properties of pure and Al doped tin oxide with and without *P. guajava* extract were monitored using UV-Spectrophotometer (Model UV-1800 SHIMADZU). The data was collected from different samples in the UV-Vis spectrophotometer, plotted using origin. The analysis was carried out at room temperature in the wavelength range 200-800 nm. Figure 4.6 depicts the absorbance spectra of pure and Al-SnO_2 nanoparticle synthesized with (a) and without (b) *P. guajava* extract. Numerous variables, notably band gap, oxygen deprivation, surface roughness and impurity centres, are expected to affect absorbance. Strong absorption edge in the region 200-300 nm was observed. Highest absorption occurred in the SnO_2 sample doped with 2.5% aluminium for capped and uncapped Al-SnO_2 respectively.

A decrease in the intensity was also noted at 1.0 % capped Al-SnO_2. Absorption occurred as a result of electron transition from one energy level to another energy level (Agrahari *et al*., 2015).

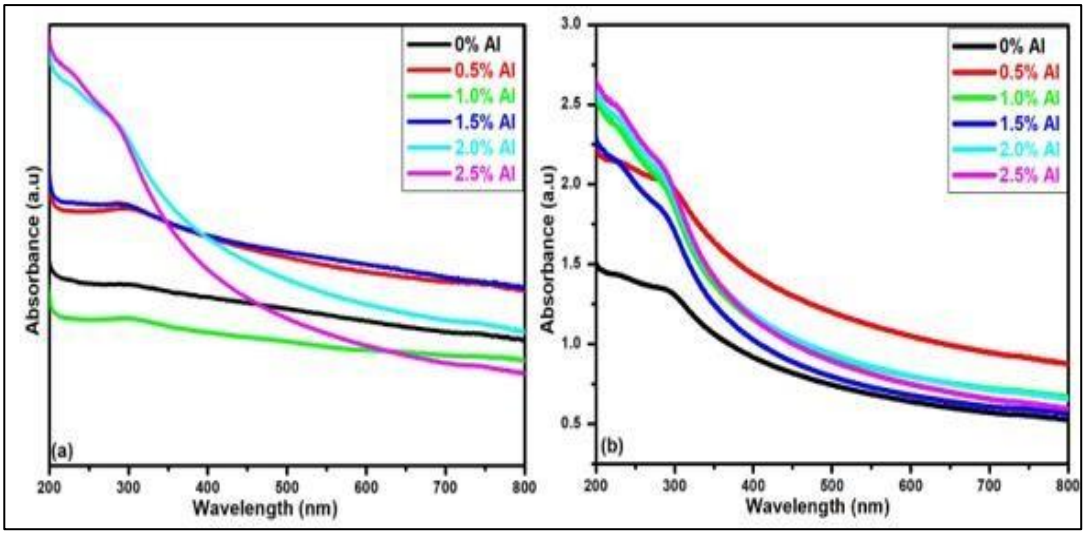


Figure 4.6: Absorbance spectra of synthesized SnO_2 and Al doped SnO_2 with (a) and without (b) *P. guajava* extract

The optical band gap of pure SnO_2 and Al-SnO_2 synthesized with and without *psidium guajava* extract was determined using Tauc's method. The Tauc's plot method, is widely recognized for determining the optical band gap of semiconductors. The method involves plotting $(\alpha h\nu)^2$ against photon energy ($h\nu$) as shown in figure 4.7. This approach involves extrapolating the linear portion of the absorption edge from diffuse reflectance spectra based on the relationship between the absorption coefficient (α) and photon energy.

The resultant energy band gaps are listed in Table 4.2 for each doping concentration for both capped and uncapped Al-SnO_2. The value of energy band gap decreased when Al was introduced thus allowing more electrons to undergo electronic transition from the valency band to the conductive band (Doyan *et al.*, 2018), (Rajan *et al.*, 2017) and (Lee *et al*., 2019). Capped Al-SnO_2, has a less band gap value than uncapped Al-SnO_2. The decrease in the energy band gap value is also influenced by the presence of Al in the SnO_2 structure (Doyan *et al*., 2021). This is because Al is a good conductor of

electricity (Doyan *et al*., 2018) (Doyan *et al*., 2017). The smaller the energy band gap, the easier it is for an electron to move from the valence band to the conduction band. The introduction of acceptor state, created by trivalent Al ion substituting the tetravalent tin ions, shifts the Fermi level toward the valence band effectively narrowing the energy gap.

When the concentration of dopant is increased, it weakens the confinement effects by increasing the defects level thus a decrease in band gap (Amrute *et al*., 2024). At higher concentration, the band gap of capped Al-SnO_2 slightly increased due to the Burstein-Moss effect. At a higher concentration there is an increase in free carrier concentration occupying the lowest state of conduction band (Rauwel *et al*., 2021). Thus, shifting the Fermi level upward relative to the band edges leads to an apparent increase in the band gap (Rauwel *et al*., 2021). Doping causes a decrease in the band gap which is lower than that of the bulk (3.6 eV) due to strong quantum confinements and an increase in the surface-area-to-volume ratio (Drake *et al.*, 2007). The primary reasons for the decrease in the doped sample's band gap energy are the quantum confinement effect and a rise in the surface-area-to-volume ratio (Thamarai *et al*., 2018).

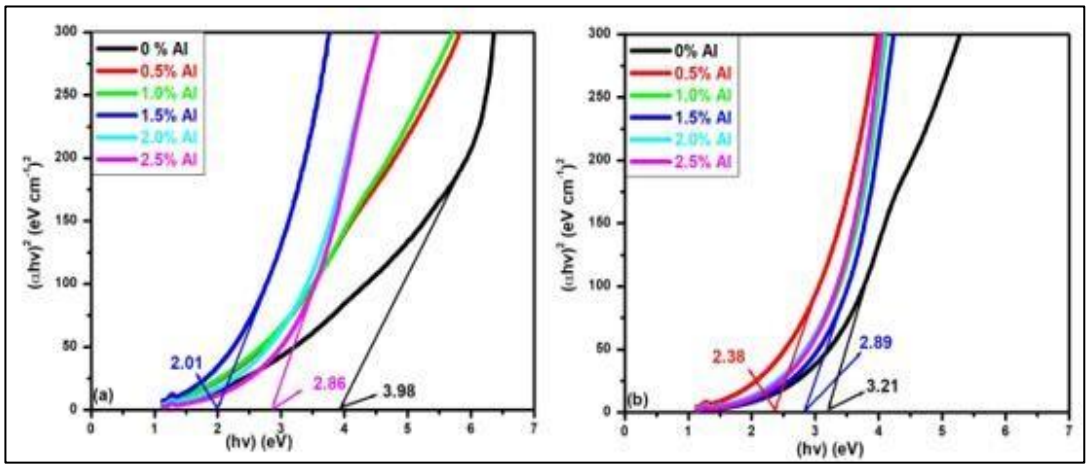


Figure 4.7: Tauc's plot estimate of SnO_2 and Al-SnO_2 synthesized with (a) and without (b) *P. guajava* extract

Table 4.2: Energy band gaps (eV) of pure SnO_2 and Al-SnO_2 synthesized with and without *P. guajava* extract

Dopant concentration	Capped Al-SnO_2	Uncapped Al-SnO_2
0% (Pure SnO_2)	3.98	3.21
0.5%	2.26	2.38
1.0%	2.40	2.52
1.5%	2.01	2.89
2.0%	2.50	2.57
2.5%	2.86	2.52

4.3.1.2 XRD analysis doped nanoparticles

Figure 4.8 depicts the XRD patter of synthesized SnO_2 and Al-SnO_2 with (a) and without (b) *p. guajava* extract recorded in the range of 20-80° using EQUINOX 100 XRD spectrometer. The spectra confirm the presence of tetragonal crystal structure in most samples for capped and uncapped Al-SnO_2. The main plane for capped and uncapped Al-SnO_2 were (110), (101), (200), (211), (220), (310), and (301) that were nearly peaked at 26.6, 34.2, 38, 50.8, 55, 61, and 63° respectively as reported previously (Benouis *et al*., 2014) (Moharrami *et al*., 2012). The structure of tin oxide in its bulk form is tetragonal rutile with lattice parameters a = 4.74 Å and c = 3.19 Å (Benouis *et al*., 2014). It is expected that Al atoms substitute Sn in the lattices or occupy Sn interstitials because the ionic radii of Al^{3+} (0.58 nm) is smaller than that of Sn^{4+} (0.71 nm).

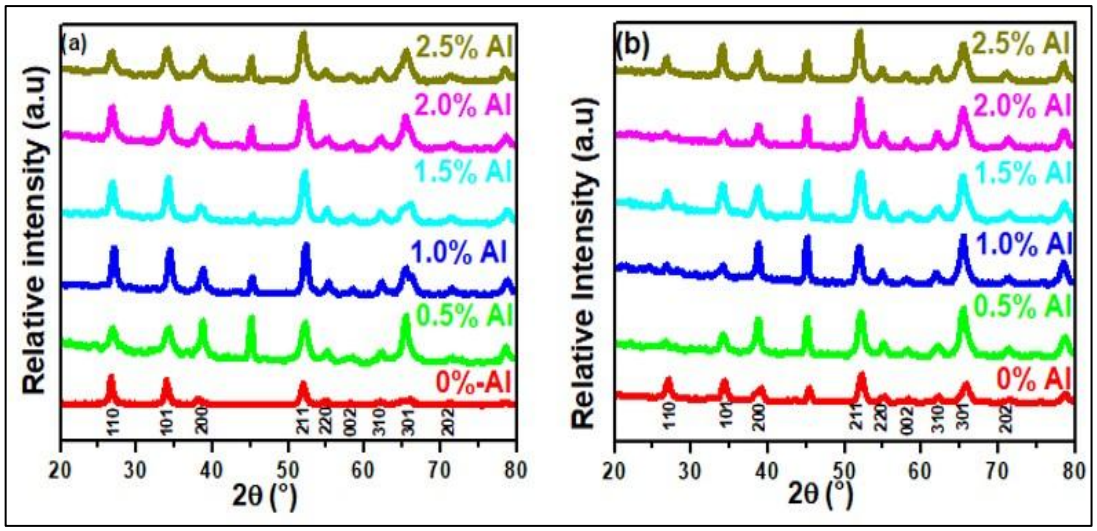


Figure 4.8: XRD pattern of synthesized SnO_2 and Al-SnO_2 with (a) and without (b) *P. guajava* extract

The crystallite size of capped and uncapped Al-SnO_2 was calculated using Scherrer equation (Equation 3.3) (Kiprotich *et al*., 2018) as shown in Table 4.3 and 4.4 respectively. For capped Al-SnO_2, 2.0 % Al-SnO_2 had the smallest size of 10.57 nm while the highest crystallite size value of 14.70 nm was observed in nanoparticles doped with 0.5%. For uncapped Al-SnO_2 (Table 4.3), 1.5 % Al-SnO_2 had the smaller size of 12.75 nm while the highest crystal size value of 15.28 nm was observed at 0.5 % Al doping, note that a similar range was and was previously reported (Chan *et al*., 2012). Decrease in crystal size has also been reported previously Doyan *et al*., 2018 and Khlayboonme *et al.*, 2021.

The reduced crystallite size was caused by lattice strain, attributed to the slight difference in ionic radius and different oxidation states. The undoped SnO_2 shows a weak intensity peaks which are effectively improved by doping causing enhanced crystallinity. Al doping causes a slight shift in the peak position compared to undoped SnO_2 implying that Al causes distortion of the lattice and occurrence of stress (Khlayboonme *et al*., 2021). Not all Al atoms used as dopant replaced Sn sites, but fewer Al atoms occupied interstitial sites and squeezed between lattices at which there were no atoms hence the distortion. Al^{3+} interstitials act as nucleation sites that can

prevent further crystal growth (Pal *et al*., 2014). A larger number of nucleation site increases the grain boundaries, reducing the crystallite size (Thanh *et al*., 2014).

Nanoparticles with smaller crystallite size have large surface area to volume ratio thus higher surface energy which caused higher strain. This leads to increase in crystallite size with decrease in strain. For both capped and uncapped Al-SnO_2, the FWHM is inversely proportion to the crystallite size causing a large crystallite size at minimum FWHM (Figure 4.9). A similar observation was observed by Jepngetich *et al*., 2025. The variation was not constant with variation in concentration. The increase in FWHM for Al-SnO_2 is attributed to asymmetrical stretching from the Al-O-Sn crystal disorder, leading to a broader peak. The substituted atoms of Sn occupy the interstitial position or other available sites in the crystal lattice to allow the crystal to adjust and maintain charge neutrality and structural stability.

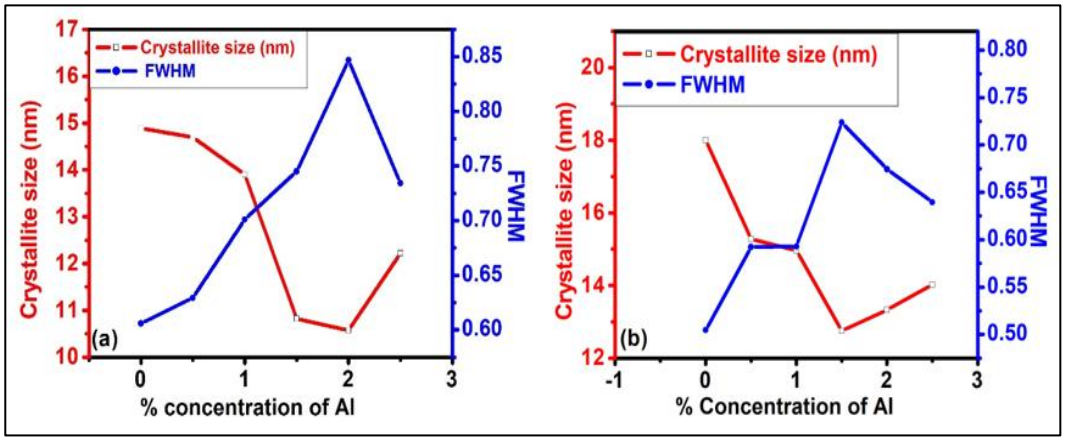


Figure 4.9: Relationship between crystallite size with FWHM of capped (a) and uncapped (b) Al-SnO_2

The dislocation density (δ), defined as the length of dislocation-lines per unit volume of the crystal was calculated using Equation 4 (Bett *et al.*, 2024)) and the results are shown in Tables 4.3 and 4.4. The dislocation network within the structure is indicated by the dislocation density and is inversely proportional to crystallite size. Figure 4.10 shows dislocation density and strain effects on the nano-crystal structure of Al doped tin oxide nanoparticles where the regular arrangement of atoms is disrupted. From Figure 4.10, it is observed that micro strain is directly proportional to dislocation

density indicating a change in size and shape of material. Additionally, higher dislocation densities and strain implies stronger nanoparticles but less ductile nanomaterials and vice versa.

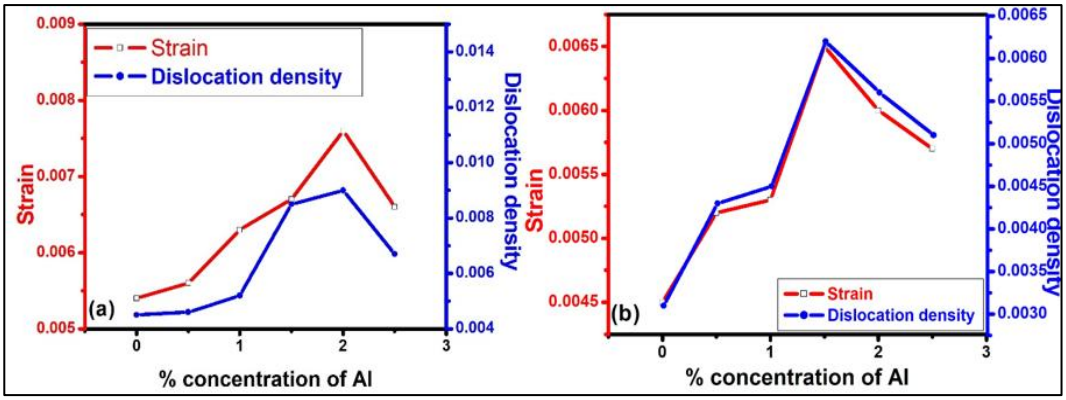


Figure 4.10: Trend of dislocation density and strain of capped (a) and uncapped (b) Al-SnO_2

Table 4.3: 2θ, full width at half maximum (FWHM), Crystallite size (D) and dislocation density (δ) for capped Al-SnO_2

		Dopant concentration					
	Plane	0%	0.5%	1.0%	1.5%	2.0%	2.5%
2θ	100	26.72	26.86	26.02	26.86	26.85	26.75
	101	34.04	34.18	34.18	34.11	34.18	34.05
	200	38.16	38.71	38.75	38.68	38.56	38.71
	211	51.99	52.14	52.05	51.99	52.09	51.96
	301	65.83	65.43	65.45	65.44	65.48	65.49
FWHM	100	0.5876	0.7770	0.0756	0.6946	0.6149	0.6826
	101	0.6046	0.7659	1.0964	0.7265	0.6340	0.6359
	200	0.6162	0.4203	0.4400	0.4923	0.9106	0.6067
	211	0.7299	0.7400	0.6523	0.8640	0.8436	0.7249
	301	0.4727	0.5910	0.6151	0.8972	0.9993	0.9694
D (av)		14.89	14.70	13.90	10.82	10.57	12.22
δ		0.0045	0.0046	0.0052	0.0085	0.0090	0.0067

Table 4.4: 2θ, full width at half maximum (FWHM), Crystallite size (D) and dislocation density (δ) for uncapped Al-SnO_2

	Plane	**Dopant concentration**					
		0%	0.5 %	1.0 %	1.5%	2.0%	2.5%
2θ	100	26.72	26.77	26.68	26.87	26.71	26.66
	101	34.03	34.09	34.20	34.13	34.22	33.99
	200	38.73	38.75	38.75	38.70	38.73	38.74
	211	51.91	52.90	52.14	52.09	52.07	51.78
	301	65.48	65.35	65.49	65.47	65.49	65.39
FWHM	100	0.4985	0.6121	0.8431	0.5876	1.0340	1.5142
	101	0.5318	0.5731	0.6046	0.6991	0.6765	0.6749
	200	0.3521	0.4201	0.4597	0.4689	0.5170	0.4708
	211	0.6089	0.6383	0.6614	0.8224	0.5599	0.7032
	301	0.5257	0.7413	0.6553	0.9043	1.0556	0.7090
D (av)		18.00	15.28	14.96	12.75	13.33	14.02
δ		0.0031	0.0043	0.0045	0.0062	0.0056	0.0051

The lattice parameters were calculated using equations 4.3 and 4.4 (Bett *et al*., 2024).

$$a=\frac{\lambda}{\sqrt{3}\sin\theta} \qquad (4.3)$$

$$c = a\sqrt{\frac{8}{3}} \qquad (4.4)$$

where ‘a’ and ‘c’ are the lattice parameters. Table 4.5 shows the lattice parameters ‘a’ and ‘c’ as well as the micro-strain (∈) values which were computed using Equation 4.2 (Waweru *et al.,* 2024). Variation of strain with crystallite size is shown in Figure 4.11. It is observed that crystallite size is inversely proportional to strain (Siyalo *et al*., 2025). The variation in the strain and lattice parameters were attributed to size variation of nanocrystals and interstitial doping (Saha *et al*., 2015). Changes in strain were also attributed to the incorporation of Al, which introduces lattice distortions and defects (Nasir *et al*., 2020). This is due to slight difference in ionic radius and different oxidation states, contributing to the reduced crystallite size. Nanoparticles with smaller crystallite size have larger surface area to volume ratio thus higher surface energy causing higher strain.

Table 4.5: Lattice parameters (a and c), and strain (∈) for capped and uncapped Al-SnO_2

Dopant concentration	Capped Al-SnO_2			Uncapped Al-SnO_2		
	A	c	∈	a	c	∈
0% (Pure SnO_2)	0.2029	0.3313	0.0054	0.2032	0.3318	0.0045
0.5%	0.2024	0.3305	0.0056	0.2006	0.3276	0.0052
1.0%	0.2027	0.3310	0.0063	0.2024	0.3305	0.0053
1.5%	0.2029	0.3313	0.0067	0.2026	0.3308	0.0065
2.0%	0.2026	0.3308	0.0076	0.2026	0.3308	0.0060
2.5%	0.2030	0.3315	0.0066	0.2037	0.3326	0.0057

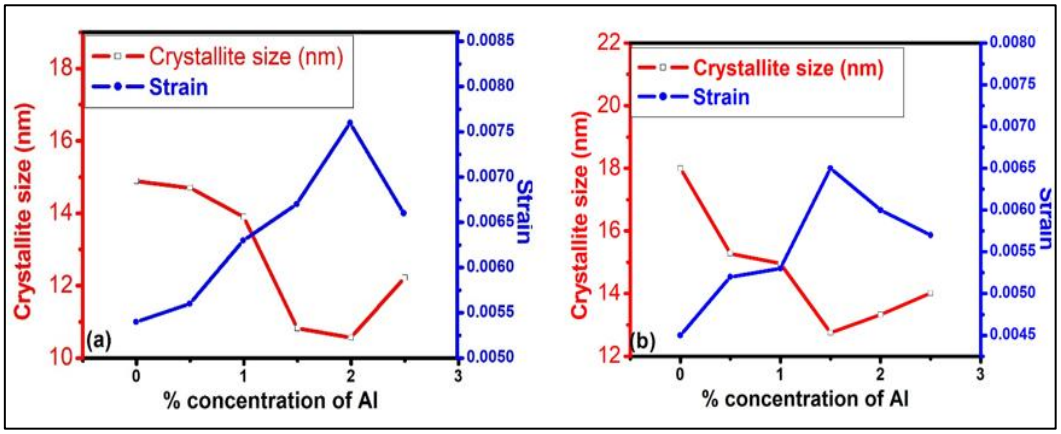


Figure 4.11: Variation in crystallite size and strain for capped (a) uncapped (b) Al-SnO_2

4.3.1.3 Photoluminescence (PL) analysis of doped nanoparticles

PL analysis aimed to assess the influence of Al doping concentration on the deep level emission and band edge emission of SnO_2 synthesized with and without *psidium guajava* extract. Figure 4.12 and 4.13 depicts photoluminescence spectra of synthesized pure SnO_2 and Al-SnO_2 with and without *P. guajava* extract at an excitation wavelength of 260 nm in the range 250-500 nm. The samples were analysed at room temperature and results plotted using Origin software. The absorption of

energy or light that causes electron excitation is referred to as the excitation spectrum. Excitation spectra had a peak centered at 264 nm for undoped SnO_2 and Al-doped SnO_2. This absorption peak indicates that photons with a wavelength of 260 nm is absorbed by the material, creating an exited state due to electronic transition from the valency band to conduction band. From Figure 4.12, doping rate of 1.5% and 2.5% Al-SnO_2 NPs had the highest and lowest excitation intensity respectively. From Figure 4.13, it is observed that pure SnO_2 and 2.5% Al-SnO_2 had the highest and lowest excitation intensity respectively.

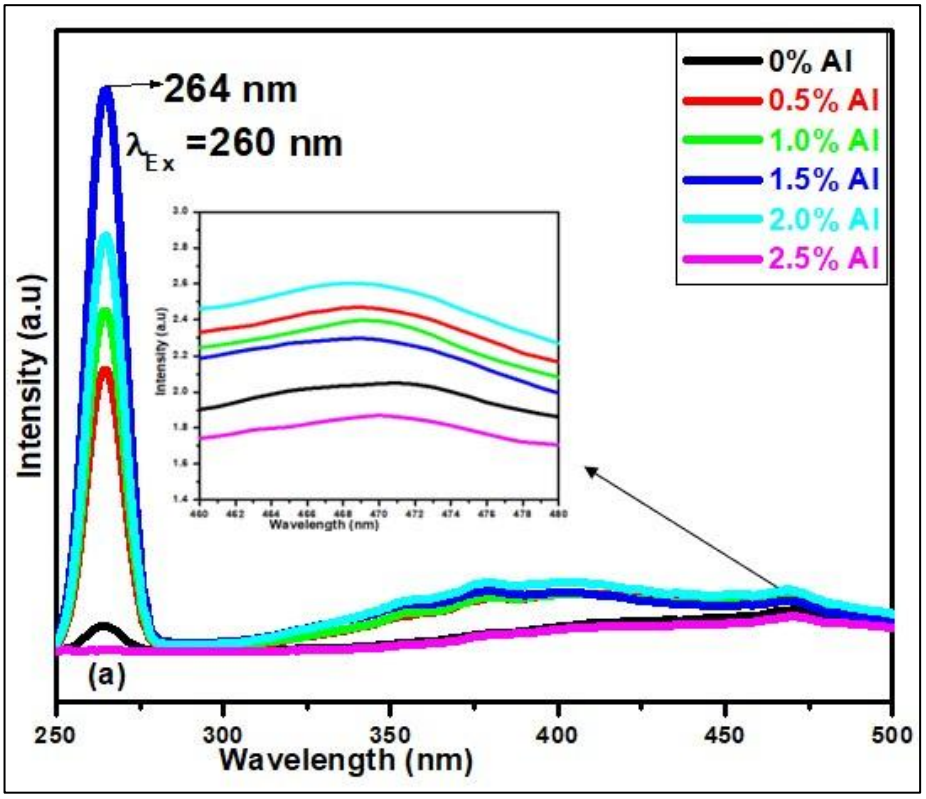


Figure 4.12: Photoluminescence spectra of pure SnO_2 and Al- SnO_2 synthesized with *P. guajava* extract in the range 250-500 nm

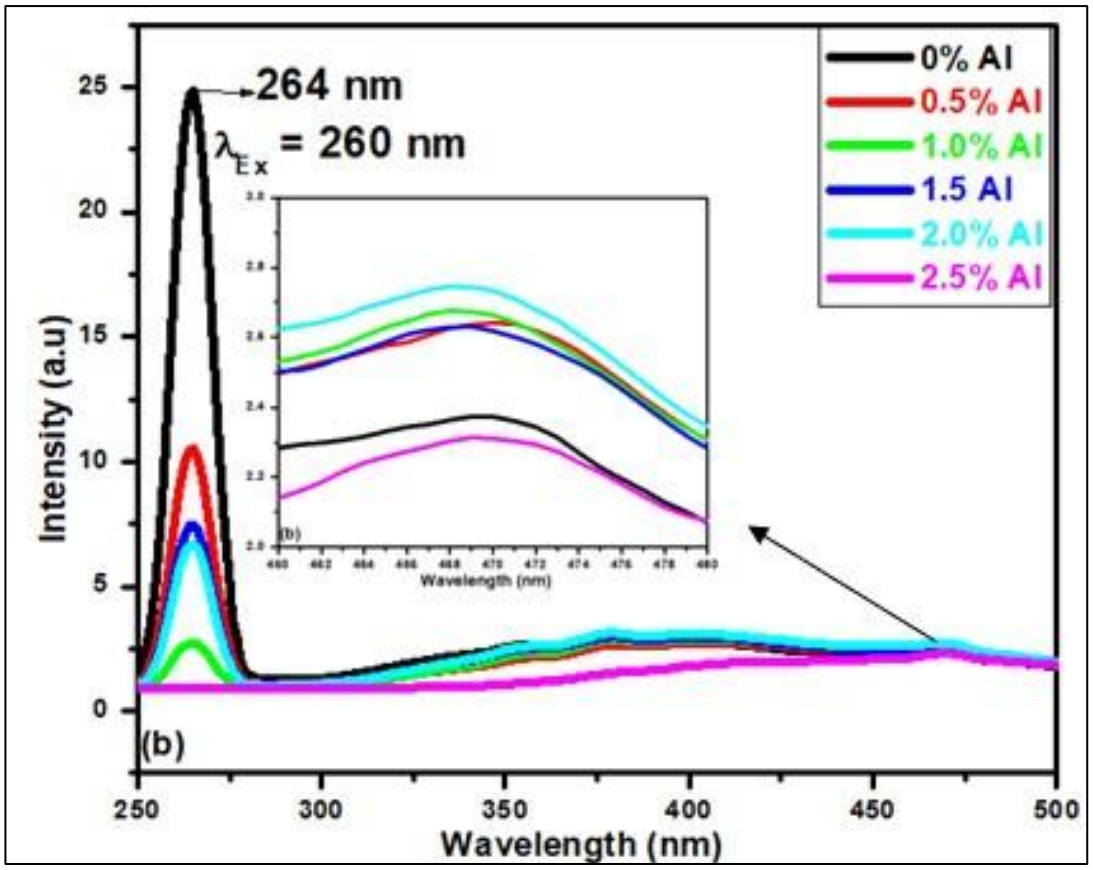


Figure 4.13: Photoluminescence spectra of pure SnO_2 and Al- SnO_2 synthesized without *P. guajava* extract in the range 250-500 nm

The energy released as electrons return to their ground state from excited states is represented by the emission spectrum. The near band edge (NBE) is responsible for the UV region's peaks centred (354.62 and 378.74 nm), which correspond to band-to-band transitions and are caused by exciton-exciton collisions process (Sarangi *et al*., 2018). This is attributed to photo-carrier recombination in the NBE and the direct recombination of a conduction electron in the Sn "4p" and a hole in the O "2p" valence band (Sabri *et al.*, 2012) (Samavati *et al*., 2017). For both capped and uncapped Al-SnO_2, the broad peak at 460–480 nm is likely due to impurities, localized states, or defects in the SnO_2 or Al-doped SnO_2. The interaction of Sn with oxygen vacancies is responsible for the appearance of the strong emission peak at 468.21 nm as suggested previously (Cheng *et al*., 2008) or defects which forms deep level emission. Strong emission at room temperature may arise from these interactions as a result of the creation of trapped states and a number of metastable energy levels within the

energy gap (Cheng *et al*., 2008). In UV region high intensity peaks are observed, while in visible region low intensity peaks are present.

Table 4.6 shows peak centre and intensity of Al-SnO_2 synthesized with and without the *Psidium guajava* extract obtained using origin software. The maximum peak intensity for both capped and uncapped NPs was 2.0 % Al-SnO_2, which increased by 0.36 and 0.58 from pure SnO_2, respectively. For capped and uncapped NPs, 2.5% Al-SnO_2 showed a decrease in the intensity with a decrement of 0.07 and 0.20 from pure SnO_2, respectively. A lower PL intensity results from fewer oxygen vacancies, which implies fewer recombination centres.

The enhanced intensity is due to the defect as Al doping introduces new energy levels within the band gap of SnO_2 and also introduction of free charge carrier (electrons). Increase in intensity for Al doping has also been reported by Benouis and coworkers (Benouis *et al*., 2014). Similar red-shift has been observed in the dominant PL peak for other oxide spectra. For example, SnO_2 on doping with Mn (Sabri *et al.,* 2012) and ZnO on doping with Ag (Hosseini *et al*., 2015). Better material quality is indicated by higher peak intensity, which denotes fewer defects. The presence of Al modifies the band structure of SnO_2 by introducing additional electronic states, which can enhance luminescence.

The origin of visible emission can be assigned to the recombination of electrons in the shallow levels with the photo excited holes in valence band. In the case of doped samples, it is easy for Al^{3+} ions to substitute Sn^{4+} ions because the ionic radius of Al^{3+} and Sn^{4+} are almost equal. As mentioned in literature, if the Sn tetravalent ions were substituted by Al trivalent ions, one broken bond (hole) is produced, which acts as an acceptor energy level near the valence band and accepts an electron from it, thus increasing the hole concentration (Benouis *et al.*, 2014). The vacancy thus created give rise to defect levels in the crystal and hence enhances the visible emission. In SnO_2, oxygen vacancies are present in three different charge states: V^0, V^{+1} and V^{+2}, in which V^0 is a very shallow donor (Ahmed *et al.,* 2011). Better performance in photocatalytic materials results from less defects since there are more free charge

carriers accessible, allowing it to absorb more radiation than others. The Al^{+3} ions can go to the interstitial sites as donors and might occupy Sn^{+4} sites as acceptors.

Table 4.6: Photoluminescence Intensity and peak centre of Al-SnO_2

Dopant concentration	Capped Al-SnO_2		Uncapped Al-SnO_2	
	Peak centre	Intensity	Peak centre	Intensity
0% (Pure SnO_2)	468.74	2.36	466.06	2.02
0.5%	466.75	2.60	466.38	2.46
1.0%	466.42	2.63	466.27	2.38
1.5%	466.05	2.59	465.21	2.26
2.0%	466.12	2.72	465.65	2.60
2.5%	468.05	2.29	465.64	1.82

4.3.1.4 FTIR analysis of doped nanoparticles

FTIR Spectroscopy was used to identify the chemical bonding and functional groups in both capped and uncapped Al-SnO_2. Figure 4.14 shows the FTIR spectra in the range 400-4000 cm^1 for capped (a) and uncapped (b) NPs. The observed change in the peak position and intensity with doping reflect a change in material structure. The replacement of Sn with Al in SnO_2 caused peak widening and a little shift, due to small ionic radius of Al causing lattice deformation and distortion. In exception of uncapped SnO_2, all samples displayed a peak around 2900 cm^{-1} attributed to the O-H stretching vibration, the peak is due to OH groups and the adsorbed water bound at the SnO_2 surface as was previously reported (Adnan *et al*., 2010). The peaks observed around 952.45 and 956.87 cm^{-1} were due to the weak Sn–O bending, (Rajan *et al*., 2017). In the present case, the presence of peaks around 1379.57 cm^{-1} and 1386.99 cm^{-1} is due to Al–O bond vibrations, which provides the experimental evidence for Al substitution (Rajan *et al.*, 2017).

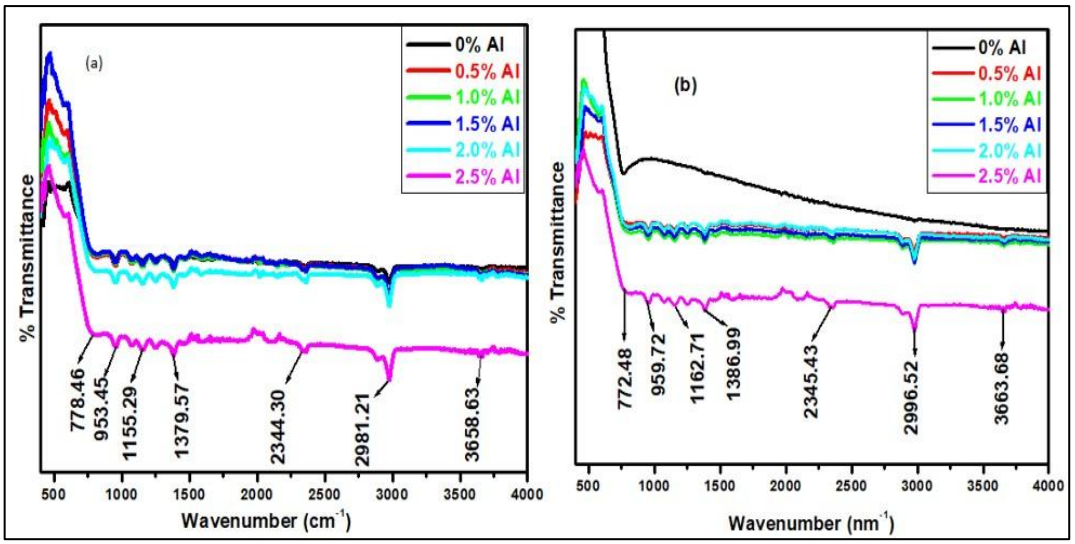


Figure 4.14: FTIR spectra of capped (a) and uncapped (b) Al-SnO_2

4.3.2 Effect of Ga doping concentration on the structural, luminescence and optical properties of SnO_2 NPs synthesized with and without *P. guajava* extract

This study investigates the effect of varying Ga doping concentrations on the structural, optical, and luminescence properties of SnO_2 nanoparticles synthesized with and without *psidium guajava* extract. Synthesized nanoparticles were analyzed using UV-Vis, XRD, PL and FTIR.

4.3.2.1 UV-Vis analysis of doped nanoparticles

Figure 4.15 shows the absorption spectra of synthesized SnO_2 and Ga-SnO_2 with (a) and without (b) *P. guajava* extract at different mol % of gallium. The absorption is related to the band gap of the material (Saha *et al.*, 2015). The highest and the lowest intensity was observed at 2.0 % and 0.5 % Ga-SnO_2 respectively for the capped NPs while for the uncapped NPs, the highest and the lowest intensity was observed at 2.0% Ga-SnO_2 and pure SnO_2 respectively. Ga doping alters the density of states in the conduction and valence bands as gallium introduces new energy states or altered pre-existing energy levels (Siyalo *et al*., 2025). Additionally, by modifying defect states, Ga doping can reduce recombination losses, improving charge separation and transport which is a critical factor for the efficiency of solar cells (Siyalo *et al*., 2025).

The absorption edge of different samples varies as the concentration of Ga in the SnO_2 nanoparticles varies.

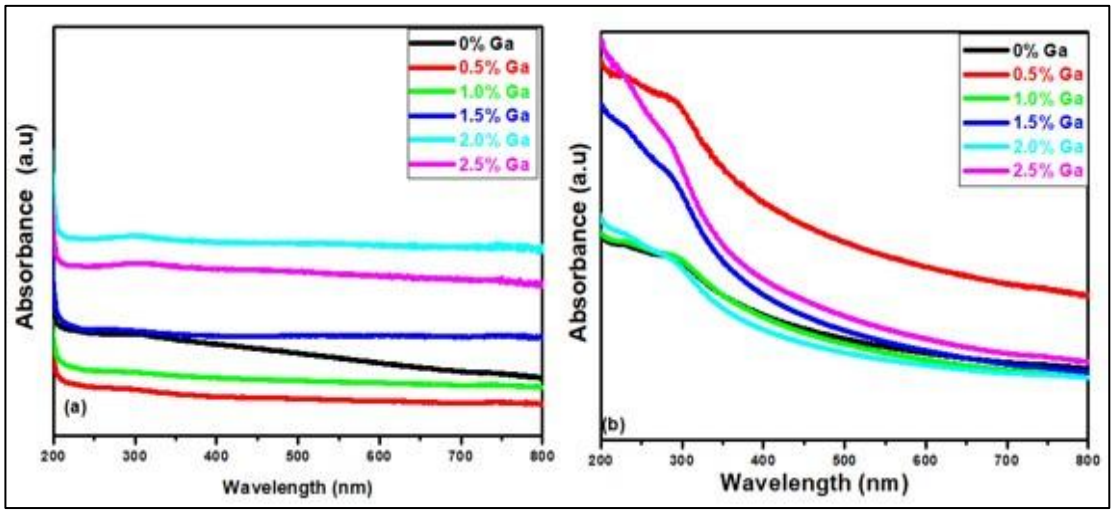


Figure 4.15: Absorption spectra of synthesized pure SnO_2 and Ga-SnO_2 with (a) and without (b) *P. guajava* extract

Figure 4.16 shows Tauc's plot for capped (a) and uncapped (b) Ga-SnO_2 at different mol concentration. Tauc's relation was used in the analysis to determine the optical band gap energy (Equation 3.1). The band gap energy is calculated as the x-intercept by extrapolating each curve's linear section (the rising edge) to the x-axis. The results are listed in Table 4.7. This process identifies the photon energy at which electronic transitions occur from the valence band to the conduction band.

For capped Ga-SnO_2 NPs, the band gap decreases from 3.25 eV to 2.29 eV with 2.5 % Ga-SnO_2 having a highest band gap and 0.5 % Ga-SnO_2 having the smallest band gap. For uncapped Ga-SnO_2, the band gap decreases with 2.0 % and 0.5 % Ga-SnO_2 having the highest and smallest band gap respectively. Decrease in band gap was also reported (Seid *et al*., 2021) for Ga doped ZnO. Additional energy level is introduced within the bandgap by Ga atom, these energy levels most likely result from structural flaws or doping-induced modifications to the electronic density of states (Siyalo *et al.,* 2025). Under visible or near-ultraviolet light, the newly added energy levels might act as intermediate states, promote multi-photon absorption and ultimately increase

photocatalysis efficiency. The decrease in band gap with addition of dopants is due to the shrinkage effect which occurs due to the induced shift of the minimum conduction band and maximum valence band (Shanmuga *et al*., 2017). Even though, the crystallite size and the band gaps expected to be changed oppositely, explanations for such a condition also be given as the quantum size effect which can cause to the shrinkage of the band gaps (Papadimitriou *et al*., 2016), (Samavati *et al.*, 2017). The band gap decreases indicating the substitutional incorporation of Ga^{3+} into the SnO_2 lattice introduces donor states therefore reducing the optical band gap. The number of electron-hole pairs increases with a smaller band gap energy. Ga doping highlights SnO_2 potential for tailoring its electronic and optical properties for specific application, such as solar cell. A decrease in the band gap signifies a shift in absorption, which reflects modifications in the electronic structure of the material, providing a means to engineer SnO_2 materials with desired optical characteristics.

Table 4.7: Energy band gap (eV) of pure SnO_2 and Ga-SnO_2 synthesized with and without *P. guajava* extract

Dopant concentration	**Capped**	**Uncapped**
Pure SnO_2	3.98	3.21
0.5%	2.29	2.46
1.0%	2.79	2.78
1.5%	3.19	3.0
2.0%	3.17	3.07
2.5%	3.25	2.90

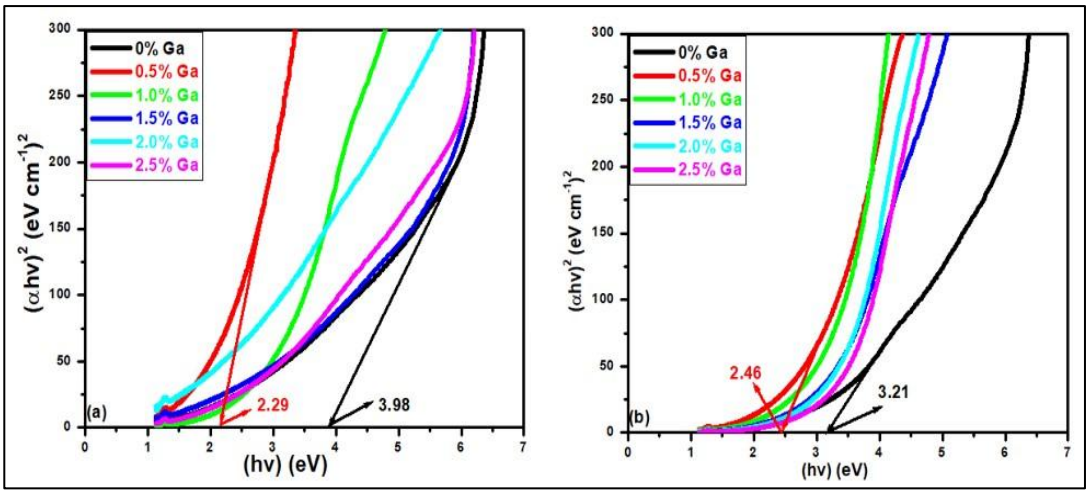


Figure 4.16: Tauc's plot estimate of synthesized SnO_2 and Ga-SnO_2 with (a) and without (b) *P. guajava* extract

4.3.2.2: XRD analysis of doped nanoparticles

The structural properties of synthesized pure SnO_2 and Ga-SnO_2 NPs were investigated using the XRD diffractometer model EQUINOX 100. Figure 4.17 depicts the XRD diffraction pattern of synthesized SnO_2 and Ga-SnO_2 NPs capped (a) and uncapped (b) at varying mol % of Ga (0.5, 1.0, 1.5, 2.0 and 2.5 %) in 2 θ from 20°-80°. The 2 θ value corresponds to the reflection from miller index 110, 101, 200, 211, 220, 002, 310, 301, 202 and 321 which agrees with JCPDS card no 41-1445.Uncapped SnO_2 and introduction of Ga shows a growth of a peak at 46°

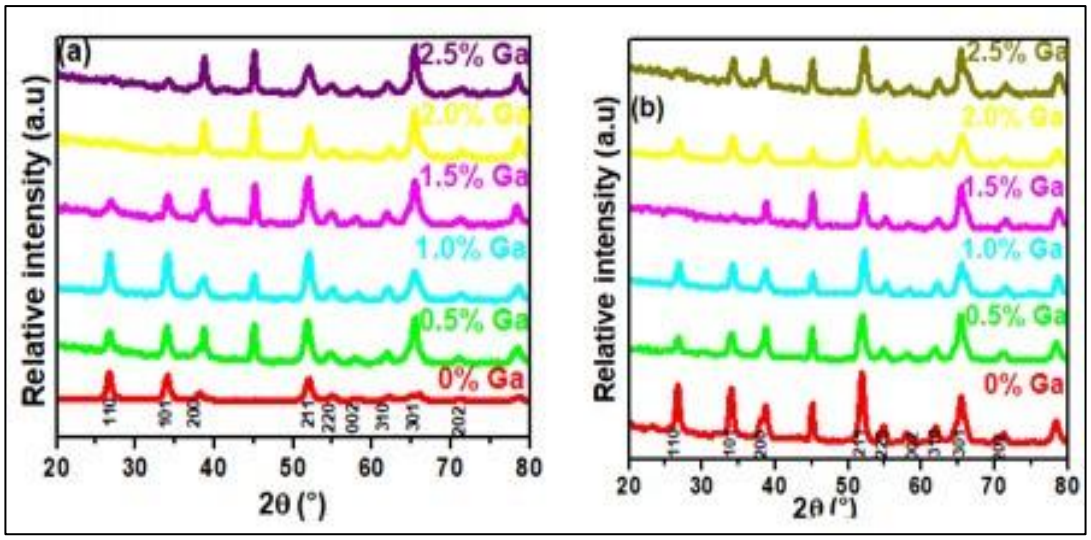


Figure 4.17: XRD pattern of synthesized SnO_2 and Ga-SnO_2 with (a) and without (b) *P. guajava* extract in the range 20°-80°

The crystallite size of capped and uncapped Ga-SnO_2 was calculated using Scherrer equation (Equation 3.3) (Jepngetich *et al.*, 2025). For uncapped Ga-SnO_2, 2.0 % Ga-SnO_2 had the smaller size of 10.99 nm while the highest crystallite size value of 15.23 nm was observed at 2.5 %. For capped Ga-SnO_2, 1.5% Ga-SnO_2 has a smaller size of 11.46 and a higher crystallite value of 16.27 nm at 0.5% Ga-SnO_2. The decrease in crystalline size when Ga was doped into SnO_2 indicates that introducing Ga atoms disrupts the natural crystal growth as Ga introduces foreign atoms in SnO_2 (Siyalo *et al*., 2025). Since ionic radius of Ga^{3+} is smaller than that of Sn^{4+}, their substitution or incorporation into the SnO_2 structure creates lattice strain or distortion which inhibits the growth of the crystalline domains, leading to smaller crystallite sizes (Kafashan *et al*., 2024). As previously reported, Ga doping results in a reduction in crystallite size (Siyalo *et al*., 2025) (Shinde *et al*., 2012).

The 2 θ values represent the diffraction angles in X-ray diffraction (XRD) analysis. Slight shifts in these values indicate changes in the lattice parameters due to doping. For example, addition of Ga to metal oxide caused lattice distortions, leading to shifts in the 2 θ values (Siddiqui *et al.*, 2018). The dislocation density (δ), defined as the length of dislocation-lines per unit volume of the crystal was calculated using

Equation 4.1 (Waweru *et al*., 2024) as shown in Table 4.8. Dislocation network within the structure is indicated by the dislocation density and is inversely proportional to crystallite size. For capped Ga-SnO_2 the δ value was highest at 1.5 % with 0.0076 and least at 0.5 % with 0.0038. For uncapped sample, the δ value was high at 2.0 % with 0.0075 and least at 2.5 % with 0.0052. Uncapped and Capped Ga-SnO_2 indicated an inverse relationship between the δ and crystallite size. A shift in crystal structure indicates a change in the interplanar spacing (d) (Siddiqui *et al.,* 2018). Figure 4.18 shows that micro strain and dislocation density are directly proportional, indicating a change and in size and shape of material. Stronger nanoparticles with higher dislocation densities and strains have fewer ductile nanomaterials, whereas weaker nanoparticles with lower dislocation densities and strains have more ductile materials.

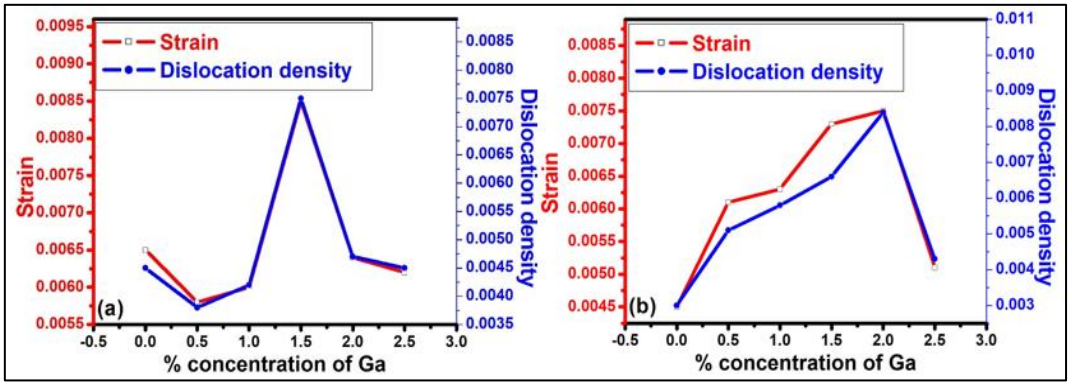


Figure 4.18: Trend of micro strain and dislocation density of capped (a) and uncapped (b) Ga-SnO_2

Table 4.8: 2θ, full width at half maximum (FWHM), crystallite size (D) and the dislocation density (δ) for uncapped (a) and capped (b) Ga-SnO_2

Materials		Plane	Dopant concentration					
			0%	0.5%	1.0%	1.5%	2.0%	2.5%
Uncapped NPs	2θ	100	26.72	26.76	26.65	26.86	26.82	26.75
		101	34.02	34.02	34.03	34.32	34.18	34.34
		200	38.73	38.34	38.75	38.79	38.68	38.73
		211	51.91	51.91	51.91	52.15	52.12	52.29
		301	65.48	65.41	66.38	65.52	65.55	65.52
	FWHM	100	0.4985	0.4842	0.9820	0.9674	0.6848	0.9306
		101	0.5318	0.6708	0.5754	1.2718	0.6567	0.5872
		200	0.3521	0.5199	0.5282	0.4585	0.7122	0.4699
		211	0.6089	0.7575	0.7184	0.6447	0.7460	0.6572
		301	0.5257	0.7767	0.9741	0.9415	1.2353	0.6144
	D (av)		18.00	13.10	13.09	12.17	10.99	15.23
	δ		0.0031	0.0052	0.0052	0.0068	0.0083	0.0043
Capped NPs	2θ	100	26.72	26.73	26.90	26.78	26.86	26.70
		101	34.04	34.02	34.06	34.09	34.13	33.98
		200	38.16	38.73	38.72	38.57	38.67	38.71
		211	51.91	51.85	51.95	52.03	52.04	51.85
		301	65.48	65.44	65.42	65.44	65.45	65.43
	FWHM	100	0.5876	0.5985	0.9542	0.5563	0.9454	0.5800
		101	0.6046	0.5329	0.5864	0.5546	0.4308	0.5908
		200	0.6162	0.4653	0.4470	1.0602	0.5217	0.4806
		211	0.7299	0.6725	0.5777	0.6850	0.6094	0.6485
		301	0.4727	0.5177	0.7260	0.9419	1.0307	0.6745
	D (av)		14.89	16.27	15.33	11.46	14.77	14.80
	δ		0.0045	0.0038	0.0043	0.0076	0.0046	0.0046

For both capped and uncapped Ga-SnO_2, high intense peaks were observed at (101), (200), (211) and (301). The peaks were broadened with increase in concentration of Ga and which shifted towards high angle. This is because the ionic radius of trivalent Ga^{3+} (0.062 nm) is much smaller than that of Sn^{+4}. An increase in crystallite size is indicated by a decrease in FWHM (Figure 4.19) and macrostrain. Variation in FWHM

suggest crystallite size and strain changes due to different doping levels (Nasir *et al*., 2020). It is observed that the FWHM is inversely proportional to crystal size: crystal size $\alpha \frac{1}{FWHM}$ (Jepngetich *et al*., 2025), the variation was not constant with variation in concentration.

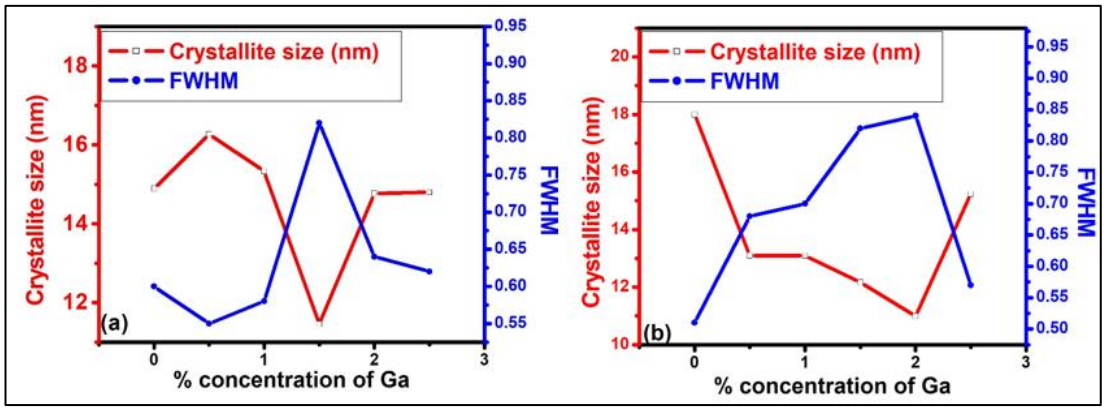


Figure 4.19: Relationship between crystallite size and FWHM of capped (a) and uncapped (b) Ga-SnO_2

The plane (301) was used to obtain lattice parameter a, c and strain (∈) because it had the highest peak. The lattice parameters were calculated using Equations 4.3 and 4.4 (Bett *et al*., 2024). Table 4.9 shows the lattice parameters 'a' and 'c' as well as the micro-strain (∈) values which were computed using Equation 4.2 (Bett *et al*., 2024)

Table 4.9: Lattice parameter (a and c) and micro-strain of capped and uncapped Ga-SnO_2

Dopant concentration	Capped Ga-SnO_2			Uncapped Ga-SnO_2		
	a	c	∈	a	c	∈
0% (Pure Ga-SnO_2	0.2029	0.3313	0.0065	0.2032	0.3318	0.0045
0.5%	0.2034	0.3322	0.0057	0.2032	0.3318	0.0061
1.0%	0.2031	0.3317	0.0060	0.2032	0.3318	0.0063
1.5%	0.2027	0.3310	0.0084	0.2024	0.3305	0.0074
2.0%	0.2028	0.3312	0.0063	0.2024	0.3305	0.0075
2.5%	0.2034	0.3322	0.0062	0.2025	0.3306	0.0052

Figure 4.20 shows the variation of strain with crystal size, it is observed that crystallite size is inversely proportional to strain (Siyalo *et al.*, 2025). Interstitial doping and nanocrystal size fluctuation were identified as the causes of the strain and lattice parameter variations (Saha *et al*., 2015). Changes in strain were attributed to the incorporation of Ga, which introduced lattice distortions and defects (Nasir *et al*., 2020) due to slight difference in ionic radius and different oxidation states, contributed to the reduced crystallite size. Nanoparticles with a smaller crystallite size have a larger surface are to volume ratio thus higher surface energy causing higher strain.

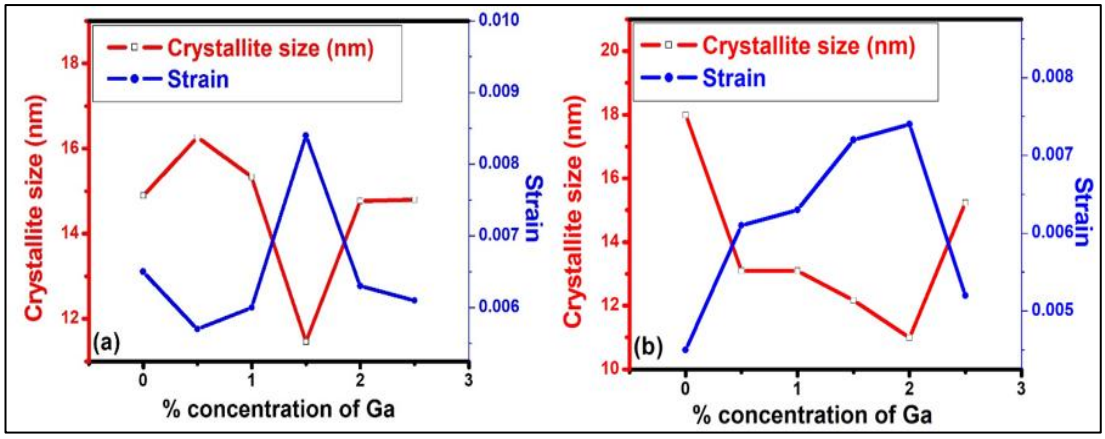


Figure 4.20: Shows the variation in crystallite size and strain for capped (a) and uncapped (b) Ga-SnO_2

4.3.2.3 Photoluminescence analysis of doped nanoparticles

Figure 4.21 and 4.22 depicts room temperature photoluminescence spectra of synthesized pure SnO_2 and Ga-SnO_2 with and without *Psidium guajava* extract respectively. The excitation spectrum has a peak around 264 nm with different peak intensity as shown in Figure 4.21 and 4.22. The absorption peaks suggest that the material absorbs energy causing electrons to move from the valence band to the conduction band, creating excited states. From Figure 4.21, excitation spectra increased when Ga was introduced with 1.0 % showing the highest intensity while 0.5% Ga-SnO_2 had a lowest intensity. From Figure 4.22, pure SnO_2 had the highest intensity and 2.5% Ga-SnO_2 had the lowest intensity.

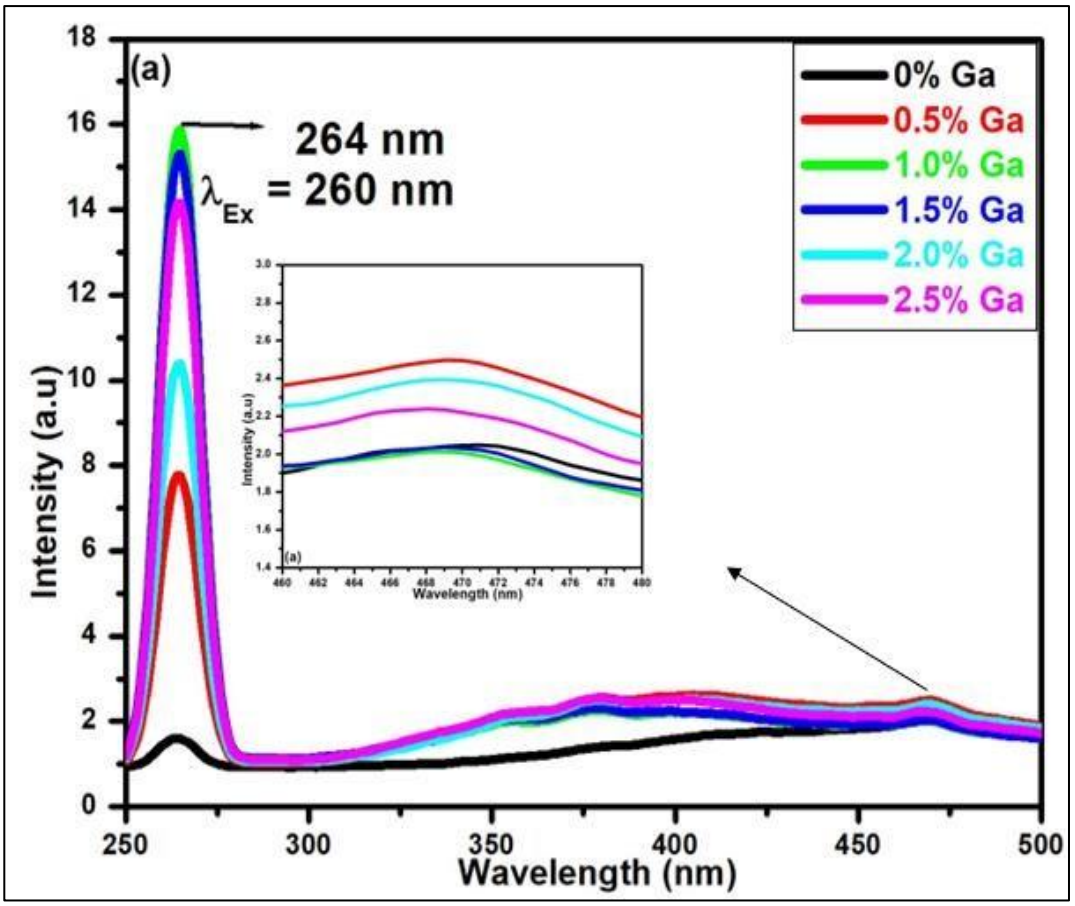


Figure 4.21: Photoluminescence spectra of synthesized pure and Ga-SnO_2 with *P. guajava* extract

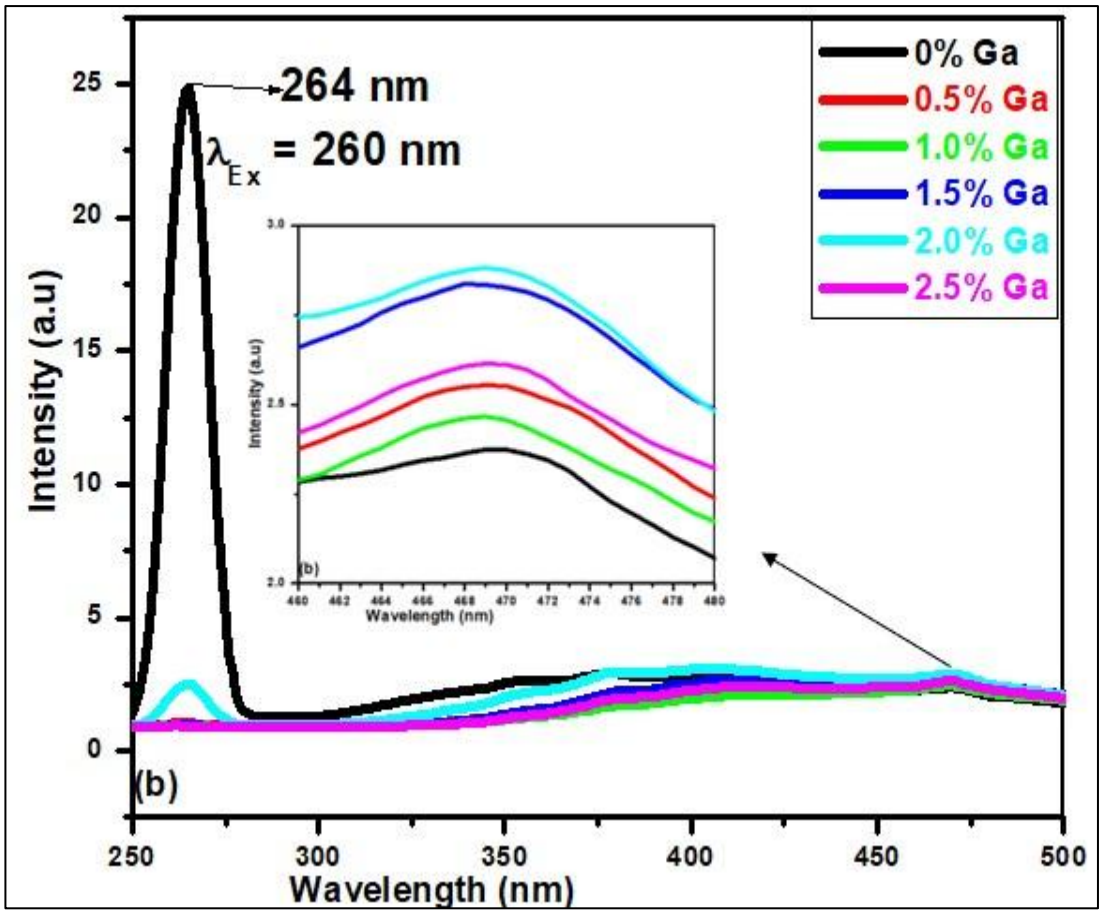


Figure 4.22: Photoluminescence spectra of synthesized pure and Ga-SnO_2 without *P. guajava* extract

Photoluminescent spectra show two types of emission: near band edge emission (NBE) in UV region and defect level emission (DLE) in the visible region. The inset in Figure 4.21 and 4.22 represents the DLE in the range (460 nm – 480 nm) for capped and uncapped Ga-SnO_2 respectively. For SnO_2 and Ga-SnO_2, emission peaks were observed at 354.62, 378.74 and 468.21 nm. The peaks at 354.62 and 378.74 nm corresponding to the near band edge, were attributed to the radiative recombination of the photoexcited electron in the conduction band with the photo generated hole in the valence band (Saha *et al*., 2015) (Dang *et al.*, 2016). Emission in the NBE was also reported in previous research (Seid *et al.,* 2021).

Table 4.10 shows the peak centre and intensity of Ga-SnO_2 synthesized with (a) and without (b) *P. guajava* extract at varying concentration of Ga. For capped Ga-SnO_2, maximum peak intensity was observed at 0.5% with an increment of 0.49 from pure SnO_2. A decrease in intensity was noted at 1.0% and 1.5% Ga-SnO_2 with a decrease of 0.04 and 0.02 respectively. For uncapped Ga-SnO_2, maximum peak intensity was observed at 2.0 % with an increment of 0.53 compared to pure SnO_2. Increase intensity in the visible emission for Ga doped samples has been reported (Siyalo *et al.*, 2025) (Asedy *et al.*, 2017) and (Shinde *et al.*, 2012). Similar red-shift has been observed in the dominant PL peak for other oxide spectra, example, for SnO_2 on doping with Mn (Sabri *et al*., 2012), for ZnO on doping with Ag (Hosseini *et al*., 2015) visible emission corresponds to the transition of photon energy carriers from donor levels of interstitial atoms to the acceptor vacancy levels (Seid *et al*., 2021).

The enhanced intensity is due to the introduction of free carrier concentration (electrons) by gallium and due to the increasing quality of Ga^{3+} acceptors (Dang *et al*., 2016). Also, Ga enhances the radiative recombination process due to introduction of new energy states or localized states within the band gap that allow more efficient electron transitions (Siyalo *et al*., 2025). Decrease in the intensity may be attributed to the decreased quantity of radiative transitions of interstitial oxygens by diffusion to oxygen vacancies (Zebbar *et al*., 2016) similar observation has been reported by Seid *et al* (Seid *et al*., 2021). Addition of a divalent/trivalent ion in a Sn ion, results in an increase in the number of O- vacancies, producing O-vacancies related traps, which make a strong contribution to the luminescence (Bhatnagar *et al.*, 2016)

Enhanced emission properties due to Ga doping can improve the performance of photo catalytic and other optoelectronic devices, where efficient light emission and controlled luminescence are essential. The enhanced UV emission is indicative of an improvement in crystallinity and was verified by the observable decrease in the DLE peak intensity with the increase in mol %. This is due to the decrease in the concentration of interstitial oxygen in the SnO_2 nanostructures which occurs when Ga is doped in SnO_2. In the process the residual O ions get consumed by Ga^{+3} ions (Pham *et al.,* 2014*)*. Doping with Ga enhances light absorption and prolongs the

lifetime of photo-generated carriers. This enhancement is essential for photocatalytic processes while the newly introduced energy levels may serve as intermediate states, facilitating multiphoton absorption and subsequently improving the efficiency of photocatalysis under visible or near-ultraviolet light (Siyalo *et al.,* 2025).

Table 4.10: Peak centre and intensity of Ga-SnO_2 at varying mol concentration of gallium

Dopant concentration	**Capped Ga-SnO_2**		**Uncapped Ga-SnO_2**	
	Peak centre (nm)	Intensity (a.u)	Peak centre (nm)	Intensity (a.u)
0% (Pure SnO_2)	471.12	2.03	470.16	2.31
0.5%	468.71	2.52	468.99	2.58
1.0%	468.74	1.98	468.99	2.46
1.5%	468.50	2.0	468.95	2.80
2.0%	468.87	2.40	468.99	2.84
2.5%	468.90	2.22	468.92	2.62

4.3.2.4 FTIR analysis of doped nanoparticles

FTIR Spectroscopy was used to identify the chemical bonding and functional groups in both capped and uncapped Ga-SnO_2. Figure 4.23 shows the FTIR spectra in the range 400-4000 cm^1 for capped (a) and uncapped (b) NPs. The stretching of Sn-O for capped and uncapped SnO_2 is responsible for the peaks at 783.42 and 698.21 cm^{-1} respectively. O-H bending, probably from phenolic compounds, is responsible for the peak at 954.09 cm^{-1} for capped SnO_2, whereas O-H bending, most likely from water and hydroxyl groups, is responsible for the peak at 892.33 cm^1 for uncapped Ga-SnO_2. For both capped and uncapped SnO_2, the peak at 1148.69 and 1063.51 is caused by C-O stretch. For capped Ga-SnO_2, the peak is an indicative of alcohol or ester group while the peak at 1389.46 and 1326.39 cm^{-1} for capped and uncapped Ga-SnO_2 is due to C-H bending. Peak at 2982.46 (capped) and 2921.90 cm^{-1} (uncapped) typically indicates C–H stretching vibrations, which can be associated with aliphatic or

potentially aromatic groups. The peak at 3662 cm^{-1} (capped) and 3604 cm^{-1} (uncapped) is due to O-H stretching indicative of hydroxyl group.

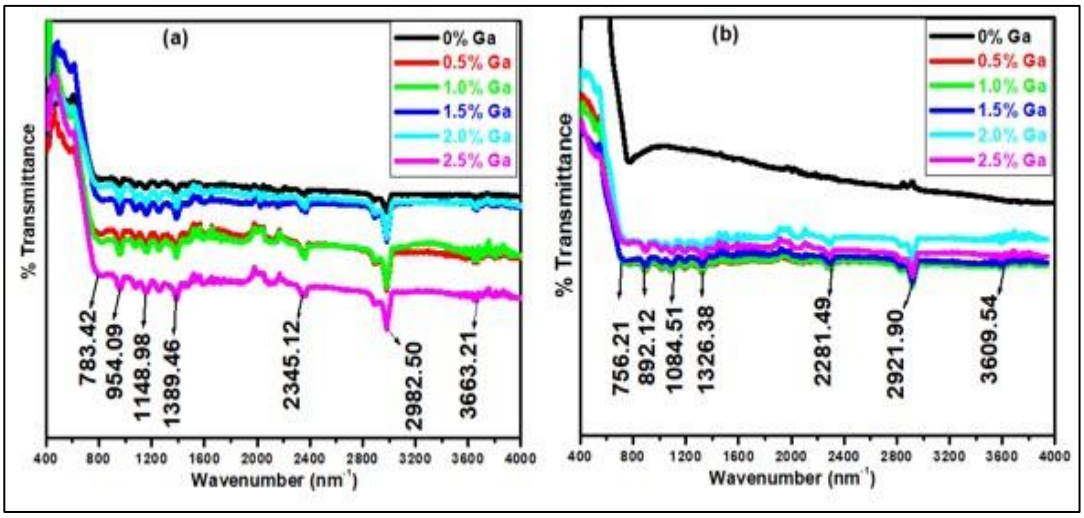


Figure 4.23: FTIR spectra of capped (a) and uncapped (b) Ga-SnO_2 at varying concentrations of the dopant

4.4 Effects of varying Al and Ga co-doping ratios on the structural, luminescence and optical properties of tin oxide nanoparticles

4.4.1 Optical analysis of co-doped nanoparticles

Figure 4.24 shows the absorption spectra of SnO_2 and Al:Ga co-doped SnO_2 synthesized with (a) and without (b) *psidium guajava* extract. Absorption was observed at a wavelength range 290-310 nm for capped Al:Ga-SnO_2. For uncapped Al:Ga-SnO_2, a weak absorption was observed from 400-600 nm after which a strong absorption was noted from 300-400 nm. Intensity of the diffraction peak was greatest at 50%:50% Al:Ga-SnO_2 and lowest for pure SnO_2 for both capped and uncapped Al:Ga SnO_2. The absorption is due to electronic transition from valency band to conduction band. The higher-intensity peak is due to numerous aspects, including oxygen deficiency, particle size and defects in the grains (Thamarai *et al.,* 2018).

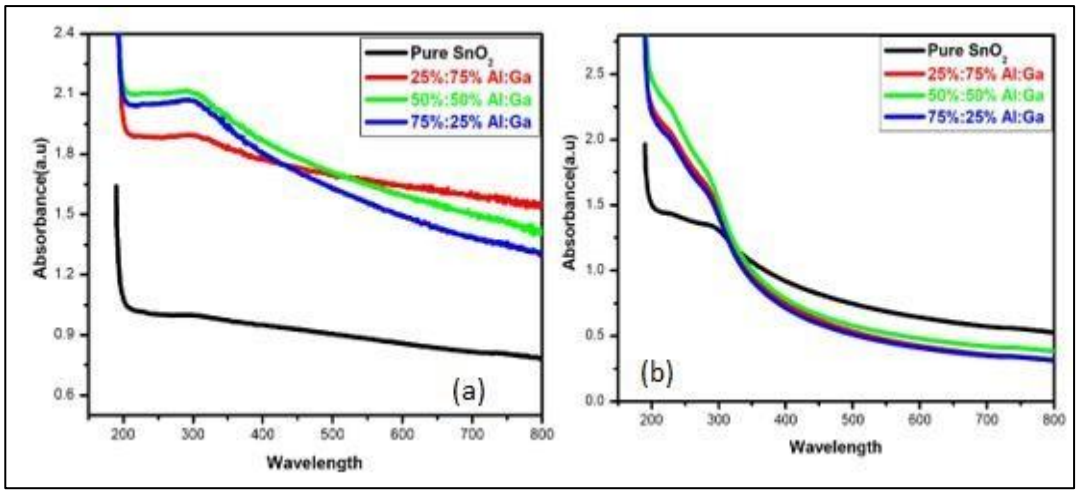


Figure 4.24: UV-Vis spectra of synthesized pure SnO_2 and Al-Ga-SnO_2 co-doped SnO_2 with (a) and without (b) *P. guajava* extract

A plot of $(\alpha hv)^2$ dependence against hv shown in Figure 4.25 (a) and (b) is done to determine the band gap energy by extrapolating the straight-line portion of the absorption edge to the energy axis. The x-intercept values are tabulated in the table 4.11. The band gap of a TCO is controlled by two opposing effects; the band-gap widening (BGW) or Moss-Burstein (B.M) effect and the band-gap narrowing (BGN) or Urbach effect in addition to the other variations in the electronic band structure induced by doping effects (Jasim *et al*., 2021). Increase stability, enhanced crystallinity, and the introduction of beneficial electronic states are the reasons behind the decrease in the band gap for Al and Ga co-doped tin oxide.

The presence of organic components from the leaf extract led to hybridization effects in the electronic states, altering the band structure and contributing to a reduced band gap. The general electrical structure of the material can be altered by doping, which can introduce energy levels into the band-gap. The increased density of defects in the nanostructures caused by the competing co-dopant atoms may cause the band gaps narrowing for the co-doped sample (Musa *et al*., 2019). The band gap of the crystallite samples where the transitions can occur is reduced as a result of the integrated free carrier impurity atoms creating new localized recombination states below the conduction band minimum (M. *et al*., 2018). Furthermore, relatively larger decrease

in the band gaps results from disorder in the crystalline structures caused by increased strain in the co-doped samples (Ng *et al.,* 2017). Band gaps and crystallite size are expected to shift in the opposite directions, however there are additional explanations for this condition, such as the quantum size effect, which can cause the band gaps to shrink (Papadimitriou *et al,* 2016). Reduced band gaps may also result from the band gap renormalization effect, which can be caused by the Coulombic interactions between excess free electrons in the conduction band and electron-impurity scatterings (Rivera *et al*., 2016). The size, shape, and crystallinity of nanoparticles can also change as a result of modifications to the synthesis conditions and methods, which can all have an impact on the band-gap energy (Droepenu *et al*., 2022)

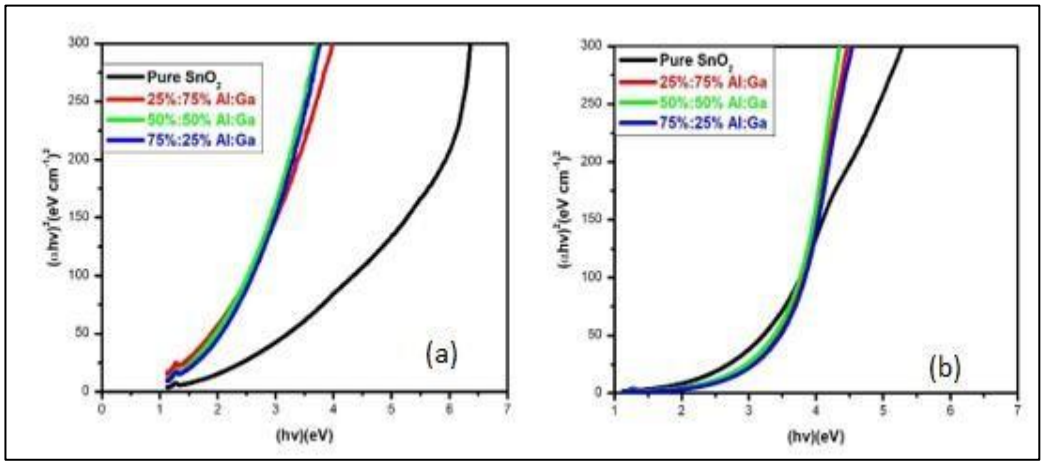


Figure 4.25: Tauc's plot extrapolation of synthesized pure SnO_2 and Al-Ga-SnO_2 co-dopped SnO_2 with (a) and without (b) *P. guajava* extract

Table 4.11: Energy band gap (eV) of pure SnO_2 and Al:Ga-SnO_2 synthesized with and without *P. guajava* extract

Dopant concentration	Capped	Uncapped
0% Al:Ga-SnO_2	3.89	3.21
25%:75%	1.58	3.06
50%:50%	1.61	3.14
75%:25%	1.69	3.08

4.4.2 XRD analysis of co-doped nanoparticles

Figure 4.26 show the XRD pattern of SnO_2 and Al:Ga-SnO_2 co-doped tin oxide synthesized with (a) and without (b) *psidium guajava* extract. Peaks in the spectra are identified as originating from reflections from (110), (101), (200), (211), (220), (002), (310), (301), (202) and (321) miller index. All the samples exhibited a tetragonal rutile structure when compared with the standard JCPDS of SnO_2 (Card no. 41-1445). Except capped SnO_2 all other samples displays formation of secondary phases or impurities. This is due to the liberation of tiny amount of tin ion which accumulated in form of tinny clusters causing a reflection at 46°.

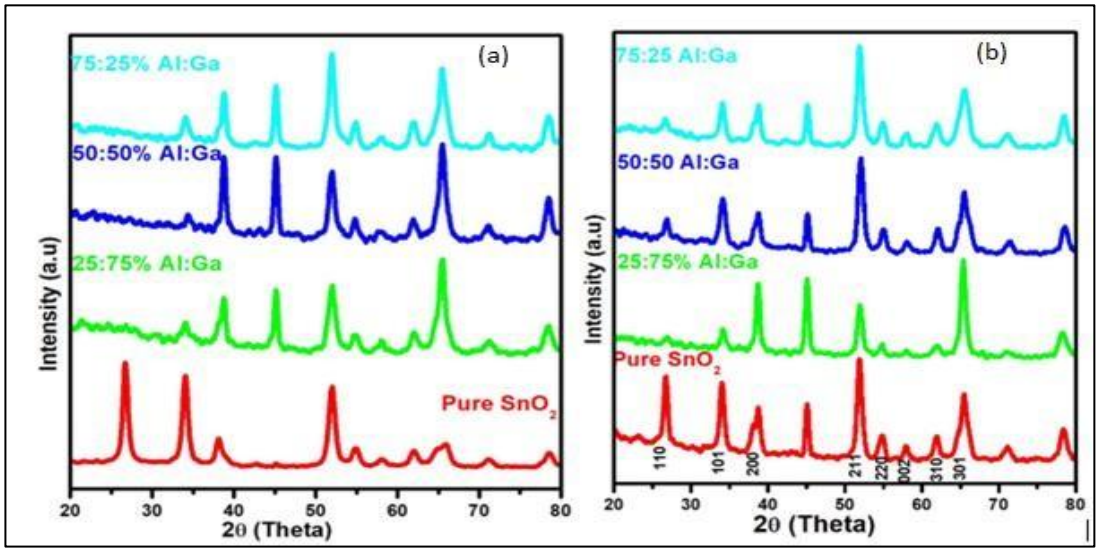


Figure 4.26: XRD pattern of synthesized SnO_2 and AlGa-SnO_2 with (a) and without (b) *P. guajava* extract in the range 20°-80°

The crystallite size was estimated using Scherrer equation (Equation 1) and results presented in Table 4.12. For capped Al:Ga-SnO_2, co-doping caused an increase in the crystal size except 75%:25% Al:Ga-SnO_2. From figure 27 (a), 25%:75% and 75%:25% Al:Ga-SnO_2 had a smallest and largest FWHM respectively. From figure 27 (b), 25%:75% and 50%:50% had a smallest and largest FWHM, respectively. For capped Al:Ga-SnO_2, its observed that FWHM had an impact on crystallite size, 25%:75% had a highest crystallite size with smallest FWHM and 75%:25% had a smallest crystallite size with increased FWHM. The same relationship of crystallite size and FWHM was observed for uncapped Al:Ga-SnO_2 hence suggesting that crystallite size $\alpha \frac{1}{FWHM}$

Table 4.12: 2θ, full width at half maximum (FWHM), average FWHM, crystallite size (D) and average D of Al:Ga-SnO_2

	Plane	**Capped Al:Ga-SnO_2**				**Uncapped Al:Ga-SnO_2**			
2θ		0%	25:75	50:50	75:25	0%	25:75	50:50	75:25
	101	34.04	34.04	34.39	34.09	34.03	34.17	34.12	34.08
	200	38.16	38.75	38.76	38.77	38.73	38.71	38.64	38.76
	211	51.98	51.97	51.96	51.96	51.91	51.95	52.07	51.94
	301	65.83	65.45	64.49	65.50	65.48	65.38	65.51	65.51
FWHM	101	0.6046	0.5523	0.6276	0.7890	0.5318	0.4935	0.6906	0.5886
	200	0.6162	0.3566	0.4535	0.5398	0.3521	0.4340	0.7543	0.3451
	211	0.7299	0.7420	0.6509	0.59741	0.6089	0.6409	0.6709	0.6202
	301	0.4727	0.5309	0.5822	0.6023	0.5253	0.6095	0.4962	1.0416
Average		0.6059	0.5455	0.5786	0.6322	0.5045	0.5445	0.6530	0.6489
D (cm)	101	13.74	15.04	13.25	10.53	15.62	16.84	12.03	14.12
	200	13.64	23.61	18.57	15.60	23.91	19.40	11.16	24.20
	211	12.11	11.91	13.58	14.79	14.51	13.79	13.18	14.25
	301	20.02	17.78	16.22	15.68	17.97	15.49	19.03	9.67
D Average		14.89	17.09	15.41	14.15	18.00	16.38	13.86	15.61

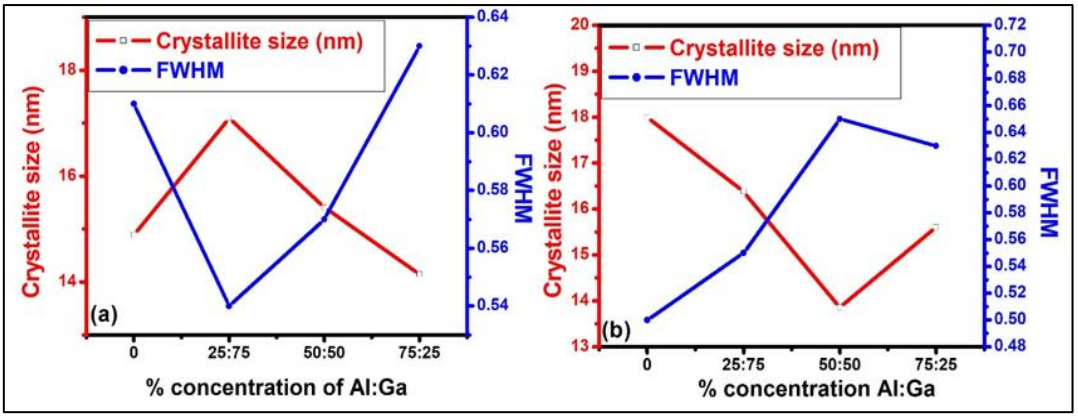


Figure 4.27: Variation of FWHM with crystallite size with (a) and without (b) *P. guajava* extract

Dislocation density and Micro-strain (∈) were computed using the equation 4 and 7 respectively as Table 4.13 show the results. For capped and uncapped Al:Ga-SnO_2, it is observed that crystallite size $\alpha \frac{1}{Strain}$, hence 25%:75% capped and uncapped Al:Ga-SnO_2, had the largest crystallite size and smallest strain. Nanocrystal size fluctuation was identified as the causes of the strain and lattice parameter variations (Saha *et al*., 2015). Changes in strain were attributed to the incorporation of Al^{3+} and Ga^{3+}, which introduced lattice distortions and defects (Nasir *et al*., 2020) due to slight difference in ionic radius. This strain distorts the lattice parameters by creating oxygen vacancies, filling interstitial sites, rearranging atoms, and reducing the charge to maintain crystal charge neutrality.

Change in strain confirms the creation of defects as SnO_2 tries to accommodate the foreign atoms of Al and Ga in its lattice structure. The dislocation network within the structure is indicated by the dislocation density and is inversely proportional to crystallite size. Capped 75%:25% Al:Ga-SnO_2 had the highest dislocation density and strain value with small D value while uncapped 50:50% SnO_2:Al-Ga had the highest dislocation value and highest strain value with small D value. For capped 25%:75% and 50%:50% Al:Ga-SnO_2, the increase in the crystallite size was attributed due to the reduced strain and FWHM as seem in figure 4.28 and 4.29 respectively. The changes in lattice parameters and crystallite size of nanoparticles are due to thermal

strain and presence of impurities. In exception of uncapped 75;25 Al:Ga-SnO_2, dislocation density increased when Al and Ga was introduced into SnO_2 lattice. In exception of uncapped 75;25 Al:Ga-SnO_2, dislocation density increased when Al and

Ga was introduced into SnO_2 lattice At miller indices (301), both capped and uncapped Al:Ga- SnO_2 showed an increase in the 2theta when compared to the peak position at the JCPDS (51.78).

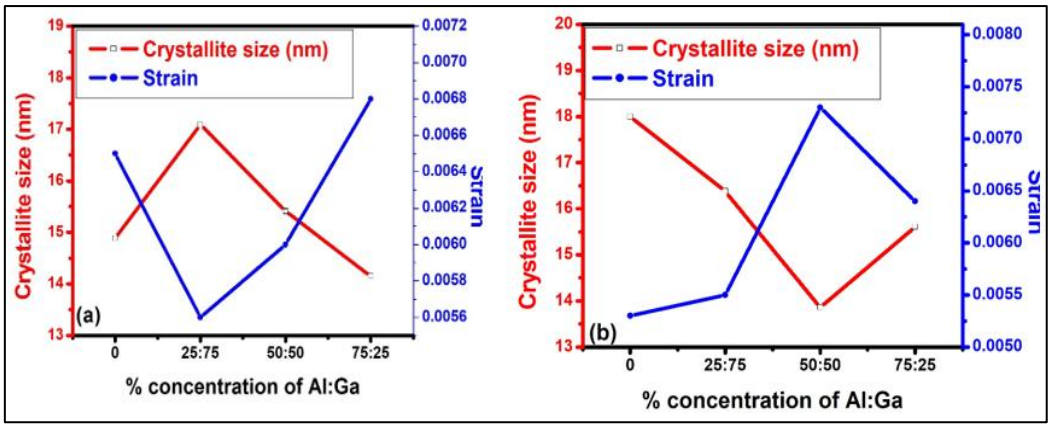


Figure 4.28: Variation between crystal size and strain of capped (a) and uncapped (b) Al:Ga-SnO_2

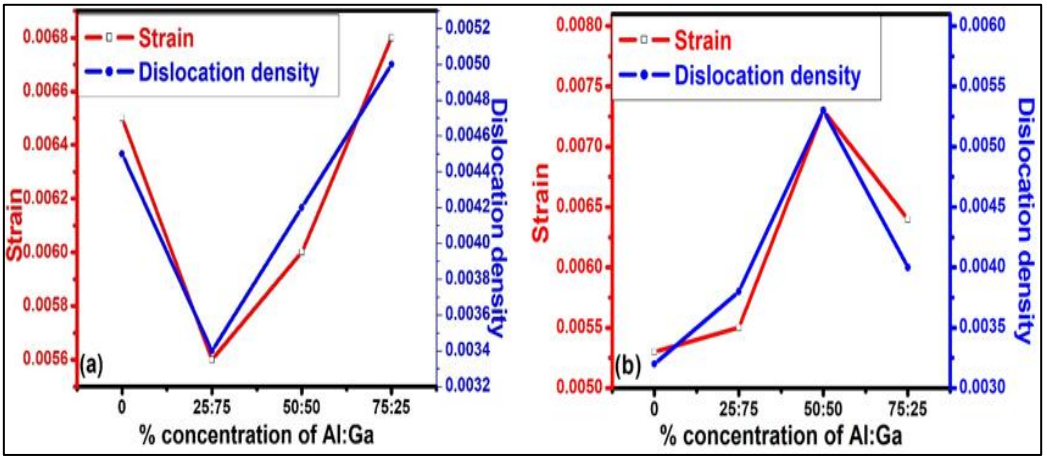


Figure 4.29: Dislocation density and strain of capped (a) and uncapped (b) Al:Ga-SnO_2

Table 4.13: Dislocation density and micro strain of Al:Ga-SnO_2

(211)	Capped Al%:Ga%-SnO_2				Uncapped Al%:Ga%-SnO_2			
	0%	25:75	50:50	75:25	0%	25:75	50:50	75:25
$\delta) \times 10^{-3}$	4.5	3.4	4.2	5.0	3.1	3.7	5.2	4.1
$\in \times 10^{-3}$	6.5	5.6	6.1	6.8	5.3	5.6	7.2	6.4

4.4.3 Photoluminescence analysis of co-doped nanoparticles

Figure 4.30 illustrates the room-temperature PL spectra of pure SnO_2 and Al:Ga SnO_2 in wavelength 250-500 nm, at an excitation wavelength of 260 nm. Electron–hole separations, electron–phonon scattering and electron–hole recombination yields the PL spectra of prepared samples. The most common defects in semiconductor nanocrystals are oxygen vacancies, which serve as the visible light's radiative center (Layek *et al*., 2012). The spectra are divided into UV and visible light (450–650 nm) parts. The UV emission associated with free exciton–exciton collision processes is ascribed to the near band edge (NBE). The visible emission of SnO_2 happens because of defects which form deep energy levels in the band gap. The emission peak shows peak at uv and visible region (450-650 nm) as seen in figure 4.30 (a) and (b). The spectra of capped and uncapped Al:Ga-SnO_2 involves a weak emission peak at 354.62 and 378.74 nm and a strong broad peak at 468.21 nm. Weak emission peak at 354.62 and 378.74 nm is associated with free exciton–exciton collision processes and is ascribed to the near band edge (NBE), which is due to direct radiative recombination of conduction electrons in the tin 4p conduction band and a hole in the oxygen (O) 2p valence band (Thankaian *et al.*, 2022).

Peak at the visible region (468.21 nm) happen: because of defects which form deep energy levels in the band gap. The inset in figure 30 (a) and (b) for both capped and uncapped Al:Ga-SnO_2, shows that 75%:25% Al:Ga-SnO_2 has a higher intensity with an increment of 0.26 and 0.36 from pure SnO_2 respectively. Increase in intensity for in visible region was reported (Thankaian *et al*., 2022). The broad visible emission band is primarily caused by existence of anion vacancies, which may result from

surface-bound electrons passing through already existing trapped holes (Kock *et al.*, 2008). Compared to the NBE peak, the emission in the DLE is more pronounced, this suggests that the DLE is more favourable to carrier recombination than that in NBE (Tiwari *et al*., 2020). Increasing the aluminium content in Al:Ga SnO_2, leads to an increase intensity in DLE, this is because Al can modify the band structure and create additional energy levels within the band gap, which may enhance DLE by providing more pathways for electron-hole recombination.

Table 4.14: Peak centre and intensity of Al:Ga-SnO_2

Al%:Ga%	**Capped**		**Uncapped**	
	Peak centre	Intensity	Peak centre	Intensity
0% SnO_2	468.85	2.01	465.49	2.33
25%:75%	466.99	2.22	468.01	2.32
50%:50%	468.16	2.18	467.16	2.62
75%:25%	467.17	2.27	466.67	2.69

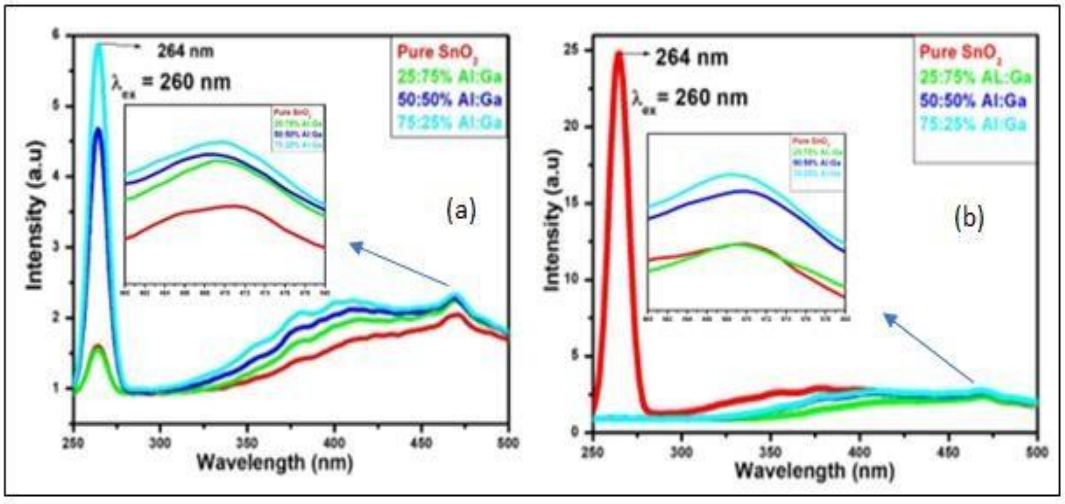


Figure 4.30: Pl spectra of capped (a) and uncapped (b) Al:Ga-SnO_2

4.4.4 FTIR analysis Al and Ga co-doped nanoparticles

Figure 4.31 shows the FTIR spectra of capped and uncapped Al:Ga-SnO_2, in the range 4004000 cm^{-1}. The peak at 843.62 and 821.72 for capped and uncapped Al:Ga-SnO_2 associated with bending vibrations of Sn-O bonds, indicating the presence of tin oxide. Peak at 1517.23 cm^{-1} could relate to C=C stretching vibrations, for capped sample the peak is due to the presence of organic compound preset in *psidium guajava*. Peak at 2147.44 cm^{-1} indicate C≡C stretching vibrations. peak at 3388.18 cm^{-1} 3351.90 cm^{-1} corresponds to O-H stretching, suggesting the presence of hydroxyl groups, likely from moisture or surface hydroxylation.

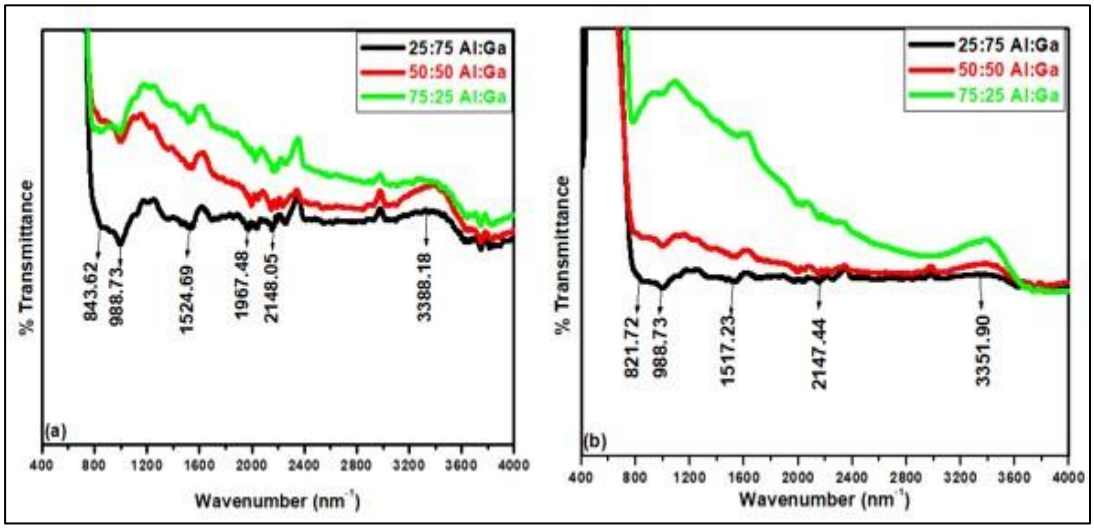


Figure 4.31: FTIR spectra of capped (a) and uncapped (b) Al:Ga SnO_2

4.5 Chapter Summary

Psidium guajava capped Al, Ga and Al-Ga-SnO_2 nanoparticles were successfully synthesized using green synthesis method, the FT-IR showed stretching vibration in both the functional group and figure print region. The figure print region showed metal oxide stretching vibration for doped and undoped nanoparticles. XRD confirms the formation of tetragonal rutile structure of tin oxide nanoparticles. Pl emission showed the increase in emission peak when higher concentration of dopant was used and lastly

the UV-Vis results showed a relatively low bandgap energy at high doping concentration

CHAPTER FIVE
CONCLUSION AND RECOMMENDATIONS

5.1 Conclusion

Nanoparticles of SnO_2, Al-SnO_2, Ga-SnO_2 and Al:Ga-SnO_2 were successfully synthesized using *psidium guajava* extract. The presence of capping agent, different mole concentration of Al and Ga and co-doping Al:Ga-SnO_2 affects the properties of tin oxide nanoparticles. XRD spectra verify that both capped and uncapped SnO_2 had a tetragonal rutile structure confirmed by JCPDs card 00-41-1445. Crystallite size calculated from Debye-Scherrer equation shows that the use of capping agent to synthesize SnO_2 reduced the crystallite size from 18.00 to 14.89 nm. Capped SnO_2, maintained the peak patter and caused an increase in the peak intensity than uncapped SnO_2. Capping agent caused an increase in the band gap when compared to uncapped SnO_2, therefore suggesting a change in the optical properties of SnO_2. Pl spectroscopy shows a decrease in the Pl intensity when compared to uncapped SnO_2 suggesting presence of different defects in SnO_2. FTIR analysis was used to determine the presence of functional group in the prepared NPs, capped SnO_2 shows peaks at both fingerprint region and functional group region while uncapped SnO_2 only shows peak at finger print region.

Al-SnO_2 and Ga-SnO_2 were successfully synthesized with different concentration of dopant (0.5, 1.0, 1.5, 2.0 and 2.5 %) using *psidium guajava* extract. Tauc equation was used to determine the band gap, Al and Ga doping caused a decrease in the band gap. For Al doping, smallest band gap was obtained at 1.5% and 0.5% for capped and uncapped SnO_2 with a band gap value of 2.01 and 3.38 eV respectively. For Ga doping, smallest band gap was obtained at 0.5 % and 1.0 % for capped and uncapped SnO_2 with a band gap value of 2.29 and 2.32 eV respectively. XRD spectra verifies that Al-SnO_2 and Ga-SnO_2 had a tetragonal rutile structure confirmed by JCPDS card file no 00-41-1445. Crystallite size calculated from Debry-Scherrer equation shows that Al and Ga doping synthesized with and without *psidium guajava* extract caused a decrease in crystallite size. For capped Al- doping, crystallite size was in the range of14.89-10.57 nm and 18.00-12.75 nm for capped and uncapped Al-SnO_2. For Ga-

SnO_2, crystallite size was in the range of 16.27-11.46 nm and 18.00-10.99 nm for capped and uncapped Ga-SnO_2. The crystallite size was inversely proportional to strain and FWHM. Absorption spectrum was obtained when the samples were characterized using UV-Vis spectroscopy. The sample were dissolved water and scan at a wavelength of 200-800 nm. Taucs extrapolation was plotted to obtain the band gap energies. The bandgap energies decreased when Al was doped in Tin oxide from 3.98 -2.01 eV and 3.21-2.38 eV for capped and uncapped Al-SnO_2.For Ga doping, the band gap decreased from 3.98-2.29 eV and 3.21-2.46 eV for capped and uncapped Ga-SnO_2 respectively.

Photoluminescence spectroscopy was used to determine the defect in *psidium guajava* capped and uncapped SnO_2. The spectra were obtained at room temperature at an excitation energy of 260 nm. When SnO_2 was doped with Al and Ga, all the samples emit strongly in the UV region, with a band cantered at 264 nm corresponding to exitonic emission when exited at 260 nm. For Al doping, 1.5 % and 0.5 % had the highest peak intensity for capped and uncapped Al-SnO_2 respectively. For Ga doping, 1.0 % and 2.0 % had the highest and lowest intensity for capped and uncapped SnO_2 respectively. Emission spectra at 460-480 nm was also observed. 2.0% capped and uncapped Al-SnO_2, had the highest emission intensity. For Ga doping highest emission intensity was observed at 0.5 % and 2.0 % for capped and uncapped Ga-SnO_2 respectively. The FTIR spectra confirms the presence of functional group in both capped and uncapped Al and Ga-SnO_2. Functional group was observed at finger print and functional group region.

Al and Ga were successfully incorporated in tin oxide lattice, the effect of co-doping Al and Ga in tin oxide was monitored by UV-Vis, XRD, Pl and FTIR. From UV-Vis results, Al and Ga were observed to cause a decrease in band gap. Capped Al:Ga-SnO_2, caused a large band gap decrement compared to uncapped Al:Ga-SnO_2. Tetragonal rutile structure of tin oxide was maintained as confirmed by XRD spectra. Increase in crystallite size was observed at 25%;75% and 50%:50% capped Al:Ga-SnO_2 having value 17.09 and 15.41 nm respectively. Capped Al:Ga caused a decrease in the crystallite size with smallest crystallite size observed at 50%:50% Al:Ga-SnO_2

and the largest crystallite size observed at 25:75 % Al: Ga-SnO_2. The crystallite size was observed to be inversely proportional to FWHM and strain. FTIR analysis confirms the presence of functional group which were in the fingerprint and functional group region. SnO_2 co-dopped with Al and Ga shows an increase intensity in the DLE with 75:25 Al:Ga-SnO_2 having the highest and lowest intensity for capped and uncapped Al:Ga-SnO_2 respectively.

5.2 Recommendations

5.2.1 Recommendations for Policy

From the findings of this study the following optimum conditions for preparation of nanoparticles with potential solar cell application are recommended

1. *Psidium guajava* is recommended for synthesizing tin oxide nanoparticles
2. 2% (capped) and 1.5% (uncapped) Al dopant is recommended for doping in tin oxide. For Ga-doped SnO_2, 2.5% (capped) and 1.5% (uncapped) were recommended
3. 75%:25% capped and 50%:50% (uncapped) Al:Ga-SnO_2 were recommended

5.2.2 Recommendations for future work

1. *Psidium guajava* capped Al and Ga to be tested in photoanode of solar cell.
2. Other transition metals oxides such as zinc oxide, titanium oxide transition metals and analysed for potential application as photoanode.
3. This research recommends further research on doping SnO_2 with other dopants and co-doping with transitional elements for photoanode applications.
4. Further studies should focus on optimizing reaction condition, extract concentration, temperature and reaction time to improve nanoparticles yield and quality.
5. To deepen understanding of the material's properties and enhance performance optimization, future studies could consider additional methods such as Scanning Electrode microscope for morphological analysis

REFERENCES

Abdelghany, T. M., Al-Rajhi, A. M. H., Al Abboud, M. A., Alawlaqi, M. M., Ganash Magdah, A., Helmy, E. A. M., & Mabrouk, A. S. (2018). Recent Advances in Green Synthesis of Silver Nanoparticles and Their Applications: About Future Directions.A Review *BioNanoScience*, *8*(1), 5–16. https://doi.org/10.1007/s12668-017-0413-3

Adam, F., Chew, T.-S., & Andas, J. (2011). A simple template-free sol–gel synthesis of spherical nanosilica from agricultural biomass. *Journal of Sol-Gel Science and Technology*, *59*(3), 580–583. https://doi.org/10.1007/s10971-011-2531-7

Adnan, R., Razana, N. A., Rahman, I. A., & Farrukh, M. A. (2010). Synthesis and Characterization of High Surface Area Tin Oxide Nanoparticles via the Sol-Gel Method as a Catalyst for the Hydrogenation of Styrene. *Journal of the Chinese Chemical Society*, *57*(2), 222–229. https://doi.org/10.1002/jccs.201000034

Agrahari, V., Tripathi, A. K., Mathpal, M. C., Pandey, A. C., Mishra, S. K., Shukla, R. K., & Agarwal, A. (2015). Effect of Mn doping on structural, optical and magnetic properties of SnO2 nanoparticles. *Journal of Materials Science: Materials in Electronics*, *26*(12), 9571– 9582. https://doi.org/10.1007/s10854-015-3620-0

Ahmed, A. S., Shafeeq M., M., Singla, M. L., Tabassum, S., Naqvi, A. H., & Azam, A. (2011). Band gap narrowing and fluorescence properties of nickel doped SnO2 nanoparticles. *Journal of Luminescence*, *131*(1), 1–6.

Ahmed, S., & Ikram, S. (2015). Silver nanoparticles: One pot green synthesis using Terminalia arjuna extract for biological application. *J. Nanomed. Nanotechnol*, *6*(4), 1–6.

Al-Asedy, H. J., Ati, A. A., Bidin, N., & Lee, S.-L. (2017). Gallium contents-dependent improved behavior of sol–gel-grown Al:Ga co-doped ZnO nanostructures. *Applied Physics A*, *123*(10), 665. https://doi.org/10.1007/s00339-017-1271-0

Alsammarraie, F. K., Wang, W., Zhou, P., Mustapha, A., & Lin, M. (2018). Green synthesis of silver nanoparticles using turmeric extracts and investigation of their

antibacterial activities. *Colloids and Surfaces B: Biointerfaces*, *171*, 398–405. https://doi.org/10.1016/j.colsurfb.2018.07.059

Altaf, U., Ansari, M. Z., & Rubab, S. (2023). Influence of aluminium doping on structural and optical properties of tin oxide nanoparticles. *Materials Chemistry and Physics*, *297*, 127304. https://doi.org/10.1016/j.matchemphys.2023.127304

Amrute, V., Monika, Supin, K. K., Vasundhara, M., & Chanda, A. (2024). Observation of excellent photocatalytic and antibacterial activity of Ag doped ZnO nanoparticles. *RSC Advances*, *14*(45), 32786–32801. https://doi.org/10.1039/D4RA05197A

Anandalakshmi, K., Venugobal, J., & Ramasamy, V. (2016). Characterization of silver nanoparticles by green synthesis method using Pedalium murex leaf extract and their antibacterial activity. *Applied Nanoscience*, *6*(3), 399–408. https://doi.org/10.1007/s13204015-0449-z

Annadhasan, M., Kasthuri, J., & Rajendiran, N. (2015). Green synthesis of gold nanoparticles under sunlight irradiation and their colorimetric detection of Ni2+ and Co2+ ions. *RSC Advances*, *5*(15), 11458–11468.

Anu Mary Ealia, S., & Saravanakumar, M. P. (2017). A review on the classification, characterisation, synthesis of nanoparticles and their application. *IOP Conference Series: Materials Science and Engineering*, *263*, 032019.

Aoki, T. (2012). Photoluminescence Spectroscopy. In E. N. Kaufmann (Ed.), *Characterization of Materials* (1st ed., pp. 1–12). Wiley. https://doi.org/10.1002/0471266965.com058.pub2

Azam, A., Ahmed, A. S., Chaman, M., & Naqvi, A. H. (2010). Investigation of electrical properties of Mn doped tin oxide nanoparticles using impedance spectroscopy. *Journal of Applied Physics*, *108*(9), 094329. https://doi.org/10.1063/1.3506691

Bansal, M., Bansal, A., Sharma, M., & Kanwar, P. (2015). Green synthesis of gold and silver nanoparticles. *Research Journal of Pharmaceutical, Biological and Chemical Sciences*, *6*, 1710–1716.

Banyamin, Z., Kelly, P., West, G., & Boardman, J. (2014). Electrical and Optical Properties of Fluorine Doped Tin Oxide Thin Films Prepared by Magnetron Sputtering. *Coatings*, *4*(4), 732–746.

Baraneedharan, P., Imran Hussain, S., Dinesh, V. P., Siva, C., Biji, P., & Sivakumar, M. (2015). Lattice doped Zn–SnO2 nanospheres: A systematic exploration of dopant ion effects on structural, optical, and enhanced gas sensing properties. *Applied Surface Science*, *357*, 1511–1521. https://doi.org/10.1016/j.apsusc.2015.09.257

Benouis, C. E., Benhaliliba, M., Mouffak, Z., Avila-Garcia, A., Tiburcio-Silver, A., Ortega Lopez, M., Romano Trujillo, R., & Ocak, Y. S. (2014). The low resistive and transparent Al-doped SnO2 films: P-type conductivity, nanostructures and photoluminescence. *Journal of Alloys and Compounds*, *603*, 213–223. https://doi.org/10.1016/j.jallcom.2014.03.046

Bhatnagar, M., Kaushik, V., Kaushal, A., Singh, M., & Mehta, B. R. (2016). Structural and photoluminescence properties of tin oxide and tin oxide: C core–shell and alloy nanoparticles synthesised using gas phase technique. *AIP Advances*, *6*(9). https://pubs.aip.org/aip/adv/article/6/9/095321/884807

Bhattacharjee, A., & Ahmaruzzaman, M. (2015). Photocatalytic-degradation and reduction of organic compounds using SnO2 quantum dots (via a green route) under direct sunlight. *RSC Advances*, *5*(81), 66122–66133. https://doi.org/10.1039/C5RA07578E

Bhattacharjee, A., Ahmaruzzaman, M., Devi, Th. B., & Nath, J. (2016). Photodegradation of methyl violet 6B and methylene blue using tin-oxide nanoparticles (synthesized via a green route). *Journal of Photochemistry and Photobiology A: Chemistry*, *325*, 116–124. https://doi.org/10.1016/j.jphotochem.2016.03.032

Bhuyan, K., Bhattacharjee, A., & Alapati, P. R. (2018). Sensing of ammonia gas by undoped and aluminum-doped tin oxide nanoparticles by Raman spectroscopy. *Pramana*, *91*(3), 32. https://doi.org/10.1007/s12043-018-1605-2

Binadi, T. R., Mishra, P., Poudel, B. R., & Gautam, S. K. (2025). Green Synthesis of Tin Oxide Nanoparticles using Psidium guajava Leaves Extract and its Applications

in Antibacterial and Antioxidant Activities. *Journal of Nepal Chemical Society*, *45*(1), 133–142. https://doi.org/10.3126/jncs.v45i1.74493

Blanco Andujar, C. (2014). Sodium carbonate mediated synthesis of iron oxide nanoparticles to improve magnetic hyperthermia efficiency and induce apoptosis [Doctoral, UCL

(University College London)]. In *Doctoral thesis, UCL (University College London)*. (p. ??). https://discovery.ucl.ac.uk/id/eprint/1430360/

Bunaciu, A. A., Udriştioiu, E. gabriela, & Aboul-Enein, H. Y. (2015). X-Ray Diffraction:

Instrumentation and Applications. *Critical Reviews in Analytical Chemistry*, *45*(4), 289299.

Buniyamin, I., Akhir, R. M., Asli, N. A., Khusaimi, Z., Malek, M. F., & Mahmood, M. R. (2022). Nanotechnology Applications in Biomedical Systems. *Current Nanomaterials*, *7*(3), 167–180.

Changchun Chen, Lin Wang, JiangFeng Liu, Benhai Yu, & Ping Liu. (2011). Investigation of nano-sized ZnO particles fabricated by various synthesis routes. *Journal of Ceramic Processing Research*, *12*(4), 420–425. https://doi.org/10.36410/JCPR.2011.12.4.420

Chan y Díaz, E., Duarte-Moller, A., Camacho, J. M., & Castro-Rodríguez, R. (2012). SnO2 thin films grown by pulsed Nd:YAG laser deposition. *Applied Physics A*, *106*(3), 619–624. https://doi.org/10.1007/s00339-011-6630-7

Chavali, M. S., & Nikolova, M. P. (2019). Metal oxide nanoparticles and their applications in nanotechnology. *SN Applied Sciences*, *1*(6), 607. https://doi.org/10.1007/s42452-019-05923

Cheng, C., Xu, G., Zhang, H., Li, Y., Luo, Y., & Zhang, P. (2008). A simple route to synthesize multiform structures of tin oxide nanobelts and optical properties investigation. *Materials Science and Engineering: B*, *147*(1), 79–83. https://doi.org/10.1016/j.mseb.2007.11.018

Choi, K. J., & Jang, H. W. (2010). One-Dimensional Oxide Nanostructures as Gas-Sensing

Materials: Review and Issues. *Sensors*, *10*(4), Article 4.

Chowdhury, F. I., Blaine, T., & Gougam, A. B. (2013). Optical transmission enhancement of fluorine doped tin oxide (FTO) on glass for thin film photovoltaic applications. *Energy Procedia*, *42*, 660–669.

Cuce, E., Cuce, P. M., Wood, C. J., & Riffat, S. B. (2014). Toward aerogel based thermal superinsulation in buildings: A comprehensive review. *Renewable and Sustainable Energy Reviews*, *34*, 273–299. https://doi.org/10.1016/j.rser.2014.03.017

Dang, H. P., Luc, Q. H., Le, V. H., & Le, T. (2016). The influence of deposition temperature and annealing temperature on Ga-doped SnO2 films prepared by direct current magnetron sputtering. *Journal of Alloys and Compounds*, *687*, 1012–1020. https://doi.org/10.1016/j.jallcom.2016.06.236

Darwish, A. A., Abdelmohsen, R. S., Ahmed, M., & Megeed, M. (2022). Solar cells: Types, modules, and applications–a review. *Tanzania Journal of Science*, *48*(1), 124–133.

Devi, H. S., Boda, M. A., Shah, M. A., Parveen, S., & Wani, A. H. (2019). Green synthesis of iron oxide nanoparticles using Platanus orientalis leaf extract for antifungal activity. *Green Processing and Synthesis*, *8*(1), 38–45.

Dheyab, M. A., Aziz, A. A., Jameel, M. S., & Oladzadabbasabadi, N. (2022). Recent advances in synthesis, modification, and potential application of tin oxide nanoparticles. *Surfaces and Interfaces*, *28*, 101677. https://doi.org/10.1016/j.surfin.2021.101677

Dixon, S. C., Scanlon, D. O., Carmalt, C. J., & Parkin, I. P. (2016). n-Type doped transparent conducting binary oxides: An overview. *Journal of Materials Chemistry C*, *4*(29), 6946– 6961.

Doyan, A., Susilawati, & Imawanti, Y. D. (2017). *Synthesis and characterization of SnO2 thin layer with a doping aluminum is deposited on quartz substrates*. 020005. https://doi.org/10.1063/1.4973083

Doyan, A., Susilawati, Imawanti, Y. D., Gunawan, E. R., & Taufik, M. (2018). Characterization Thin Film Nano Particle of Aluminum Tin Oxide (AlTO) as Touch Screen. *Journal of Physics: Conference Series*, *1097*(1), 012009.

Doyan, A., Susilawati, Muliyadi, L., Hakim, S., Munandar, H., & Taufik, M. (2021). The effect of dopant material to optical properties: Energy band gap Tin Oxide thin film. *Journal of Physics: Conference Series*, *1816*(1), 012114.

Drake, C., & Seal, S. (2007). Band gap energy modifications observed in trivalent In substituted nanocrystalline SnO2. *Applied Physics Letters*, *90*(23), 233117.

Droepenu, E. K., Wee, B. S., Chin, S. F., Kok, K. Y., & Maligan, M. F. (2022). *Zinc oxide nanoparticles synthesis methods and its effect on morphology: A review*.

Duan, Y., Zheng, J., Fu, N., Jiangtao, H., Tongchao, L., Fang, Y., Zhang, Q., Zhou, X., Lin, Y., & Pan, F. (2015). Effects of Ga doping and hollow structure on the band-structures and photovoltaic properties of SnO2 photoanode dye-sensitized solar cells. *RSC Advances*, *5*, 93765–93772. https://doi.org/10.1039/C5RA19491A

Dutta, A. (2017). Fourier Transform Infrared Spectroscopy. In *Spectroscopic Methods for Nanomaterials Characterization* (pp. 73–93). Elsevier. https://doi.org/10.1016/B978-0323-46140-5.00004-2

Feinle, A., Elsaesser, M. S., & Hüsing, N. (2016). Sol–gel synthesis of monolithic materials with hierarchical porosity. *Chemical Society Reviews*, *45*(12), 3377–3399. https://doi.org/10.1039/C5CS00710K

Furka, D., Furka, S., Dueñas Santana, J. A., Tóth, A., Čaplovičová, M., Rakovský, E., Čičkan, M., & Janek, M. (2025). Enhancing Photocatalytic Efficiency Through Morphology and Band Gap Tuning in Gallium-doped Zinc Oxide Nanoparticles. *ChemNanoMat*, e202400665.

Gebreslassie, Y. T., & Gebretnsae, H. G. (2021). Green and Cost-Effective Synthesis of Tin Oxide Nanoparticles: A Review on the Synthesis Methodologies, Mechanism of Formation, and Their Potential Applications. *Nanoscale Research Letters*, *16*(1), 97. https://doi.org/10.1186/s11671-021-03555-6

Gopinath, K., Kumaraguru, S., Bhakyaraj, K., Mohan, S., Venkatesh, K. S., Esakkirajan, M., Kaleeswarran, P., Alharbi, N. S., Kadaikunnan, S., Govindarajan, M., Benelli, G., & Arumugam, A. (2016). Green synthesis of silver, gold and silver/gold bimetallic nanoparticles using the *Gloriosa superba* leaf extract and their antibacterial and antibiofilm activities. *Microbial Pathogenesis*, *101*, 1–11. https://doi.org/10.1016/j.micpath.2016.10.011

Govindasamy, S., Gunasekaran, B. M., Vaiyapuri, N., Natarajan, B., Nesakumar, N., Varatharajan, B., Britto, P. G. J., & Arjunan, A. (2024). Synthesis of tin oxide nanoparticles by chemical and biological methods and their applications in high performance supercapacitor electrode, antibacterial and antifungal activity. *Physica Scripta*, *99*(7), 075042. https://doi.org/10.1088/1402-4896/ad5770

Haq, S., Rehman, W., Waseem, M., Rehman, M., & Shah, K. H. (2020). Modeling,

Thermodynamic Study and Sorption Mechanism of Cadmium Ions onto Isopropyl Alcohol Mediated Tin Dioxide Nanoparticles. *Journal of Inorganic and Organometallic Polymers and Materials*, *30*(4), 1197–1205. https://doi.org/10.1007/s10904-019-01256-3

Hassan, N. K., Hashim, M. R., & Bououdina, M. (2013). One-dimensional ZnO nanostructure growth prepared by thermal evaporation on different substrates: Ultraviolet emission as a function of size and dimensionality. *Ceramics International*, *39*(7), 7439–7444. https://doi.org/10.1016/j.ceramint.2013.02.088

Herklotz, F., Lavrov, E. V., Melnikov, V. V., Galazka, Z., & Agekyan, V. F. (2023).

Comprehensive study of the interstitial hydrogen donor in SnO 2. *Physical Review B*, *108*(20), 205204.

Hjiri, M., Dhahri, R., El Mir, L., Bonavita, A., Donato, N., Leonardi, S. G., & Neri, G. (2015). CO sensing properties of Ga-doped ZnO prepared by sol–gel route. *Journal of Alloys and Compounds*, *634*, 187–192.

Hoag, G. E., Collins, J. B., Holcomb, J. L., Hoag, J. R., Nadagouda, M. N., & Varma, R. S. (2009). Degradation of bromothymol blue by 'greener'nano-scale zero-valent iron synthesized using tea polyphenols. *Journal of Materials Chemistry*, *19*(45), 8671–8677.

Horwat, D., Zakharov, D. I., Endrino, J. L., Soldera, F., Anders, A., Migot, S., Karoum, R., Vernoux, Ph., & Pierson, J. F. (2011). Chemistry, phase formation, and catalytic activity of thin palladium-containing oxide films synthesized by plasma-assisted physical vapor deposition. *Surface and Coatings Technology*, *205*, S171–S177. https://doi.org/10.1016/j.surfcoat.2010.12.021

Hosseini, S. M., Sarsari, I. A., Kameli, P., & Salamati, H. (2015). Effect of Ag doping on structural, optical, and photocatalytic properties of ZnO nanoparticles. *Journal of Alloys and Compounds*, *640*, 408–415. https://doi.org/10.1016/j.jallcom.2015.03.136

Hussain, I., Singh, N. B., Singh, A., Singh, H., & Singh, S. C. (2016). Green synthesis of nanoparticles and its potential application. *Biotechnology Letters*, *38*(4), 545–560. https://doi.org/10.1007/s10529-015-2026-7

Jasim, K. E., & Dakhel, A. A. (2021). Role of (Cu, Al) codoping in tuning the optical, structural and magnetic properties of Co-doped SnO2 nanostructures: A comparative study. *Physica B: Condensed Matter*, *614*, 413040. https://doi.org/10.1016/j.physb.2021.413040

Jayaseelan, C., Rahuman, A. A., Kirthi, A. V., Marimuthu, S., Santhoshkumar, T., Bagavan, A., Gaurav, K., Karthik, L., & Rao, K. V. B. (2012). Novel microbial route to synthesize ZnO nanoparticles using Aeromonas hydrophila and their activity against pathogenic bacteria and fungi. *Spectrochimica Acta. Part A, Molecular and Biomolecular Spectroscopy*, *90*, 78–84.

Jepngetich, J., Opiyo, S. A., Njoroge, P. W., & Kiprotich, S. (2025). Effects of Ag Doping

Concentrations on Structural and Optical Properties of Citrus Reticulata Capped ZnO Nanoparticles.

Jiang, H., & Stewart, D. A. (2017). Using Dopants to Tune Oxygen Vacancy Formation in Transition Metal Oxide Resistive Memory. *ACS Applied Materials & Interfaces*, *9*(19), 16296–16304.

Kafashan, H., Orshesh, Z., Bahrami, A., & Zakerian, F. (2024). Structural and optoelectronic properties of electrodeposited CdSe thin films: Effect of Cu-dopant. *Physica B: Condensed Matter*, *675*, 415623.

Kalyani, V. L., Dudy, M. K., & Pareek, S. (2015). Green energy: The need of the world. *Journal of Management Engineering and Information Technology*, *2*(5), 18–26.

Kataria, N., & Garg, V. K. (2018). Green synthesis of Fe3O4 nanoparticles loaded sawdust carbon for cadmium (II) removal from water: Regeneration and mechanism. *Chemosphere*, *208*, 818–828.

Kemuma Gichana, S., M. Mulati, D., & N. Soitah, T. (2024). Structural Characterization of Ptype SnO₂: Ga and Sb-co-doped SnO2:Ga Thin Films Prepared by Sol-Gel Dip-Coating Method for Potential Optoelectronic Applications. *Journal of Materials Physics and Chemistry*, *12*(2), 37–41.

Kethzy Agnes, J., Sharmila, D. J., Praveen, B., Pugazhendhi, K., Naveen Kumar, P., Madhavan, J., & Merline Shyla, J. (2019). A Featural Analysis of Aluminium Doped SnO2 and Bare SnO2 Thin Films Grown on FTO Substrates. *Materials Today: Proceedings*, *8*, 207–213. https://doi.org/10.1016/j.matpr.2019.02.102

Khan, S. A., Khan, S. B., Khan, L. U., Farooq, A., Akhtar, K., & Asiri, A. M. (2018). Fourier Transform Infrared Spectroscopy: Fundamentals and Application in Functional Groups and Nanomaterials Characterization. In S. K. Sharma (Ed.), *Handbook of Materials Characterization* (pp. 317–344). Springer International Publishing

Kharissova, O. V., Dias, H. V. R., Kharisov, B. I., Pérez, B. O., & Pérez, V. M. J. (2013). The greener synthesis of nanoparticles. *Trends in Biotechnology*, *31*(4), 240–248.

Khlayboonme, S. T., & Thowladda, W. (2021). Impact of Al-doping on structural, electrical, and optical properties of sol-gel dip coated ZnO: Al thin films. *Materials Research Express*, *8*(7), 076402.

Kiprotich, S., Onani, M. O., & Dejene, F. B. (2018). High luminescent L -cysteine capped CdTe quantum dots prepared at different reaction times. *Physica B: Condensed Matter*, *535*, 202– 210.

Ko, S. H., Lee, D., Kang, H. W., Nam, K. H., Yeo, J. Y., Hong, S. J., Grigoropoulos, C. P., & Sung, H. J. (2011). Nanoforest of Hydrothermally Grown Hierarchical ZnO Nanowires for a High Efficiency Dye-Sensitized Solar Cell. *Nano Letters*, *11*(2), 666–671. https://doi.org/10.1021/nl1037962

Kock, I., Edler, T., & Mayr, S. G. (2008). Growth behavior and intrinsic properties of vapordeposited iron palladium thin films. *Journal of Applied Physics*, *103*(4). https://pubs.aip.org/aip/jap/article/103/4/046108/373579

Kukli, K., Kemell, M., Mizohata, K., Vehkamäki, M., Kalam, K., Castan, H., Duenas, S., Link, J., Stern, R., Ritala, M., & Leskelä, M. (2018). Atomic Layer Deposition of Zirconium Dioxide from Zirconium Tetraiodide and Ozone. *ECS Journal of Solid State Science and Technology*, *7*(2), P1–P8. https://doi.org/10.1149/2.0041802jss

Kumar, M., Mehta, A., Mishra, A., Singh, J., Rawat, M., & Basu, S. (2018). Biosynthesis of tin oxide nanoparticles using Psidium Guajava leave extract for photocatalytic dye degradation under sunlight. *Materials Letters*, *215*, 121–124. https://doi.org/10.1016/j.matlet.2017.12.074

Layek, A., Manna, B., & Chowdhury, A. (2012). Carrier recombination dynamics through defect states of ZnO nanocrystals: From nanoparticles to nanorods. *Chemical Physics Letters*, *539*, 133–138.

Lee, S.-H., Kwon, K., Kim, K., Yoon, J. S., Choi, D.-S., Yoo, Y., Kim, C., Kang, S., & Kim, J. H. (2019). Electrical, structural, optical, and adhesive characteristics of aluminum-doped tin oxide thin films for transparent flexible thin-film transistor applications. *Materials*, *12*(1), 137.

M, N. P., Paulraj, R., P, R., & N, V. (2017). One step synthesis of tin oxide nanomaterials and their sintering effect in dye degrdation. *Optik*, *135*, 434–445. https://doi.org/10.1016/j.ijleo.2017.01.068

M., S., Girija, K. G., Kaur, M., Geetha, V., Debnath, A. K., Karri, M., Thota, M. K., Vatsa, R. K., Muthe, K. P., & Gadkari, S. C. (2018). Synergistic effect of indium and gallium codoping on the properties of RF sputtered ZnO thin films. *AIP Conference Proceedings*, *1942*, 080054.

Mahfooz-ur-Rehman, Rehman, W., Waseem, M., Shah, B. A., Shakeel, M., Haq, S., Zaman, U., Bibi, I., & Khan, H. D. (2019). Fabrication of Titanium–Tin Oxide Nanocomposite with Enhanced Adsorption and Antimicrobial Applications. *Journal of Chemical & Engineering Data*, *64*(6), 2436–2444.

Micheli, D., Pastore, R., Vricella, A., Delfini, A., Marchetti, M., & Santoni, F. (2017).

Electromagnetic Characterization of Materials by Vector Network Analyzer Experimental Setup. In *Spectroscopic Methods for Nanomaterials Characterization* (pp. 196–233). https://doi.org/10.1016/B978-0-323-46140-5.00009-1

Mittal, A. K., Chisti, Y., & Banerjee, U. C. (2013). Synthesis of metallic nanoparticles using plant extracts. *Biotechnology Advances*, *31*(2), 346–356. https://doi.org/10.1016/j.biotechadv.2013.01.003

Moharrami, F., Bagheri-Mohagheghi, M.-M., Azimi-Juybari, H., & Shokooh-Saremi, M. (2012). Structural, electrical, optical, thermoelectrical and photoconductivity properties of the SnO_2 –Al_2 O_3 binary transparent conducting films deposited by the spray pyrolysis method. *Physica Scripta*, *85*(1), 015703. https://doi.org/10.1088/0031-8949/85/01/015703

Musa, I., & Qamhieh, N. (2019). Study of optical energy gap and quantum confinment effects in Zinc Oxide nanoparticles and nanorods. *Dig. J. Nanomater. Biostruct*, *14*(1), 119–125.

Nachit, W., Ait Ahsaine, H., Ramzi, Z., Touhtouh, S., Goncharova, I., & Benkhouja, K. (2022). Photocatalytic activity of anatase-brookite TiO2 nanoparticles synthesized by sol gel method at low temperature. *Optical Materials*, *129*, 112256.

Nagirnyak, S. V., Lutz, V. A., Dontsova, T. A., & Astrelin, I. M. (2016). Synthesis and Characterization of Tin(IV) Oxide Obtained by Chemical Vapor Deposition Method. *Nanoscale Research Letters*, *11*(1), 343. https://doi.org/10.1186/s11671-016-1547-x

Nasir, H., Rahman, N., Zulfiqar, Khan, T., Ali, S., Khan, R., & Hayat, K. (2020). Variations in structural, optical, and dielectric properties of CuO nanostructures with thermal decomposition. *Journal of Materials Science: Materials in Electronics*, *31*, 10649–10656.

Ng, Z.-N., Chan, K.-Y., Sin, Y.-K., Yam, F.-K., & Knipp, D. (2017). Sol–Gel Derived Al–Ga Co-Doped ZnO Thin Films Embedded with Microrods. *Journal of Nanoscience and Nanotechnology*, *17*(1), 348–353.

Nguyen, A. H.-T., Nguyen, M.-C., Choi, J., Han, S., Kim, J., & Choi, R. (2017). Electrical performance enhancement of p-type tin oxide channel thin film transistor using aluminum doping. *Thin Solid Films*, *641*, 24–27. https://doi.org/10.1016/j.tsf.2017.01.032

Nilavazhagan, S., Muthukumaran, S., & Ashokkumar, M. (2015). Microstructural and band gap exploration on Ni-doped SnO2 nanoparticles co-doped with Cu. *Journal of Materials Science: Materials in Electronics*, *26*(6), 3989–3996. https://doi.org/10.1007/s10854-0152935-1

Pal, M., Bera, S., Sarkar, S., & Jana, S. (2014). Influence of Al doping on microstructural, optical and photocatalytic properties of sol–gel based nanostructured zinc oxide films on glass. *Rsc Advances*, *4*(23), 11552–11563.

Panneer, N. K., Venkatraman, C., Bachan, N., Wilson, J. J., Edwin, M. A., Jesudasan, A. R., & Joseph, M. S. (2023). Ecofriendly sol-gel-derived dye-sensitized solar cells

with aluminium-doped tin oxide photoanode. *Environmental Science and Pollution Research*, *30*(21), 60524–60537

Papadimitriou, D. N. (2016). Structural, optical, electrical properties, and strain/stress of electrochemically deposited highly doped ZnO layers and nanostructured ZnO antireflective coatings for cost-effective photovoltaic device technology. *Thin Solid Films*, *605*, 215–231.

Patil, G. E., Kajale, D. D., Gaikwad, V. B., & Jain, G. H. (2012). Preparation and characterization of SnO2 nanoparticles by hydrothermal route. *International Nano Letters*, *2*(1), 17. https://doi.org/10.1186/2228-5326-2-17

Patil, S. P., & Rane, P. M. (2020). Psidium guajava leaves assisted green synthesis of metallic nanoparticles: A review. *Beni-Suef University Journal of Basic and Applied Sciences*, *9*(1), 60.

Pham, D. P., Nguyen, H. T., Phan, B. T., Cao, T. M. D., Hoang, V. D., Dao, V. A., Yi, J., & Tran, C. V. (2014). In and Ga Codoped ZnO Film as a Front Electrode for Thin Film Silicon Solar Cells. *Advances in Condensed Matter Physics*, *2014*, 1–7.

Pode, R., & Diouf, B. (2011). Solar Photovoltaic Electricity. In R. Pode & B. Diouf, *Solar Lighting* (pp. 19–59). Springer London. https://doi.org/10.1007/978-1-4471-2134-3_2

Priyadharsini, C., Mathiyalagan, S., Annamalai, P., Anbarasan, P., Renganathan, S., & Aroulmoji, V. (2017). Effect of Mg Doping on Structural and Optical Properties of SnO2 Nanoparticles by Chemical Co-Precipitation Method. *International Journal of Advanced Science and Engineering*, *3*, 428–434.

Qin, X.-J., Yu, Q., Yan, H., Khan, A., Feng, M.-Y., Li, P.-P., Hao, X.-J., An, L.-K., & Liu, H.-Y. (2017). Meroterpenoids with Antitumor Activities from Guava (Psidium guajava). *Journal of Agricultural and Food Chemistry*, *65*(24), 4993–4999. https://doi.org/10.1021/acs.jafc.7b01762

Rabinovich, D. (2013). The allure of aluminium. *Nature Chemistry*, *5*(1), 76–76. https://doi.org/10.1038/nchem.1535

Rahman, I. A., & Padavettan, V. (2012). Synthesis of Silica Nanoparticles by Sol-Gel: Size Dependent Properties, Surface Modification, and Applications in Silica-Polymer Nanocomposites—A Review. *Journal of Nanomaterials*, *2012*, 1–15. https://doi.org/10.1155/2012/132424

Rajan, R., & Vizhi, R. E. (2017). Investigation of Room-Temperature Ferromagnetism on Pristine and Non-ferromagnetic Dopant-Substituted SnO2 Nanoparticles. *Journal of Superconductivity and Novel Magnetism*, *30*(11), 3199–3206.

Ramesh, S. (2013). *Sol-gel synthesis and characterization of Ag*.

Ran, L., Zhao, D., Gao, X., & Yin, L. (2015). Highly crystalline Ti-doped SnO_2 hollow structured photocatalyst with enhanced photocatalytic activity for degradation of organic dyes. *CrystEngComm*, *17*(22), 4225–4237. https://doi.org/10.1039/C5CE00184F

Rauwel, P., Galeckas, A., & Rauwel, E. (2021). Enhancing the UV emission in ZnO–cnt hybrid nanostructures via the surface plasmon resonance of Ag nanoparticles. *Nanomaterials*, *11*(2), 452.

Rivera, M. J., Ramírez, E. B., Juárez, B., González, J., García-León, J. M., Escobar-Alarcón, L., & Alonso, J. C. (2016). Low temperature-pyrosol-deposition of aluminum-doped zinc oxide thin films for transparent conducting contacts. *Thin Solid Films*, *605*, 108–115.

Sabri, N. S., Deni, M. S. M., Zakaria, A., & Talari, M. K. (2012). Effect of Mn Doping on Structural and Optical Properties of SnO2 Nanoparticles Prepared by Mechanochemical Processing. *Physics Procedia*, *25*, 233–239. https://doi.org/10.1016/j.phpro.2012.03.077

Sagadevan, S. (2015). Preparation, Structural and Electrical Properties of Tin Oxide Nanoparticles. *Journal of Nanomaterials & Molecular Nanotechnology*, *4*(1). https://doi.org/10.4172/2324-8777.1000157

Sagadevan, S., Pal, K., Chowdhury, Z. Z., & Hoque, M. E. (2017). Structural, dielectric and optical investigation of chemically synthesized Ag-doped ZnO nanoparticles composites. *Journal of Sol-Gel Science and Technology*, *83*(2), 394–404.

Saha, M., Ghosh, S., Ashok, V. D., & De, S. K. (2015). Carrier concentration dependent optical and electrical properties of Ga doped ZnO hexagonal nanocrystals. *Physical Chemistry Chemical Physics*, *17*(24), 16067–16079. https://doi.org/10.1039/C4CP05480F

Saha, P., Mahiuddin, Md., Islam, A. B. M. N., & Ochiai, B. (2021). Biogenic Synthesis and Catalytic Efficacy of Silver Nanoparticles Based on Peel Extracts of *Citrus macroptera* Fruit. *ACS Omega*, *6*(28), 18260–18268.

Samavati, A., Samavati, Z., Ismail, A. F., Othman, M. H. D., Rahman, M. A., Zulhairun, A. K., & Amiri, I. S. (2017). Structural, optical and electrical evolution of Al and Ga co-doped ZnO/SiO_2 /glass thin film: Role of laser power density. *RSC Advances*, *7*(57), 35858– 35868.

Sapkota, R., Duan, P., Kumar, T., Venkataraman, A., & Papadopoulos, C. (2021). Thin Film Gas Sensors Based on Planetary Ball-Milled Zinc Oxide Nanoinks: Effect of Milling Parameters on Sensing Performance. *Applied Sciences*, *11*(20), Article 20. https://doi.org/10.3390/app11209676

Sarangi, S. N., Pradhan, G. K., & Samal, D. (2018). Band gap engineering in SnO2 by Pb doping. *Journal of Alloys and Compounds*, *762*, 16–20. https://doi.org/10.1016/j.jallcom.2018.05.143

Seid, E. T., & Dejene, F. B. (2021). Gallium and indium co-doping effects on structural, optical and luminescence properties of ZnO nanostructures. *Materials Today Communications*, *27*, 102330.

Selvakumari, J. C., Ahila, M., Malligavathy, M., & Padiyan, D. P. (2017). Structural, morphological, and optical properties of tin(IV) oxide nanoparticles synthesized using Camellia sinensis extract: A green approach. *International Journal of Minerals, Metallurgy, and Materials*, *24*(9), 1043–1051.

Shankar, S., & Rhim, J.-W. (2015). Amino acid mediated synthesis of silver nanoparticles and preparation of antimicrobial agar/silver nanoparticles composite films. *Carbohydrate Polymers*, *130*, 353–363.

Shanmuga Priya, B., Shanthi, M., Manoharan, C., & Dhanapandian, S. (2017). Synthesis, characterization and photocatalytic activity of pure and Zn-doped In2O3 nanostructures. *Journal of Materials Science: Materials in Electronics*, *28*(17), 12784–12794.

Shinde, S. S., Shinde, P. S., Oh, Y. W., Haranath, D., Bhosale, C. H., & Rajpure, K. Y. (2012). Structural, optoelectronic, luminescence and thermal properties of Ga-doped zinc oxide thin films. *Applied Surface Science*, *258*(24), 9969–9976. https://doi.org/10.1016/j.apsusc.2012.06.058

Siddiqui, H., Parra, M. R., & Haque, F. Z. (2018). Optimization of process parameters and its effect on structure and morphology of CuO nanoparticle synthesized via the sol- gel technique. *Journal of Sol-Gel Science and Technology*, *87*, 125–135.

Singh, G., Kohli, N., & Singh, R. C. (2017). Sensitive and selective ethanol sensor based on Zndoped SnO2 nanostructures. *Journal of Materials Science: Materials in Electronics*, *28*(17), 13013–13023. https://doi.org/10.1007/s10854-017-7133-x

Singh, G., & Singh, R. C. (2019). Synthesis, Characterization and Gas Sensing Properties of Ga-Doped SnO2 Nanostructures. *Journal of Electronic Materials*, *48*(7), 4478–4490. https://doi.org/10.1007/s11664-019-07231-5

Siyalo, S., Etefa, H. F., & Dejene, F. B. (2025). Enhancing structural and optical properties of CuO thin films through gallium doping: A pathway to enhanced photoluminescence and predict for solar cells applications. *Chemical Physics*

Impact, *10*, 100832. https://doi.org/10.1016/j.chphi.2025.100832 Smith, B. C. (2011). *Fundamentals of Fourier Transform Infrared Spectroscopy*. CRC Press

Subramaniam, M. P., Arunachalam, G., Kandasamy, R., Veluswamy, P., & Hiroya, I. (2018). Effect of pH and annealing temperature on the properties of tin oxide nanoparticles prepared by sol–gel method. *Journal of Materials Science: Materials in Electronics*, *29*(1), 658–666. https://doi.org/10.1007/s10854-017-7959-2

Suthakaran, S., Dhanapandian, S., Krishnakumar, N., & Ponpandian, N. (2019). Hydrothermal synthesis of SnO2 nanoparticles and its photocatalytic degradation of methyl violet and electrochemical performance. *Materials Research Express*, *6*(8), 0850i3. https://doi.org/10.1088/2053-1591/ab29c2

Suthakaran, S., Dhanapandian, S., Krishnakumar, N., & Ponpandian, N. (2020). Hydrothermal synthesis of surfactant assisted Zn doped SnO2 nanoparticles with enhanced photocatalytic performance and energy storage performance. *Journal of Physics and Chemistry of Solids*, *141*, 109407

Tazikeh, S., Akbari, A., Talebi, A., & Talebi, E. (2014). Synthesis and characterization of tin oxide nanoparticles via the Co-precipitation method. *Materials Science-Poland*, *32*(1), 98– 101. https://doi.org/10.2478/s13536-013-0164-y

Teh, J. J., Ting, S. L., Leong, K. C., Li, J., & Chen, P. (2013). Gallium-Doped Tin Oxide NanoCuboids for Improved Dye Sensitized Solar Cell. *ACS Applied Materials & Interfaces*, *5*(21), 11377–11382.

Thamarai Selvi, E., & Meenakshi Sundar, S. (2018). Popcorn like morphology and absence of room temperature ferromagnetism in Ni doped SnO2 nanoparticles. *Journal of Materials Science: Materials in Electronics*, *29*(1), 38–48. https://doi.org/10.1007/s10854-017-78853

Thanh, N. T. K., Maclean, N., & Mahiddine, S. (2014). Mechanisms of Nucleation and Growth of Nanoparticles in Solution. *Chemical Reviews*, *114*(15), 7610–7630. https://doi.org/10.1021/cr400544s

Thankaian, R. D., Muthukrishnan, M., Thiagamani, S. M. K., Siengchin, S., & Rangappa, S. M. (2022). Impact of metal doping and co-doping on the electrical and optical behavior of tin oxide nanoparticles. *Nanomaterials and Energy*, *11*(3–4), 55–66. https://doi.org/10.1680/jnaen.23.00010

Tiwari, A., & Sahay, P. P. (2020). Sn–Ga co-doping in sol-gel derived ZnO thin films: Studies of their microstructural, optical, luminescence and electrical properties. *Materials Science in Semiconductor Processing*, *118*, 105178. https://doi.org/10.1016/j.mssp.2020.105178

Tsay, C.-Y., & Liang, S.-C. (2015). Fabrication of p-type conductivity in SnO2 thin films through Ga doping. *Journal of Alloys and Compounds*, *622*, 644–650. https://doi.org/10.1016/j.jallcom.2014.10.003

U, M. raj, J, P., R, V., S, A. P., & M, N. S. (2024). Advancements In Calcium Carbonate Nanoparticles: Novel Strategies For Osteomyelitis Treatment. *International Journal of Pharmaceutical Sciences*, *02*(02), Article 02. https://doi.org/10.5281/zenodo.10781159

Vidhya, S. N., Balasundaram, O. N., & Chandramohan, M. (2016). Structural and optical investigations of gallium doped tin oxide thin films prepared by spray pyrolysis. *Journal of Saudi Chemical Society*, *20*(6), 703–710. https://doi.org/10.1016/j.jscs.2015.01.006

Wang, C., Yin, L., Zhang, L., Xiang, D., & Gao, R. (2010). Metal oxide gas sensors: Sensitivity and influencing factors. *Sensors*, *10*(3), 2088–2106.

Wang, S.-C., & Shaikh, M. O. (2015). A Room Temperature H2 Sensor Fabricated Using High Performance Pt-Loaded SnO2 Nanoparticles. *Sensors*, *15*(6), Article 6. https://doi.org/10.3390/s150614286

Waweru, G. S., Kiprotich, S., & Waithaka, P. (2024a). Effects of Growth Temperature on the Structural and Optical Properties of Synthesized Titanium Dioxide Nanoparticles. *American Journal of Materials Science*.

Waweru, G. S., Kiprotich, S., & Waithaka, P. (2024b). *Effects of growth temperature on the structural and optical properties of synthesized titanium dioxide nanoparticles*. https://idlbnc-idrc.dspacedirect.org/bitstreams/1e065307-334f-44fa-9559-d21854b73e9d/download

Ye, M., Wen, X., Wang, M., Iocozzia, J., Zhang, N., Lin, C., & Lin, Z. (2015). Recent advances in dye-sensitized solar cells: From photoanodes, sensitizers and electrolytes to counter electrodes. *Materials Today*, *18*(3), 155–162. https://doi.org/10.1016/j.mattod.2014.09.001

Yuan, Y., & Huang, J. (2016). Ion Migration in Organometal Trihalide Perovskite and Its Impact on Photovoltaic Efficiency and Stability. *Accounts of Chemical Research*, *49*(2), 286–293. https://doi.org/10.1021/acs.accounts.5b00420

Yue, S., Yan, Z., Shi, Y., & Ran, G. (2013). Synthesis of zinc oxide nanotubes within ultrathin anodic aluminum oxide membrane by sol–gel method. *Materials Letters*, *98*, 246–249. https://doi.org/10.1016/j.matlet.2013.02.037

Zayed, M., Ghazal, H., Othman, H., & Hassabo, A. G. (2022). Psidium guajava leave extract for improving ultraviolet protection and antibacterial properties of cellulosic fabrics. *Biointerf. Res. Appl. Chem*, *12*(3), 3811–3835.

Zebbar, N., Chabane, L., Gabouze, N., Kechouane, M., Trari, M., Aida, M. S., Belhousse, S., & Larbi, F. H. (2016). *Thin Solid Films*, *605*, 89–94.

Zhang, T., Lu, G., Shen, H., Shi, K., Jiang, Y., Xu, D., & Gong, Q. (2014). Photoluminescence of a single complex plasmonic nanoparticle. *Scientific Reports*, *4*(1), 3867. https://doi.org/10.1038/srep03867

Zhao, L., Ryu, S.-W., Hazeghi, A., Duncan, D., Magyari-Kope, B., & Nishi, Y. (2013, January 1). *Dopant Selection Rules for Extrinsic Tunability of HfOx RRAM Characteristics: A Systematic Study*.

Zhou, Y., Shim, J. W., Fuentes-Hernandez, C., Sharma, A., Knauer, K. A., Giordano, A. J., Marder, S. R., & Kippelen, B. (2012). Direct correlation between work function of indiumtin-oxide electrodes and solar cell performance influenced by ultraviolet irradiation and air exposure. *Physical Chemistry Chemical Physics*, *14*(34), 12014–12021. https://doi.org/10.1039/C2CP42448G

APPENDICES

Appendix 1: Research authorization

MURANG'A UNIVERSITY OF TECHNOLOGY

Office of the Director, Postgraduate Studies

E-mail: ips@mut.ac.ke
Website: www.mut.ac.ke
P.O. Box 75-10200
Murang'a, Kenya

Ref: MUT/ARP/PGS/19/2020 /VOL.1 **Date:** 27th March, 2025

Mr. Bethwel Kiprotich- AS401/5137/2023
School of Pure, Applied and Health Sciences,
Murang'a University of Technology,
P.O. Box 75-10200
Murang'a.

Dear Mr. Kiprotich,

RE: APPROVAL OF RESEARCH PROPOSAL AND SUPERVISORS.

I am pleased to inform you that the Directorate of Postgraduate Studies on 11th March, 2025 considered and approved your Master research proposal entitled ***"Synthesis and Characterization of AL-Ga CO-doped Tin Oxide Nanoparticles using Psidium Quajava Leaves Extract for Potential Application in Solar Cell ."*** and appointed the following as supervisors:

1. Dr. Peter Waithaka- Murang'a University of Technology
2. Prof. Sylvia Opiyo- Murang'a University of Technology

You may now proceed with your data collection subject to obtaining research permit from NACOSTI, if required. You should also begin consulting your supervisors and submit through them quarterly progress reports to the Director Postgraduate Studies through your CoD and School Dean. Progress Reports forms can be accessed in the Student Portal.

It is the policy and regulations of the University that you observe deadlines. The guidelines on Postgraduate supervision can be accessed in the post graduate Handbook.

Your responsibilities as a student will include, among others;

i. Maintain regular consultation with your supervisor(s), at least once a month
ii. Submit quarterly reports on time, through your supervisors, CoD, Dean and to the Director of Postgraduate Studies;

iii. Ensure quality work all through;
iv. Present your research findings at 2-3 seminars/conferences prior to thesis examination.
v. Publish one (1) article from your research findings in a refereed journal prior to thesis examination.

For any further clarification please contact the undersigned.

Yours Sincerely,

Prof. Geoffrey Muchiri, PhD
Director, Postgraduate Studies
GM/MMK

DIRECTORATE OF POSTGRADUATE STUDIES
MURANG'A UNIVERSITY OF TECHNOLOGY
27 MAR 2025
P. O. Box 75 - 10200, MURANG'A
Tel: 0771463515, Email: info@[illegible]

Copy to:
1. Registrar – Academics and Students Affairs
2. Dean - School of Pure, Applied and Health Sciences

Appendix 2: Publications

This thesis has produced the following publication:

Bethwel, K., Waithaka, P., Opiyo, S. A., & Kiprotich, S. (2025). Effects of *Psidium guajava* extract on optical and structural properties of tin oxide nanoparticles. *American Journal of Materials Science, 15*(1), 1–8.